Investigation of plasma polymerization
in rf discharge
by novel fibre based FTIR diagnostic tool

Inauguraldissertation

zur

Erlangung des akademischen Grades

doktor rerum naturalium (Dr. rer. nat.)

an der Mathematisch-Naturwissenschaftlichen Fakultät

der

Ernst-Moritz-Arndt-Universität Greifswald

vorgelegt von

Konstantin Li

geboren am 10.06.1972

in Magnitogorsk, Russland

Greifswald, 2002

Dekan: .... Prof. Dr. rer. nat. K.Fesser ....

1. Gutachter: .... Prof. Dr. rer. nat. J.Meichsner ......

2. Gutachter: .... Prof. Dr. rer. nat. G.Marx ....

Tag der Promotion: .... 14. Juni 2002 ....

ACAT	autocollimating and alignment telescope
ATR	attenuated total reflection
BS	beamsplitter
CA	cellulose acetate
CAS-Number	Chemical Abstracts Service Number
DECR	distributed electron cyclotron resonance
EEDF	electron energy distribution function
ESMA	electron beam microanalysis (Elektronenstrahl Mikroanalyse)
EWS	evanescent wave spectroscopy
FT	Fourier Transform
FTIR	Fourier Transform Infrared
FWHH	full width at half-height
GC	gas chromotography
HMDSO	hexamethyldisiloxane
HMFG	heavy metal fluoride glasses
HWHM	half width at half maximum
IR	infrared
IRE	internal reflection element
IRRAS	infrared reflection absorption spectroscopy
IRS	internal reflection spectroscopy
MCT	mercury cadmium telluride
MS	mass spectrometry
MW	molecular weight
NA	numerical aperture
OES	optical emission spectroscopy
P	pyrolysis
PC	polycrystalline
PDMS	polydimethylsiloxane
PECVD	plasma enhanced chemical vapour deposition
PP	plasma polymer
PPS	plasma polymerized styrene
PTMSP	poly (1-trimethylsilyl-1-propyne)
PVTMS	poly (vinyltrimethylsilane)
rf	radio frequency
SC	single crystal
SEM	secondary electron microscopy
S/N	signal-to-noise ratio
TDLAS	tuneable diode laser absorption spectroscopy
UV	ultraviolet
XPS	X-ray photoelectron spectroscopy

List of symbols
(in order of appearance)

p	pressure
Vp	plasma potential
V_{bias}	self bias voltage
V_{rf}	amplitude of rf voltage
V_g	amplitude of voltage of grounded electrode
A_{rf}	area of powered electrode
A_g	area of grounded electrode
V_m	amplitude of rf modulation voltage
V_{pp}	peak-to-peak voltage
τ_{res}	residence time
V	chamber volume
f	gas flow rate
I_0	laser intensity without absorption
I_{tran}	intensity of transmitted laser beam
$\Delta\nu_d$	Doppler half width at half maximum
S	line strength
L	optical path length
A_x	absorption peak height of species X
A_{ref}	peak height of reference absorption line
$\Delta\nu_d$	experimental line width
δ	mirror retardation
$\overline{\nu}$	wavenumber
Δ	maximum retardation
A	absorbance
a	molar extinction coefficient
d	thickness
$E_{x,y}$	electric field components in x–, y-directions
$E_{0x,y}$	amplitudes of electric field components
ω	frequency
δ	phase angle
Ψ	ellipsometric angle
Δ	ellipsometric angle
n	refractive index
k	extinction coefficient
R	Fresnel reflection coefficient
λ	wavelength
E_g	optical band gap
Perm	permeability coefficient
V	cell volume
Δp	pressure difference
T	temperature

t	time
$J_{Knudsen}$	Knudsen flow
n	number of pores
τ_{pore}	pore tortuosity
r	pore radius
D_k	Knudsen diffusion coefficient
M_w	molecular weight
J	flux
α	ideal selectivity
θ_c	critical angle
n_{pp}	refractive index of plasma polymer
n_c	refractive index of fibre core
ρ	fibre radius
n_{air}	refractive index of air
θ	angle of ray incidence within fibre core
V	fibre parameter
n_{cl}	refractive index of cladding
N	number of reflections
τ_{ray}	ray transit time
E_t	tangential component of electric field
D_n	normal component of electric displacement
ε_c	dielectric constant of fibre core
ε_{pp}	dielectric constant of plasma polymer
$\overline{S}_x$	Pointing's vector
$\mathbf{H}$	net magnetic field in solids
d_p	penetration depth
d_s	sampling depth
d_e	effective thickness
α_{pp}	absorption coefficient of plasma polymer
γ_f	absorption per unit length of fibre
T_g	glass transition temperature
$\tau_{accumulation}$	accumulation time
V_m	molar volume
s	thickness of plasma polymer monolayer
N_a	Avogadro number
N_{ring}	number of phenyl rings inside cluster
E_{g0}	band gap energy associated with one ring cluster
m/z	mass-to-charge ratio
$I_{ss}(i)$	count rate of fragment ion i in the steady state in discharge
$I_0(i)$	count rate of fragment ion i without discharge
ϕ	composite process parameter

W	discharge power
k	Boltzmann constant
M	monomer molecule mass
ϕ_c	critical value of composite process parameter
Θ	Langmuir isotherm
K_{ads}	adsorption coefficient
a	characteristic size of active particle
n_s	surface concentration of growing plasma polymer
Z	collision frequency
p_a	partial pressure of neutral active species
n_i	ion density
u_b	Bohm velocity
ν_i	ionization frequency
β_{dis}	coefficient of dissociative recombination
n_e	electron density
τ_{dif}	ion diffusion time
R	chamber radius
l	chamber height
D_{amb}	coefficient of ambipolar diffusion
μ_i	ion mobility
T_e	electron temperature
T_i	ion temperature
ν_m	elastic collision frequency
ν_u	frequency of energy loss for electrons
$\boldsymbol{v}_{de}$	electron drift velocity
E_{eff}	effective electric field
τ_0	ion flight time through plasma sheath
$\langle \varepsilon \rangle$	average electron energy
σ_{tr}	transport cross-section
m	electron mass

Content

Appendix A

Appendix B

Appendix C

Appendix D

Appendix E

Explanation (Erklärung)

Curriculum Vitae (Lebenslauf)

Acknowledgements

Introduction

Non-isothermal plasma processing is already recognized technology of thin organic film fabrication. Have the discharge to be ignited in the vapour of organic compound, high molecular weight products would be formed in the gas phase or on the surface. The process, in which this transformation occurs, is designated as plasma polymerization [1, 2].

The aimed thin organic film deposition in reactive plasmas is possible only in the limited number of cases because of the high complexity of process. The main problems consist in the following issues:

— the process takes place in non-equilibrium plasma with a large number of elementary reactions including plasma-surface interaction;

— stable products of plasma-chemical conversion can partially replace the monomer due to recirculation;

— the lack of data on the properties of low temperature plasma of complex monomer compounds and on the reactions makes the comprehensive description of such plasma hardly possible.

Analysing the methodology of investigations of plasma polymerization, one distincts two main approaches: microkinetic and macroscopic, [3]. The former assumes analytic description of transport phenomena in reactor, an electric discharge, elementary reactions in the gas phase as well as on the surface. Microkinetic analysis allows one to clear up the process kinetics, if the elementary data on monomer molecules, products of plasma-chemical conversion (gaseous species and solids) and on all possible reactions are known. This approach can not be applied to complex monomer compounds utilized in the applications of industrial scale, at least now. In the macroscopic description one considers the transformation of monomer in the stable products, gaseous and solid, as a result of the various processes in a discharge plasma (ionization, dissociation, etc) taking into account only brutto-reactions. This method assumes the experimental investigations of the correlations between process parameters and products of plasma-chemical conversion. As a result of the study of defined system (monomer substance, discharge type, etc) by means of any approach one should be able to influence the necessary reaction route by the process parameters and, thus, to control both the deposition kinetics and the film quality. Other important issue is a process scaling. The results, obtained from the study of a specific case, should be applicable for other process systems independent on discharge type, reactor scale, etc.

To realize the aimed manufacturing of thin organic films in discharge plasma, it is necessary not only to set correct process parameters gained by study of the process of interest, but also to carry out a control of the film quality during the deposition. The latter should provide real time data about whether chemical composition and structure or physical properties of obtained film.

The aim of this work consists in the following issues:

1) development of a diagnostic tool for *in situ* analysis of the formation of molecular structure of thin organic films deposited in plasma. It should preferably be applicable not only for the diagnostics of plasma polymerization process, but also for the study of plasma treatment of conventional polymer films.

2) investigation of thin film deposition in low pressure rf discharge containing hexamethyldisiloxane (HMDSO)

> The next problems of interest were marked out as a result of the undertaken study
> of the published works devoted to the film deposition in the HMDSO plasmas:
> - the influence of the process parameters on the formation of molecular structure;
> - formation of molecular structure of films deposited at the various steps of plasma chemical conversion of the monomer.
> - formation of molecular structure of the films deposited at the intensive and moderate ion bombardment which can permit to draw conclusions about the role of ions in the film growth and the deposition kinetics;

The analytical methods for the characterization of thin organic films deposited in plasma should meet the appropriate requirements. In dependence upon the characterization level (electronic structure, molecular structure, chemical composition, etc) one has to choose the appropriate technique of the surface analysis or the combination of them. The deposites have to be studied *in situ* in order to avoid the surface oxidation due to the influence of the ambient air. Moreover, *in situ* diagnostic techniques of the appropriate time resolution allow one to follow the deposition process, i.e. to study the film formation. High sensitivity of technique would provide the detailed information not only on the obtained film, but also on the deposition mechanism. These and other requirements stimulate further modification of the existing characterization techniques and development of the new ones.

IR spectroscopy is one of the effective tools for investigation of molecular structure and composition of plasma polymerized films. There have been developed a variety of special techniques of IR or FTIR spectroscopy like internal reflection spectroscopy (IRS), attenuated total reflection (ATR) spectroscopy, etc. The most of them can be used for *in situ* study of plasma deposited or plasma treated films [4 − 9]. There are some main disadvantages of the techniques which are used for *in situ* diagnostics:

— utilized now ATR, IRRAS arrangements allow one to analyse films on the powered or grounded electrode only;

— direct IR absorption spectroscopy of gas phase provides the information only about macroparticles;

— typical internal reflection elements (IRE) are relatively large in size (the order of centimeters) and strongly perturb the plasma.

The diagnostic tool of question should be free of such limitations and provide further advantages. Evanescent wave spectroscopy (EWS) was taken as a base for a novel FTIR diagnostic tool. EWS assumes the use of tiny optical fibre as a medium for radiation transmission and as an active probe which should be placed in the process vessel. IR radiation from a source passed through an IR fibre is partially absorbed due to interaction with the molecules of plasma polymer film growing on the surface of the active part of the fibre. The absorption is measured by detector of FTIR spectrometer. Obtained IR absorption spectra permit to identify molecular groups composing the growing plasma polymer. Thus, it is possible to control molecular structure of the growing film without any extraction of sample from the process vessel.

The analysis of the theory of evanescent wave spectroscopy and the theory of optical waveguides intends to determine the following issues:

— fibre and measurement parameters which determine the sensitivity of the technique;

— potential advantages and drawbacks as well as method limitations.

The technique is tested on the well known styrene plasma polymerization process. The aim of the trial is to clear up the applicability of the tool to the diagnostics of plasma deposition and to analyse the issues mentioned above.

The second part of this work is devoted to the investigation of the film deposition in the HMDSO-containing plasmas. Hexamethyldisiloxane (HMDSO) is one of the most utilized organosilicon compounds used for a thin film deposition in discharge plasma. Plasma processing of the HMDSO has already found many important applications in industry for manufacturing of optics [10, 11], barrier films for food packaging or gas separating membranes [12 − 14], dielectric coatings [15, 16], and corrosion protection layers [17, 18]. The comprehensive review of plasma processing of organosilicon monomers was presented by Wrobel and Wertheimer [19]. Despite of numerous publications devoted to the deposition of organosilicons the main aspects of the process have not been clarified: the plasma chemistry, the plasma-substrate interaction, the film formation.

The information required for the study of plasma polymerization can be gained only by means of the combination of various diagnostic techniques which covers analysis of electrical discharge, diagnostics of gase phase and characterization of thin film. The complex study of the HMDSO plasma deposition was undertaken in this work. The gas phase composition (neutral species) as well as the plasma-chemical conversion were analysed by mass spectrometry and IR tuneable diode laser absorption spectroscopy. The film growth was followed by *in situ* ellipsometry (film thickness, deposition rate) and by novel FTIR fibre based diagnostic tool (molecular structure). Various techniques of the film characterization including the developed one were applied to study the state of surface, structure, composition and properties of the films deposited in the HMDSO plasmas. The overview of the applied experimental methods is given in the appropriate chapter.

Low pressure capacitively coupled rf discharge

The physical effects appeared in capacitively coupled rf discharges of low presures make them very attractive for many technological applications. Rf discharges are sustained by radio frequency, $1-100$ MHz, currents and voltages. Capacitive type of excitation is applied usually for discharge ignition at the low, $p \sim 1-100$ Pa, pressures. The discharge power is defined by a process of interest and can be varied in the wide region, $1-10^3$ W.

Figure 1 shows a coupling geometry chosen in this work for producing of capacitive rf discharge. Idealized time dependent potential structure is presented also. The most rf discharges are asymmetrical at low pressures, even in case of the parallel plate configuration of the electrodes, because the rf current is confined not only by electrodes, but also by the wall of a vacuum chamber. The dc voltage between the plasma and the powered electrode is larger than that between the plasma and the grounded electrode. A negative self bias voltage, V_{bias}, which is a little less than half the peak to peak rf voltage, is created on the powered electrode, see Figure 2.

The self bias depends on the ratio of the surfaces of electrodes and the amplitude of the applied rf voltage. It can be shown that the powered-to-grounded voltage ratio, $\overline{V}_{rf} / \overline{V}_g$, is inversely proportional to the electrode area, A_g/A_{rf} [21 p.$133-138$, 22 p. $368-372$]:

$$\frac{\overline{V}_{rf}}{\overline{V}_g} \approx \left(\frac{A_g}{A_{rf}}\right)^q \tag{1}$$

with $q \leq 2.5$.

The plasma of the low pressure capacitive rf discharge is non-equilibrium, weakly ionized. The bulk plasma has the following typical values of the parameters: electron temperature, T_e, $1-3$ eV, temperature of heavy particles $T \sim 300$ K, plasma density $10^8 - 10^{11}$ cm^{-3}. Low pressure capacitively coupled rf discharges are characterized by plasma sheathes formed at the electrodes in such a way that conduction current in bulk plasma is closed by displacement current on the electrodes.
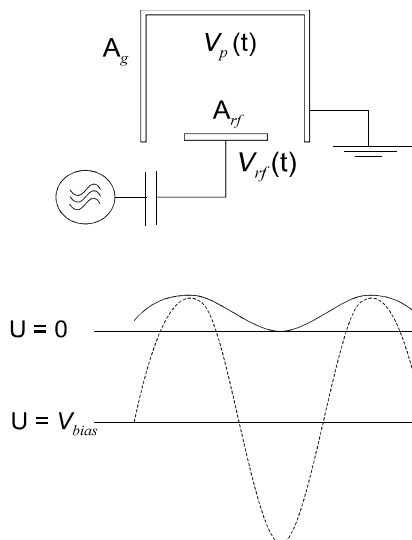
Figure 1. The scheme of the chosen reactor geometry for asymmetrical capacitively coupled rf discharge. Driving voltage V_{rf} (dashed line) and plasma potential V_p (solid line).

Figures 2 (a, b) shows the axial distribution of the plasma density (positive single charged molecular ions) in the rf (13.56 MHz) discharge in oxygen. The ion density reaches a maximum value at the distance of about 2 *cm* from the driven electrode and then decreases rapidly. The estimated plasma sheath thickness is about of 6 *mm* at the chosen discharge parameters. The pressure increase reduces the plasma density at the fixed rf voltage, see Figure 2(b).

The plasma potential, V_p, is positive with respect to all potentials of the electrodes in contact with the plasma. Hence, the time-averaged electric field in plasma sheathes is directed to the electrodes. At low pressures ions can cross the plasma sheath without collisions and accelerate within the sheath up to energies of about of the plasma sheath potential which can be of about hundreds eV. The processes in the plasma sheathes influence on energy spectra and fluxes of charged and neutral particles. The bombardment of solids by energetic ions has a strong influence on the deposition process. The dc voltage across the sheath, which determines the ion energy, depends, first of all, on the amplitude of the applied rf voltage. Other factor, which has an influence on the ion energy, is asymmetry of capacitively coupled rf discharge.

The Figures 3(a, b) show the O_2^+ ion energy distribution functions (IEDF) on rf and grounded electrodes in asymmetrical capacitively coupled rf (13.56 MHz) discharge respectively. The multiple peak structure of the ion energy distribution function at the rf electrode is due to the modulation of sheath voltage and charge transfer collisions in the plasma sheath. Slow ions and energetic neutral species appear as a result of the charge transfer collisions. The rf modulation is the main factor in case of collisionless plasma sheath at the rf electrode, while it is negligible low ($V_m \ll \overline{V}_p$) for
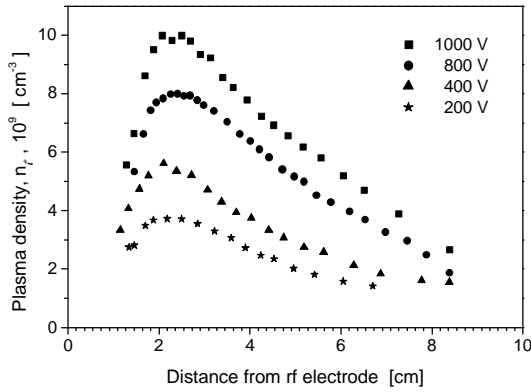
Figure 2(a).
Axial distribution of the plasma density
with the distance from the driven electrode
in the O$_2$ rf discharge (adapted from [20])
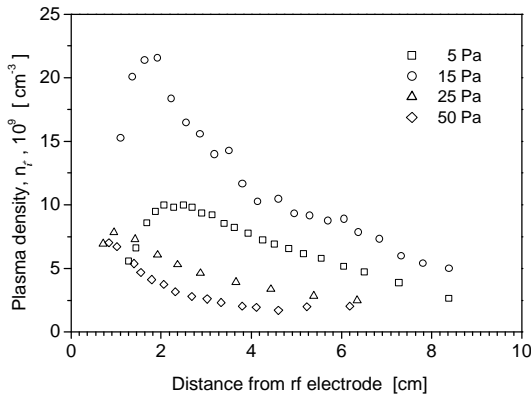Variation parameter: peak-to-peak voltage.
Total pressure: 5 Pa.

Figure 2(b).
Axial distribution of the plasma density
with the distance from the driven electrode
in the O$_2$ rf discharge.
Variation parameter: total pressure.
Applied peak-to-peak voltage: 1000 V.

the sheath at the grounded electrode. The variation of amplitude of the rf voltage influences the self bias voltage. Doubling of the peak-to-peak rf voltage, 720 V vs 360 V, causes higher self bias, -322 V vs -165 V respectively. This enhancement of self bias contributes to the appearance of high energetic ion part in the distribution function, see Figure 3(a). The increase of the total pressure results in the shift of the ion energy distribution in the low energy region due to elastic ion-molecule collisions.

The ion energy distribution functions on the grounded electrode is determined by the plasma potential which is low and close to the floating potential, which is typically of about $10 - 20$ eV. That is why, the IEDFs are shifted in the low energy region, see Figure 3(b). Thus, the substrates immersed in the bulk plasma or placed on the grounded electrode are exposed to low energetic ion flux.
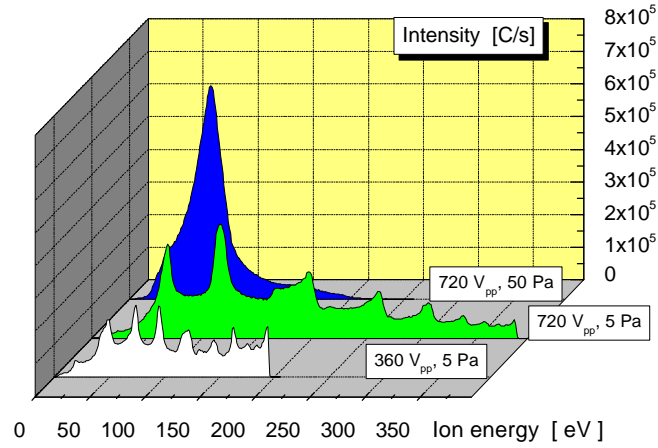
Figure 3(a). Ion energy distribution functions of molecular oxygen ions, O_2^+, on the rf electrode. Process and plasma parameters:
V_{pp} 360 V, discharge power 27 W, total pressure 5 Pa, V_{bias} −165 V;
V_{pp} 720 V, discharge power 74 W, total pressure 5 Pa, V_{bias} −322 V;
V_{pp} 720 V, discharge power 92 W, total pressure 50 Pa, V_{bias} −223 V.
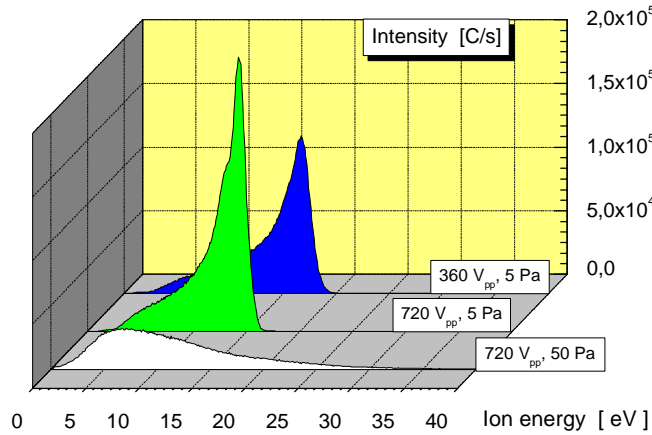

Figure 3(b). Ion energy distribution functions of molecular oxygen ions, O_2^+, on the grounded electrode. Process and plasma parameters:
V_{pp} 360 V, discharge power 31 W, total pressure 5 Pa, V_{bias} −157 V;
V_{pp} 720 V, discharge power 92 W, total pressure 5 Pa, V_{bias} −330 V;
V_{pp} 720 V, discharge power 99 W, total pressure 50 Pa, V_{bias} −204 V.

Experimental apparatus and methods

This chapter gives a short description of the experimental details of the investigation. The description of the arrangement is followed by the overview of the main techniques applied in this work for a diagnostics of gas phase and thin organic film characterization.

3.1 Experimental arrangement

Thin film deposition was carried out in the plasma of low pressure asymmetrical rf discharge at the frequency of 13.56 MHz. The typical values of the process parameters are:

total pressure: $1 - 100$ Pa; gas flow rate: $1 - 20$ *sccm*; rf power: $10 - 200$ *W*.

The residence time is defined as

$$\tau_{res} = \frac{pV}{f} \tag{2}$$

where p is the total pressure, V is the chamber volume, f is the gas flow rate. The residence time is about of 31 *s* at the typical values of the process parameters utilized in the work, 10 Pa, 4 *sccm*.

The experimental arrangement used for the investigation of the HMDSO deposition in the plasma of low pressure rf discharge is shown in Figure 4. The plasma reactor is a cylindrical stainless steel vacuum chamber with the volume of 20 *l*. Hexamethyldisiloxane or its mixture with other gases was supplied to the chamber from the side feed line. The data on physical and chemical properties of the monomer are given in Appendix A. The flow rate of the monomer gas was regulated by MKS mass flow controller which is managed by Multi-channel Mass Flow/Pressure Programmer 147B (MKS, USA). The fixed total pressure was maintained by means of the Throttle Valve Controller 652 (MKS, USA) connected with the programmer.

The discharge was powered by rf ACG-5 generator (ENI, USA) coupled to the powered electrode by a fully tuneable π-type matching network. The asymmetrical discharge was maintained between the substrate-carrying powered electrode (8.5 *cm* in diameter) and the grounded wall of the chamber.

Various kinds of substrates were used for thin organic films deposition in the HMDSO plasmas. Si wafers served for analytical purposes, to be more specific, for determination of deposition rate, chemical composition and structure as well as physical properties (optical properties, surface morphology) of synthesized films. Polymer membranes were the base of the composite membranes
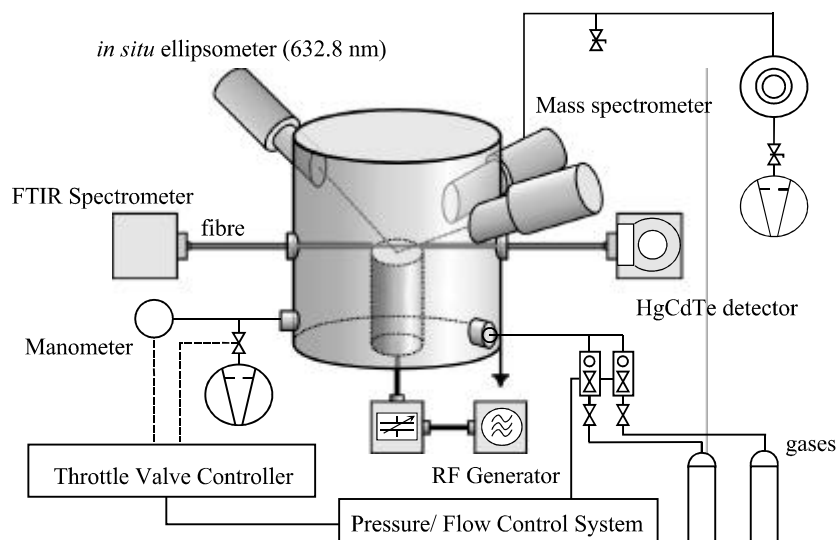
Figure 4. The scheme of the experimental arrangement used for the investigation of
the HMDSO deposition in the plasma of low pressure rf discharge.

fabricated for the study of a gas permeation. Cellulose acetate (CA) membranes (ultrafiltration membranes, 500 MW cut-off, YC05, Millipore) and polyamide 6,6 membranes (microfiltration membranes, 0.1 μm pore size, Pall Gelman Sciences) served as a substrate material for the composite membranes.

3.2   Diagnostics of gas phase

3.2.1   Mass spectrometry

Mass spectrometry has proven to be a powerful method of gas phase and plasma diagnostics. Modern mass spectrometric systems provide a great amount of a valuable information:

— plasma composition (ions, atoms, molecules and radicals);
— particle fluxes to the wall of vacuum chamber or to the electrode surface;
— ion energy distribution functions; plasma sheath properties;
— kinetics of plasma-chemical conversion.

On the other hand, mass spectrometer is an intrusive method, so the diagnostics of bulk plasma causes a plasma disturbance. The interpretation of obtained data is not always strait. High molecular neutrals dissociate in the ion source of mass spectrometer and, hence, a detected fragment ion can have numerous sources. The growth of organic film within mass spectrometer hinders a routine application of this method in reactive plasmas. The special measures have to be followed, e.g. monomer dilution by inert gases.
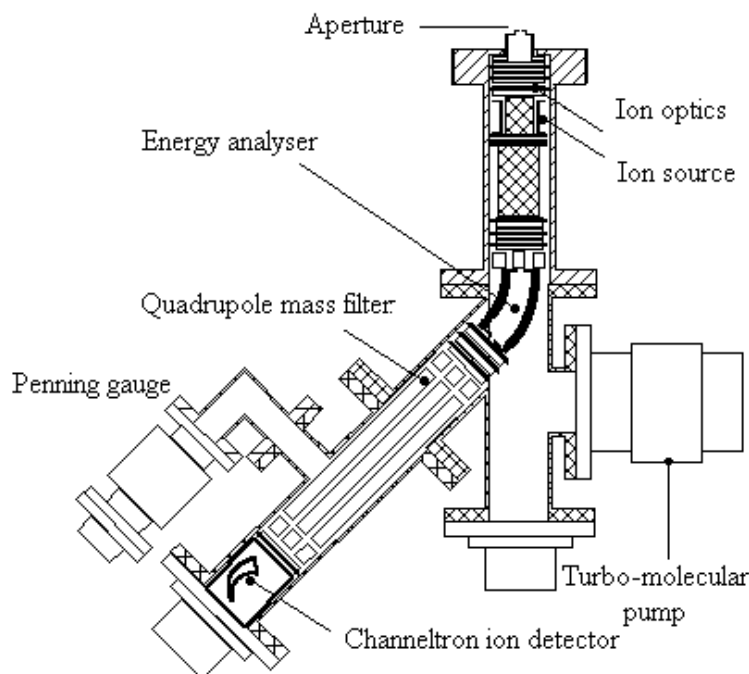
Figure 5. Schematic diagram of the EQP 300 Mass/Energy analyser.

The EQP 300 Mass/Energy Analyser (Hiden Analytical, UK) was used for the mass spectrometric study of the HMDSO plasmas in this work. This plasma monitor represents the combination of ion energy analyser and quadrupole mass filter, see Figure 5.

Discharges utilized for thin organic film deposition are ignited usually at the pressures higher than 10^{-3} Pa. That is why, the common approach to the mass spectrometric diagnostics of such a relatively high pressure environment is to place the mass spectrometer in a separate housing with own vacumm pump, connected with the volume of interest by an sampling orifice with the aperture of appropriate size. The housing of the plasma monitor is differentially pumped by a turbomolecular pump. The flow rate of gas through the 100 μm aperture and pumping speed are arranged to give a background pressure in the housing of about 10^{-6} Pa which is controlled by a Penning gauge used to monitor the differential pumping action and to provide over-pressure protection. The orifice is situated at the distance of about 20 cm from the active plasma zone. Consequently, stable neutral species formed in the plasma and diffusing to the chamber wall can be monitored at such a geometry.

The ions were produced from the neutral particles as a result of electron impact ionization within the ion source of the mass spectrometer. The target gas pressure in the ion source of the mass spectrometer was in the range of $(1-3) \times 10^{-6}$ $mbar$. The hot filament emits electrons which

can be accelerated to the energies of about $5 - 100$ eV. The standard electron energy is 70 eV. This value is associated with the maximum cross-section of electron impact ionization for the most species. The variation of electron energy allows to find the ionization potential of neutrals. The electron emission current is 20 μA.

For analysis of the ions extracted from the plasma boundary sheath in front of electrodes or substrate surfaces (plasma monitoring), the ion source is switched off and formes a field free drift space for these ions. Whereby the necessary potential is set on the transfer lens to refocus the ion beam from the sampling orifice onto the exit aperture of the ion source.

A drift space and an ion optics (lens 2) are used to transfer ions to the input of the 45° sector field energy analyser. The alignment adjustments are realized by the variation of plate voltages, [VERTICAL DEFLECTION] and [HORIZONTAL DEFLECTION]. [QUADRUPOLE] variable serves for the correction of any astigmatism in the ion beam. A decelerating lens, [FOCUS], reduces the kinetic energy of the beam before injection into the quadrupole mass filter. The quadrupole mass filter separates the ions with different mass-to-charge, m/z, values. The mass resolution is controlled by two variables, [DELTAM] and [RES'N].

The ion beam is registered by a continuous dynode electron multiplier which operates in the pulse counting mode. The detector is controlled by three variables: the first dynode voltage, [1STDYN], which is the voltage on the front of the detector; [MULTHT]; which is the voltage across the detector; [DISCRM] which is used to set a counting threshold on the pulse output from the multiplier. The typical values of variables are listed in Table 1.

The intensities of 15 chosen species can be concurrently recorded in the experiments. 100 ms counting time was used what allowed to follow the plasma-chemical conversion with 1.5 s time step from the moment of discharge ignition up to the time when the system reaches a steady state.

[QUADRUPOLE]	Q_1	0.87	[LENS1]	0 V
	Q_2	-0.85	[LENS2]	-70 V
	$Q_{3,4}$	± 1.82	[ENERGY]	1.0 V
[DEFLECTION]	$P_{1,2}$	± 8.10	[ELECTRON ENERGY]	70 V
[DELTAM]		-30%	[SUPPRESSION]	-50 V
[RES'N]		-30%	[FILTER]	-41 V
[MULTHT]		2100 V	[FOCUS]	-70 V
[1STDYN]		-1200 V	[EXTRACTION]	0 V
[DISCRM]		-30%		

Table 1. Typical settings of plasma monitor used in this work.

3.2.2   IR tuneable diode laser absorption spectroscopy

IR tuneable diode laser absorption spectroscopy is a modern, promising technique for non-invasive diagnostics of reactive plasmas. IR absorption spectroscopy allows to identify molecular species (molecules, radicals, molecular ions) and to determine their concentrations in ground states. Moreover, the profile of absorption spectral line lets derive the information about temperature.
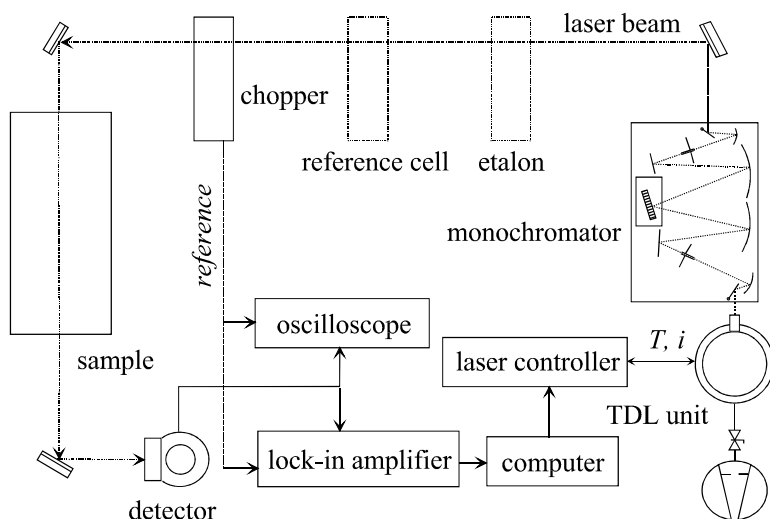
Figure 6. Schematic diagram of the TDLAS module.

Narrow-band tuneable diode lasers emitting in the IR spectral range, $3 - 20$ μm, are used as a light source in this technique. Spatial resolution is limited by a cross-section of laser beam and can be reduced up to the order of mm. The time resolution of ms can be achieved by modern laser spectrometers. This technique is characterized by high selectivity due to high spectral resolution, up to 10^{-4} cm^{-1}, and absorbances of 10^{-4} [23]. A sensitivity of 10^{10} cm^{-3} can be reached for the molecules with sufficiently high line strengths.

The layout of the TDLAS module used in this work is shown in Figure 6. Laser controller sets the operation temperature and the diode current. The temperature of the diode lasers is controlled at milli-Kelvin precision in the range between 25 K and 80 K. The narrow-band infrared emission (line width of about 10^{-4} cm^{-1}) from the TDL source assembly (Mütek Infrared Laser Systems, Germany) first passes a mode selection monochromator and then transmits through KBr windows of the chamber at the height of 12 mm from the powered electrode. MCT-detector registered the transmitted radiation. Direct and second harmonic techniques were used for the absorption measurements. Two types of laser radiation modulation were applied in the case of the direct absorption measurement: chopper modulation and ramp modulation generated by HP33120A Function/Arbitrary waveform generator. The absolute concentration of species X was calculated according to the formula [24]:

$$[X] = (\ln 2/\pi)^{-1/2} \ln(I_0/I_{tran}) \Delta\nu_d/(SL) \tag{3}$$

where I_0 is the laser radiation intensity without absorption, I_{tran} is the transmitted signal intensity, $\Delta\nu_d$ and S are the Doppler HWHM and the line strength, respectively. L is the optical path length for each species of interest.

Second harmonic phase sensitive measurements were performed for small absorption signals by

Species	Transition	Line position [cm^{-1}]	Line strength [$cm/molecule$]	References, remarks
CH_3	Q(3,3)	606.12032	4.46×10^{-19}	[25, 26]
CH_4		3013.7	1.11×10^{-20}	Derived using reference cell
C_2H_2	P(12)	700.9004	1.444×10^{-19}	
C_2H_6		2999.5	2.45×10^{-21}	Derived using reference cell
N_2O	R(19)	606.146055	6.05×10^{-22}	[27]
CO_2	P(25)	701.018014	2.129×10^{-21}	[27, 28]

Table 2. The spectroscopic data of the reference gases and the low weight molecular hydrocarbon products of the HMDSO plasma-conversion which were studied in this work.

means of a SR830DSP lock-in amplifier (Standford Research Systems, USA). In this case the total laser power cannot be measured directly. Instead of that the absorption peak heights of the species of interest have to be calibrated against the corresponding peak heights of a substance of known concentration from the reference cell. In this case the unknown concentration of species X is determined as follows [24]:

$$[X] = (\Delta\nu_{d(x)}/\Delta\nu_{d(ref)})(A_x/A_{ref})(S_{ref}L_{ref}/(S_xL_x))[Y] \qquad (4)$$

where A_x is the absorption peak height of the species of interest and A_{ref} is the height of the reference absorption line, [Y] is the known concentration of the gas in the reference cell.

Below is the detailes on the measurement of the species of interest. Table 2 gives the absorption lines of the species of interest, their position and line strengths.

Methyl radical, CH_3
The CH_3 radical was monitored using Q(3,3) transition of ν_2 fundamental band around 606 cm^{-1}. The peak height of the absorption line was calibrated against the R(19) line of N_2O at 606.146 cm^{-1}. The second harmonic technique as well as the direct measurement were used for the spectra processing. The latter technique was found to be optimal because of the poor laser stability under even very small influence of the rf generator. Representative TDL absorption spectra of the CH_3 radical is shown in Figure 7(a).

As shown in [24] it is possible to use an experimental line width instead of the Doppler's one in the equation (4). The experimental HWHM of N_2O reference line $\Delta\nu_{exp}(N_2O) = 0.00305$ cm^{-1} was estimated by fitting. For the CH_3 radical the Doppler broadening was taken at the temperature of 500 K [29], $\Delta\nu_{exp}(CH_3) = 0.00125$ cm^{-1}. It was assumed that the methyl radical is present only in the rf electrode region of the characteristic dimension of about 14 cm and therefore this value was chosen as the optical path length L.

Methane, CH_4; Ethane, C_2H_6
Methane was monitored using line at 3014.7 cm^{-1}. The calculations were performed measuring the same absorption line obtained by means of the methane reference cell. C_2H_6 monitoring line at the 2999.5 cm^{-1} was not identified. Both measurement techniques were applied. Parameters for calculations: Doppler HWHM at 300 K $\Delta\nu_{exp}(CH_4) = 0.00362$ cm^{-1}, $\Delta\nu_{exp}(C_2H_6) = 0.002631$ cm^{-1}, optical path length $L = 30$ cm (the stable molecules were assumed to diffuse into the whole
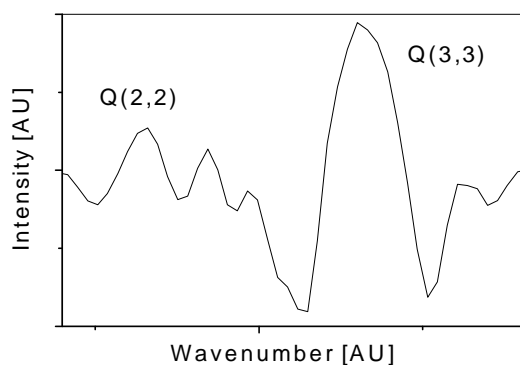
Figure 7(a). The TDL absorption spectra of the CH$_3$ radical in the HMDSO plasma. (15 Pa, 60 W, 5 $sccm$ HMDSO, 5 $sccm$ Ar)
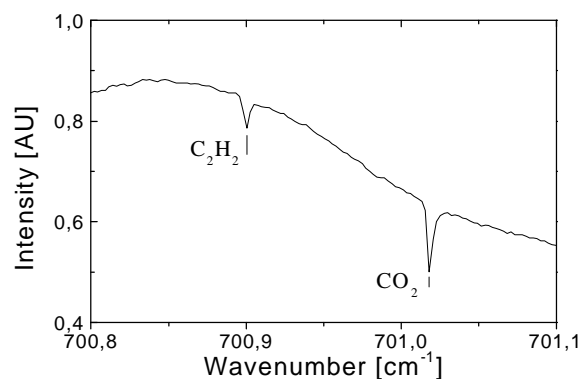
Figure 7(b). The TDL absorption spectra of the C$_2$H$_2$ molecule in the HMDSO plasma. (15 Pa, 120 W, 5 $sccm$ HMDSO)

vacuum chamber).

Acetylene, C$_2$H$_2$

The absorption line P(12) at 700.9004 cm^{-1} was used for the determination of the C$_2$H$_2$ concentration. Only direct measurement technique could be applied because of the relatively high line intensity. Nevertheless, second derivative measurements were performed also in order to improve the precision of measurements. Representative spectrum is shown in Figure 7(b). The monitoring line is marked. Bold line, as ever, show the absorption in reference gas cell. CO$_2$ lines come from the CO$_2$ reference cell and they were used for acetylene line identification.

3.3   Thin organic film characterization

The focus of this work lies on surface and thin film diagnostics of plasma polymerization. Moreover, FTIR spectroscopy was chosen as a base for the novel technique to be developed. That is why, the methods of characterization of thin films, which can be used for *in situ* study of the process also, are considered in details here.

3.3.1   Fourier transform infrared spectroscopy

Infrared spectroscopy provides information on molecular vibrations which are excited by radiation in selected spectral regions. A vibrational mode is IR-active when there is a change in the molecular electrical dipole momentum during the oscillation. Molecules with a centre of symmetry have no fundamental lines in the IR spectrum. The theory of IR transitions have been discussed by many authors in detail [30 − 33].

In comparison with conventional IR spectroscopy the FTIR technique allows one to measure concurrently all frequencies in the chosen spectral range. It is possible due to the interferometer. The

principal scheme of the Michelson interferometer used in the most commercial FTIR spectrometer is shown in Figure 8. It consists of two mutually perpendicular plane mirrors. One of them (M1) is fixed and the other (M2) can move along the axis which is perpendicular to its plane. The infrared radiation emitted by a source, S, falls onto the beamsplitter, BS, where the infrared beam is partially reflected to the mirror M1 and transmitted to the mirror M2. After both space coherent beams returns to the beamsplitter, they interfere and are again partially reflected and partially transmitted. The path difference is equal to $2x$ where x is the M2 mirror displacement. The modulated output beam transmits the sample section and is focused on a detector. The detector measures the intensity of the infrared radiation as a function of the mirror displacement - the interferogram. For polychromatic source the measured interferogram is the resultant of the inerferograms corresponding to each wavelength. In such a case the interferogram can be represented by the integral [34, p.8]:

$$I(\delta) = \int\limits_{-\infty}^{+\infty} B(\overline{\nu}) \cos 2\pi\overline{\nu}\delta \cdot d\overline{\nu} \tag{5}$$

which is one-half of a cosine Fourier transform pair. The other is expressed in a following way:

$$B(\overline{\nu}) = \int\limits_{-\infty}^{+\infty} I(\delta) \cos 2\pi\overline{\nu}\delta \cdot d\delta \tag{6}$$

For the monochromatic radiation the parameter $B(\overline{\nu})$ gives the intensity of the source at a wavenumber $\overline{\nu}$ as modified by the instrumental characteristics. The spectrum is calculated from the inteferogram by computing the cosine Fourier transform of $I(\delta)$. While $I(\delta)$ is an even function, the equation (6) can be rewritten as:

$$B(\overline{\nu}) = 2 \int\limits_{0}^{+\infty} I(\delta) \cos 2\pi\overline{\nu}\delta \cdot d\delta \tag{7}$$
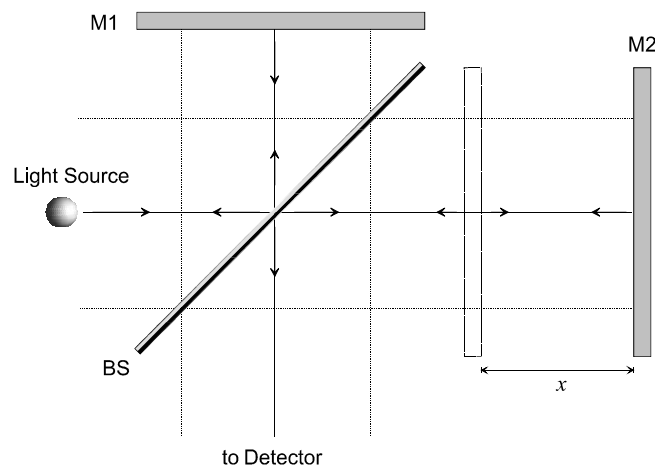

Figure 8. The principal scheme of the Michelson interferometer.

From the equations (5) and (7) follows that the spectrum can be measured at infinitely high resolution: $\overline{\nu}$ varies from 0 up to $+\infty$. However, in order to realize this one should scan the movable mirror of the interferometer an infinitely long distance: δ varies from 0 up to $+\infty$ (7). In practice the signal measurement can be carried out only with the limited retardation what causes the spectrum has a finite resolution. The restriction of the maximum retardation of the interferogram to Δ means that the complete interferogram is multiplied by a truncation function $D(\delta)$:

$$
\begin{aligned}
D(\delta) &= 1 & if \quad -\Delta \leq \delta \leq +\Delta \\
D(\delta) &= 0 & if \quad \delta \succ |\Delta|
\end{aligned}
\tag{8}
$$

In this case the spectrum is given by the expression:

$$
B(\overline{\nu}) = \int\limits_{-\infty}^{+\infty} I(\delta)D(\delta)\cos 2\pi\overline{\nu}\delta \cdot d\delta
\tag{9}
$$

The equation (9) shows that the true spectrum $B(\overline{\nu})$ (or the Fourier Transform (FT) of $I(\delta)$) is convolved with the sinc function $2\Delta\mathrm{sinc}2\pi\overline{\nu}\Delta$ which is the FT of $D(\delta)$.

The convolution with the sinc function results in the strong side lobes in the interferogram. Suppression of the magnitude of these side lobes is known as apodization. Series of apodization functions have been studied. The apodization functions used in this work are summarized in Table 3.

Norton-Beer	$A(\delta) = \sum\limits_{i=0}^{n} C_i \left[1 - \left(\frac{\delta}{\Delta}\right)^2\right]^i$	[35]
Happ-Genzel	$A(\delta) = 0.54 + 0.46\cos\left(\pi\frac{\delta}{\Delta}\right)$	[34]
Boxcar	$A(\delta) = D(x) \equiv \left\{\begin{smallmatrix} 1, & |x| \preceq L \\ 0, & |x| \succ L \end{smallmatrix}\right.$	[34, 36]

Table 3. Series of apodization functions.

Norton and Beer showed that there is a distinct empirical boundary relation between the full width at half-height (FWHH) and the side lobe amplitude [35]. The narrower is the FWHH, the greater is the side lobe amplitude. The use of the specific apodization function depends on the experiment being performed. A function like the Norton-Beer weak function should be applied, if either high resolution or an accuracy for the quantative analysis is required. Stronger apodization functions can be applied for spectra containing both weak and intense bands, especially when their width is comparable with the instrumental resolution.

The absorption of the infrared radiation at any wavelength by a homogenious medium is defined quantatively by the Beer-Bouguer-Lambert law:

$$
A(\overline{\nu}) = \log(I_0/I) = a(\overline{\nu})dc
\tag{10}
$$

where $A(\overline{\nu})$ is the absorbance (also known as extinction), I_0 is the intensity of the entering radiation, I is the intensity of the transmitted after the sample absorption radiation, $a(\overline{\nu})$ is the absorptivity at $\overline{\nu}$ (or molar extinction coefficient), d is the pathlength (or the sample thickness), c is the concentration of the sample. Thus, it is possible to calculate the concentration of the absorbing medium when the molar extinction coefficient is known. The value of the $A(\overline{\nu})$ depends also on the instrumental parameters. That is why, the integral absorbance can be used instead of the maximal absorbance in the quantative analysis [37].

The following integration method was applied in this work. The boundary frequencies of the absorption band of interest are chosen and the baseline is drawn, see Figure 9. The baseline is determined by totally 4 points which are the points of the local baseline of the overall absorption spectrum. Then the band area over the chosen baseline is calculated.

As a concluding remark here is the list of the advantages of the FTIR technique in comparison with the ordinary IR spectroscopy:

— Multiplex- or Fellgett-advantage: it is possible to measure at all the wavelengthes of chosen spectral range;
— Jacquinot-advantage: more radiation goes through the round blends of the FTIR spectrometer in comparison to the split of the grade based IR spectrometer;
— Connes-advantage: applied in FTIR spectrometer HeNe-laser allows to set a wavelength with a very high accuracy, $< 0.01 cm^{-1}$.
— very short time of measurement;

The polymeric films can be analysed by different FTIR spectroscopic techniques: transmission
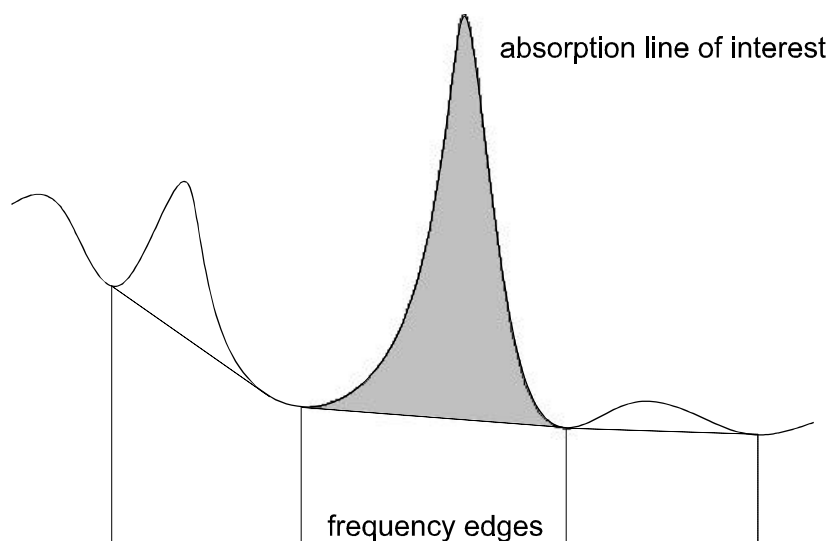

Figure 9. The integration type used in this work for calculation of the integral absorbance.

spectroscopy, reflection-absorption spectroscopy, attenuated total reflection spectroscopy, etc. The first one deals with the measurement of an apperent IR radiation intensity passed through the film of interest, since transmission of radiation actually involves numerous absorptions and reemissions. The reflection of IR radiation falling on the sample surface should be taken into account for correct measurements of IR spectra.

Reflectance spectrum can be obtained by two types of measurements. The term specular reflectance applies to the measurement of the reflectance spectrum of a surface of an absorbing material. The term reflection-absorption spectroscopy (IRRAS) is used for the measurement which involves a double pass through a thin surface film on a highly reflective (metallic) surface, [38]. The analytical description of reflection-absorption spectroscopy considers the propagation of the electric fields in a three-phase, optically isotropic medium. Reflection occurs at the planar, parallel optical boundaries between media. The typical system of interest consists of three media: air, thin film of interest and substrate medium (metallic thick film). The degree to which IR radiation is reflected or transmitted at an interface depends on the polarization and angle of incidence of the falling radiation as well as the optical constants of two adjacent media.

Attenuated total reflection spectroscopy (ATR) is based on a phenomenon called total internal reflection, [39] and chapter 4 of this work: when radiation passes into a medium with higher refractive index than the surrounding one, it will be trapped inside, if the angle of reflection at the surface of the medium exceeds a "critical angle". A standing wave is established at the reflecting interface. The radiation is reflected at the interface at the proper conditions and propagates through the medium.

3.3.2   Ellipsometry

Ellipsometry is one of very effective methods for thin film characterization. This technique allows one to obtain the information about thickness, optical and electrical properties of the analysed films. In dependence upon the wavelength of the radiation the ellipsometric measurements can be performed in the various spectral regions: UV, visible and infrared.

The polarization state of the radiation will change as a result of the light interaction with a solid. The alteration of the radiation intensity and the displacement of the phase angle between parallel and perpendicular to the plane of incidence components of the polarized light are measured by an ellipsometer. The following data processing based on the very well developed mathematical description of the light propagation through the ellipsometer units (polarizer, compensator, etc) assumes the fitting procedure of the experimentally measured parameters (so-called ellipsometric angles Ψ and Δ) according to the physical model describing the analysed system (a half-continuous solid state, stratified medium, etc). Whereby one solves a reverse problem: determination of the material parameters from the alterations of the intensity and the phase of the reflected light. The theory used in the ellipsometry as well as often applied dispersion models are very detailed described by Azzam and Bashara [40].

The electromagnetic waves are represented ordinarly only by the electric field component in
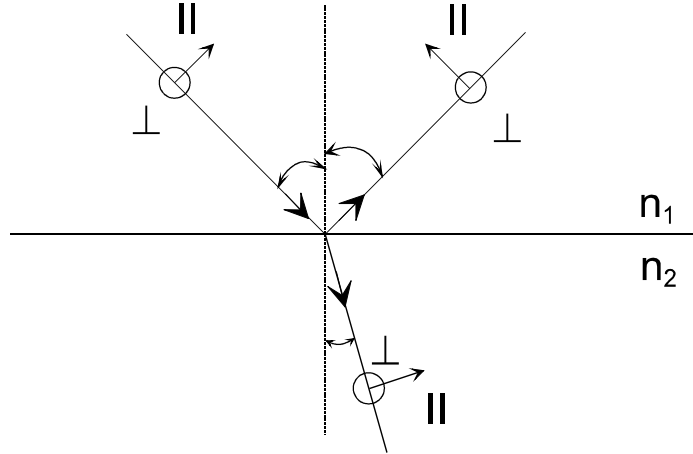
Figure 10. Reflection of light beam on the boundary of two media.

the optics because the influence of the magnetic field on electrons of the solids is much weaker than that of the electric fields. In the cartesian coordinate system a transverse electromagnetic wave propagating in z-direction can be expressed by the superposition of two linearly polarized perpendicular to each other waves:

$$E_x = E_{0x} \exp i(\omega t + \delta_x) \tag{11}$$

$$E_y = E_{0y} \exp i(\omega t + \delta_y) \tag{12}$$

in the form $\overrightarrow{E} = \overrightarrow{E}_x + \overrightarrow{E}_y$. Where $\delta_{x,y}$ are the phase angles, $E_{0x,y}$ are the amplitudes. For an ellipsometer the coordinate system is chosen in such a way that one axis is parallel to the plain of incidence, $\parallel$, and the other $-$ perpendicular, $\perp$. The polarization state of the wave can be described in various but equivalent ways [41, 42], e.g. by the amplitudes ratio and phase displacement:

$$E_{0\parallel}/E_{0\perp} = \tan \Psi_W \tag{13}$$

$$\delta_\parallel - \delta_\perp = \Delta_W \tag{14}$$

and

$$E_\parallel/E_\perp = \tan(\Psi_W) \exp(i\Delta_W) \tag{15}$$

Figure 10 shows the reflection of electromagnetic wave on the boundary of two media with complex refractive indices n_1 and n_2.

According to the Fresnel theory the reflection properties of a sample can be described by means of the reflection coefficients R [43]. Parallel and perpendicular components of the incident (i) and reflected (r) electric field strength are correlated in this way:

$$E_{\parallel,\perp}^r = R_{\parallel,\perp} E_{\parallel,\perp}^i \tag{16}$$

The change of the polarization state as a result of the reflection is expressed by the ratio of the parallel and perpendicular components of the reflection coefficient $R_{p,s}$:

$$\rho = R_\parallel/R_\perp = \tan \Psi \exp(i\Delta) \tag{17}$$

The values Ψ and Δ are so-called ellipsometric angles. The first ellipsometric angle, Ψ, describes the change of the ratio of the amplitudes as a result of the reflection, while the ellipsometric angle, Δ, corresponds to the phase difference between the parallel and perpendicular components of the electric field.

Note, that $\rho = f(\lambda, \phi, n, d)$ and, thus, the thickness d and the refractive index n of the film of interest can be obtained from (17) by the solving of the reverse problem,

$$\begin{aligned} n &= g(\tan\Psi, \exp(i\Delta)) \\ d &= h(\tan\Psi, \exp(i\Delta)) \end{aligned} \qquad (18)$$

The d- and n-values are calculated with the help of the experimentally measured ratio (17). The important issue of this calculation is the physical model of the analysed system. One should define the substrate, the number of layers and the dispersion models for every layer. The ellipsometric angles (Ψ, Δ) calculated for a chosen model numerically are fitted to measured ones. The film material is described here by an appropriate dispersion model. The models used in the ellipsometry are summarized in Table 4 below.

There are two main types of the ellipsometric techniques:
— Null-ellipsometry;
— photometric ellipsometry.

Model	Dispersion relation	Remarks
Lorentz	$n^2 = 1 + \sum\limits_i \frac{A_i\lambda^2}{\lambda^2 - \lambda_{0i}^2 - iC_i}$ A_i, C_i, λ_{0i} are the constants	description of the resonant absorption peaks; suits for various materials; [40, 42]
Sellmeier	$n^2 = 1 + \sum\limits_{i=1}^{N} \frac{A_i\lambda^2}{\lambda^2 - \lambda_{0i}^2}$	suits for the region of the normal dispersion; good description of amorphous dielectrica; [40, 43]
Cauchy	$n = n_0 + \frac{n_2}{\lambda^2} + \frac{n_4}{\lambda^4}$ $k = k_0 e^{(\frac{1}{\lambda} - \frac{1}{\lambda_0})}$ n_i, k_0, λ_0 are the constants	good description of dielectrica and semiconductors; [40, 44]
effective medium models		
Lorentz-Lorentz	$\frac{\varepsilon - 1}{\varepsilon + 2} = f_1 \frac{\varepsilon_1 - 1}{\varepsilon_1 + 2} + f_2 \frac{\varepsilon_2 - 1}{\varepsilon_2 + 2}$ $\varepsilon = n^2$; $f_{1,2}$ is the volume part of the appropriate admixture	mixture on the atomic level; [45]
Maxwell-Garnett	$\frac{\varepsilon - \varepsilon_1}{\varepsilon + 2\varepsilon_1} = f_2 \frac{\varepsilon_2 - \varepsilon_1}{\varepsilon_2 + 2\varepsilon_1}$	mixture of domains with ε_i; [41]
Bruggemann (Effective Medium Approximation)	$0 = f_1 \frac{\varepsilon_1 - \varepsilon}{\varepsilon_1 + 2\varepsilon} + f_2 \frac{\varepsilon_2 - \varepsilon}{\varepsilon_2 + 2\varepsilon}$	f_1 and f_2 are comparable; good description of the surface roughness

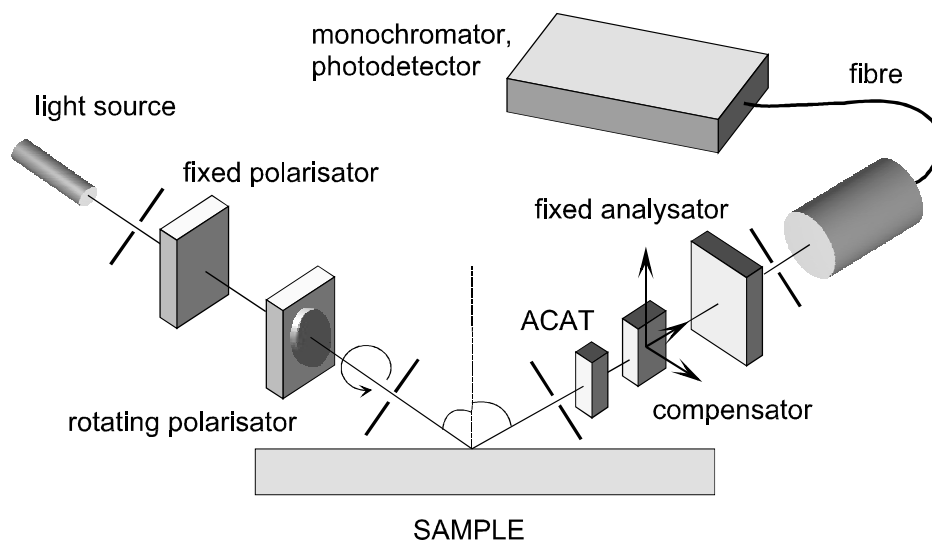Table 4. The dispersion models used in the ellipsometry.

Figure 11. The principal scheme of the spectroscopic ellipsometer used in this work.

The first one assumes the determination of the ellipsometric angles at the positions of polarizator, compensator and analysator at which the signal intensity measured by detector is zero or minimum. Null-ellipsometry is a very precise technique: the accuracy of measurement is defined only by mechanical components and their adjustment. The disadvantage of the method consists in the long period of time in order to get the necessary position of the elements. This time is comparable with the total measurement time by photometrical ellipsometer.

In the photometric ellipsometry the radiation intensity is measured as the function of periodically modulated parameter (azimuth-angle of polarizator or analysator, displacement of the phase angle). There are two main types of the photometric ellipsometer: with rotating analyser or with rotating polarizer.

The use of the polychromatic radiation source allows one to measure the ellipsometric values (Ψ, Δ) in dependence upon the wavelength. Spectroscopic ellipsometer makes the analysis of the systems consisting from many layers possible [40, 41]. The principal scheme of the spectroscopic ellipsometer SD2200 (Rudolf Research, USA) used in this work is shown in Figure 11.

Application of *in situ* ellipsometer with time resolution, e.g. of about 1 s, allows one to study the process kinetics. Here, the rates of the film deposition on Si wafers placed on the powered electrode were measured by *in situ* SD2200 ellipsometer (Philips Analytical Technology GmbH, Germany) at the wavelength of 632.8 nm. Thin films were also deposited on Si substrates (1.5 cm × 1.5 cm) in the plasma at the various distances from the rf electrode. These films were *ex situ* tested by S2000 spectroscopic (300 − 800 nm) ellipsometer (Rudolph Technologies, USA). The obtained data were analysed and fitted by WVASE software (Woolam, USA). The ellipsometric measurements of a film thickness allowed one to estimate the deposition rate. Moreover, the dispersion relations of refractive index and extinction coefficient were obtained from the ellipsometric data with the use

of Sellmeier and Cauchy optical models. The two layer system was simulated including the plasma deposited HMDSO thin filmand an interface from natural SiO_2 on Si substrate.

Besides film thickness and optical properties ellipsometric measurements can also provide the information about the band gap energy for photoconducting materials or semiconductors. Two types of electron delocalization are possible in the organosilicon conpounds composed of σ- and π-systems. σ-electrons of the Si-Si bonds can delocalize through the main chain. In the polymers composed of alternating arrangements of σ- and π-systems, σ-electrons can also delocalize through the π-systems ($\sigma - \pi$-delocalization). The electronic structure of such amorphous systems (polymers, glasses, etc.) can be considered with the help of band models [44 − 47]. The model of optical absorption in amorphous semiconductors was first introduced by Tauc [46]. His model contains the following assumptions:

− the amorphous semiconductors can be described by valence and
  conduction bands separated by a gap;
− there is no mixing of valence- and conduction-band wave functions due to positional disorder.

The additional assumptions should be done to describe non-direct optical transitions: there is no conservation of electron momentum in the disordered amorphous semiconductor. The absorption constant due to optical transitions is correlated with the optical band gap in the following way [46]:

$$(\alpha E)^{1/2} = \beta(E - E_g) \tag{19}$$

where α is the absorption coefficient, β is a constant, E is the photon energy, E_g is the optical band gap. The Tauc plot giving the value $(\alpha E)^{1/2}$ as a function of the radiation energy in the visible spectral range provides the value of the band gap.

3.3.3   Manometric measurement of gas permeation

Gas permeation through a polymeric membrane is defined by the properties of the gas of question (characteristic molecule size, chemical potential, dipole moment, etc) and by the parameters of the membrane material (porosity, pore size, etc) as well as by the interaction between the permeate and the polymer matrix. The polymeric membranes can be tested relative to the permeability of gas mixtures or pure gases. The interaction among single mixture components should be taken into account in the analysis of the gas mixture permeation. The gas permeation through a membrane is characterized by a permeability coefficient, $Perm$, which determines the gas amount passing through a membrane of the unit area for the unit time. The ideal selectivity of the membrane according to the gas pair A and B is defined as the ratio of the appropriate permeability coefficients, $\alpha = Perm_A/Perm_B$. Unfortunately, for any separation, the selectivity and the permeability tend to be inversely related: membranes exhibiting highest selectivities have low permeabilities and vice versa.

The gas permeation through non-porous polymer membranes is considered in terms of both thermodynamics of gas solution in polymers and kinetic mobility of gas molecules in polymers. Gas permeation through a polymer membrane is expressed in the following way [50 − 52]:

$$Perm = D \times \sigma \tag{20}$$

where D is the diffusion coefficient, σ is the solubility coefficient. The selectivity due to solubility is determined by the chemical interaction between gas molecules and polymer chains. The ability of polymeric film to let through gas molecules respectively their sizes and forms determines the selectivity due to kinetic mobility of gas molecules.

The gas transport mechanism for the membranes with relatively big pore sizes can be described by the Knudsen flow:

$$J_{Knudsen} = \frac{\pi n r^2 D_k}{RT\tau_{pore}} \frac{\triangle p}{d} \tag{21}$$

where $J_{Knudsen}$ is the gas flux, D_k is the Knudsen diffusion coefficient, $\triangle p$ is a pressure gradient, d is the membrane thickness, r is a pore radius, n is the number of pores, τ_{pore} is a pore tortuosity (for cylindrical perpendicular pores $\tau_{pore} = 1$ [51]), T is the gas temperature.

The Knudsen diffusion coefficient is given by [51]:

$$D_k = 0.66r\sqrt{\frac{8}{\pi}\frac{RT}{M_W}} \tag{22}$$

where M_W is the molecular weight.
The membrane flux J can be expressed also in terms of the permeability coefficient:

$$J = Perm \cdot \triangle p / d \tag{23}$$

Taking into account (21) and (23), it can be deduced that ideal selectivity is proportional to the ratio of Knudsen diffusion coefficients of appropriate gases: $\alpha(\text{A/B}) \sim D_k(\text{A})/D_k(\text{B})$. Ideal selectivity is determined by the square root of the ratio of the molecular weights of gas molecules and characteristic sizes of gases molecules. The typical value for O_2/N_2 is 0.98 in the case of Knudsen mechanism.

Gas permeability coefficients can be measured via manometer method [50, 53 − 55] based on the measurements of the amount of gas that passed through a membrane, see Figure 12. The tested membrane is placed on the plate of porous metal with a permeability considerably higher than that of membranes. The cell is sealed by using the vacuum rubber ring. The membrane divide the cell into two parts. The first one is under the gas pressure (from 10 to 50 Pa), the second part is pumped to 10^{-4} Pa. The increase of pressure in the second part is monitored by the pressure controller. The gas permeability is calculated according the following expression:

$$Perm = \frac{V \cdot d}{\triangle p \cdot A \cdot RT}\left(\frac{dp_2}{dt}\right)_{steady\ state} \tag{24}$$

where V is the cell volume at the downstream side of the membrane, d is the membrane thickness, A is the active surface of the membrane, $\triangle p$ is the pressure difference between the upstream and the downstream sides of the membrane, dp_2 is the pressure increase in the second part of the cell. The sensitivity of this method is in the order of magnitude $10^{-10}cm^3 \cdot cm/(cm^2 \cdot s \cdot cmHg)$ [55].

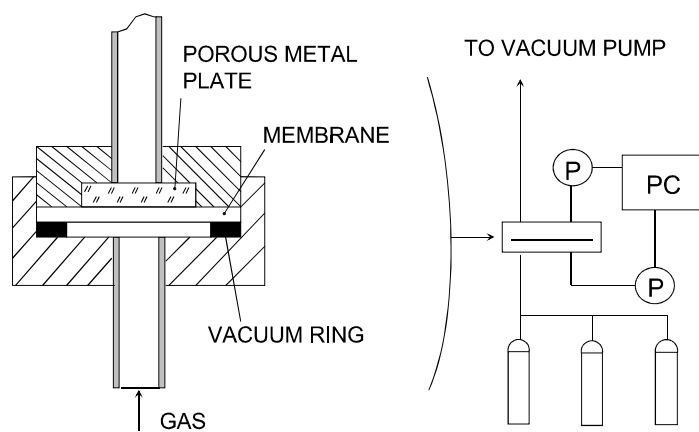Figure 12. The schematic representation of the measurement of gas permeability through a polymeric membrane.

Development of novel *in situ* fibre based FTIR diagnostic tool

4.1 Evanescent wave spectroscopy

A novel FTIR diagnostic tool is based on evanescent wave spectroscopy. EWS assumes the use of tiny optical fibres as a medium for radiation transmission and as an active probe which should be placed in the process vessel. The analysis of the theory of evanescent wave spectroscopy and the theory of optical waveguides let clear up the following issues:

— fibre and measurement parameters which determine the sensitivity of the technique;

— potential advantages and drawbacks as well as method limitations;
— possible ways of technique optimization.

Evanescent wave spectroscopy is related to internal reflection spectroscopy (IRS) which is more widely known as attenuated total reflection (ATR) spectroscopy. ATR spectroscopy is carried out at a single fixed incidence angle at the surface between internal reflection element and the medium in question. The optical fibres are the main optical element of the method. The fibres are illuminated by the collimated light beam. Thus, there is a random ensemble of angles at which the radiation propagates in the fibre core and, hence, a more complex description of the resulted spectrum is required.

4.1.1 Fibre optics

The simplest optical fibre consists of the cylindrical core of radius ρ surrounded by the protecting cladding. The light beam is transmitted through the fibre as a result of the total internal reflection. The radiation approaching the interface from the denser medium is totally reflected if the angle of incidence at the reflection surface exceeds the critical angle θ_c obeying:

$$\sin \theta_c = n_{pp}/n_c, \tag{25}$$

where n_{pp} is the refractive index of the rarer medium (plasma polymer here), n_c is the refractive

index of the denser medium (fibre core here), thereto $n_c > n_{pp}$. When the ratio ρ/λ is large ($\rho \gg \lambda$) the light propagation in the fibre can be described by geometric optics, i.e. a light power propagates along the trajectories determined by the ray-path equations. The wavelength, λ, of the considered mid-IR radiation lies in the range of $3-16\ \mu m$, so the fibre should have the radius of hundreds microns.

The rays entering and propagating in the fibre core are bounded by the core within a limited solid angle of incidence defined by θ_0:

$$n_{air} \sin \theta_0 = n_c \sin \theta_c \quad \Longrightarrow \quad n_{air} \sin \theta_0 = n_c (2\Delta)^{1/2} \tag{26}$$

where $n_{air} \simeq 1$ is the refractive index of air. The quantity $n_c(2\Delta)^{1/2}$ is called by the numerical aperture (NA) of the fibre. It can be shown that no any ray with $\theta < \theta_c$ propagates along the fibre, but only a discrete number of modes. This number, in a step-index fibre, is determined by a fibre parameter ("V-number") [56, 57]:

$$V = \frac{2\pi\rho}{\lambda} \left(n_c^2 - n_{cl}^2 \right)^{1/2} = \frac{2\pi\rho}{\lambda} n_c (2\Delta)^{1/2} \tag{27}$$

Thus, in terms of the fibre parameter: the ray analysis can be applied to multimode waveguides with $V \gg 1$. The V-numbers of the fibres used in this work vary in the range of $250 - 3749$. Both criteria, ($\rho \gg \lambda$, $V \gg 1$) are fulfilled and, consequently, the ray analysis can be used here.

The axisymmetric refractive-index profile $n(r)$ is either uniform or graded over the core. The step-graded fibres used for the evanescent wave spectroscopy have the profile of the refractive index defined by:

$$n(r) = n_c, \quad 0 \le r < \rho; \qquad\qquad n(r) = n_{cl}, \quad \rho < r < \infty \tag{28}$$

Note, that $n_c > n_{cl}$. The rays which cross the fibre axis between reflections are known as meridional rays (M). The rays which never cross the fibre axis and propagating in a helical-like path are known as skew rays (S), see Figure 13. The meridional rays are described by the angle θ between the path and the x-direction, while for the description of the skew rays second additional angle is used: θ_ϕ is the angle in the core cross-section between the tangent to the interface and the projection of the ray path.

The angles θ and θ_ϕ are spherical polar angles relative to the axial direction AB. The path length l_{AB} from A to B is calculated from geometry [56]:

$$l_{AB} = 2\rho \frac{\sin \theta_\phi}{\sin \theta}, \tag{29}$$

here the skew ray paths are also included. The optical path length L_{opt} is, consequently, equal to $l_{AB} = 2\rho n_c \frac{\sin \theta_\phi}{\sin \theta}$. The number of reflections per unit length of fibre, N, is given by:

$$N = \frac{1}{L_{AB} \cos \theta} = \frac{\tan \theta}{2\rho \sin \theta_\phi}. \tag{30}$$
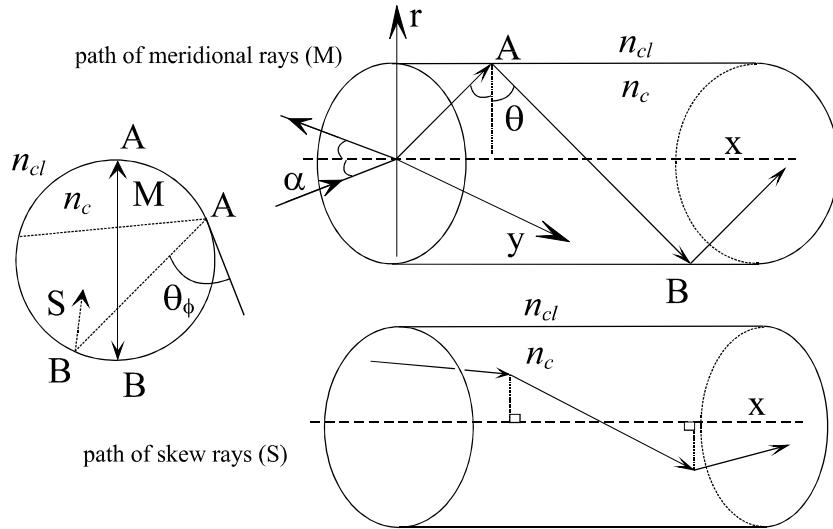
Figure 13. Ray paths within the core of a step-index fibre.

Assuming that the angles θ and θ_ϕ are constant (fibres with homogeneous core, without bending), one can find the ray transit time τ_{ray}, h.e. the time taken for a ray to travel distance x along a fibre, for step-profile fibre:

$$\tau_{ray} = xN\frac{L}{c} = \frac{x}{c}\frac{n_c}{\cos\theta}.$$ (31)

Note, that the ray transit time depends only on the axial angle θ.

An optical signal transmitted along the fibre can be distorted because of the dispersion. It is convenient to distinguish the following dominant mechanisms: intermodal and intramodal dispersion. The first kind of dispersion is present whenever more than one mode is excited in the fibre. The modes with steeper angles of incidence θ (typically the higher-order modes) propagate more slowly along the fibre than those with less steep angles. The energy pulse of the initial signal is broadened. The intramodal dispersion occurs because of the Fourier transform of the single mode which is composed of a distribution of propagating waves with $\lambda \pm \Delta\lambda$. Every spectral component undergoes the appropriate time delay. Intramodal dispersion contains generally the contributions from the core material ($dn/d\lambda$) and from the mode guiding ($d\theta/d\lambda$). The former is referred to as material dispersion and the latter as waveguide dispersion, as if the two were independent.

The ultimate limiting transmission loss of optical fibres is expressed by the sum of losses due to scattering and absorption. Both processes are present even in highly pure and structurally perfect materials (intrinsic losses). The frequency region of maximum intrinsic transparency in glasses and crystals is known as the optic window. On the long-wavelength (far IR) side it is limited by absorption from polar modes of lattice vibration (the multiphonon edge). For chalcogenide glasses the attenuation caused by the multiphonon edge lies outside of $10\mu m$ wavelength. On the short-wavelength side the optic window is bounded by absorptions from electronic band gap (valence to conduction band) excitations (Urbach tail). The other source of the power attenuation on the

short-wavelength wide is the scattering (mainly Rayleigh scattering). Besides such loss mechanisms mentioned above, there are also the macroscopic losses due to bending of the fibres, imperfectness of the core cross-sections, etc. These losses as well as the dispersion do not influence crucially the application of the optical fibres in the evanescent wave spectroscopy. The absorption spectrum of a thin film deposited on the active part of the core is taken in regard to the background spectrum of the fibre and, thus, represents the difference spectrum.

4.1.2   Principles of evanescent wave spectroscopy

While evanescent wave spectroscopy is a case of ATR technique, the main issues of the theory of the latter are suitable for the EWS also. As it follows directly from the name of ATR technique, the effect of the total internal reflection lies in the basis of this method. The theory of ATR spectroscopy can be described in both rigorous (in terms of the Maxwell's equations) and non-rigorous (in terms of the classical equations of Fresnel and of Snell's law) ways. From Maxwell's equations it can be found that a standing wave normal to a totally reflecting surface is established in the dense medium because of the superposition of the incoming and reflected waves. The amplitude of the electric field component E_y perpendicular to the plane of incidence is given by [58]:

$$E_y = 2i \cos(k_r r + \phi_y), \tag{32}$$

where $k_r = (n_c \omega / c) \cos\theta$ and $\cos\phi_y = \cos\theta / \sqrt{1 - (n_{pp}/n_c)^2}$.
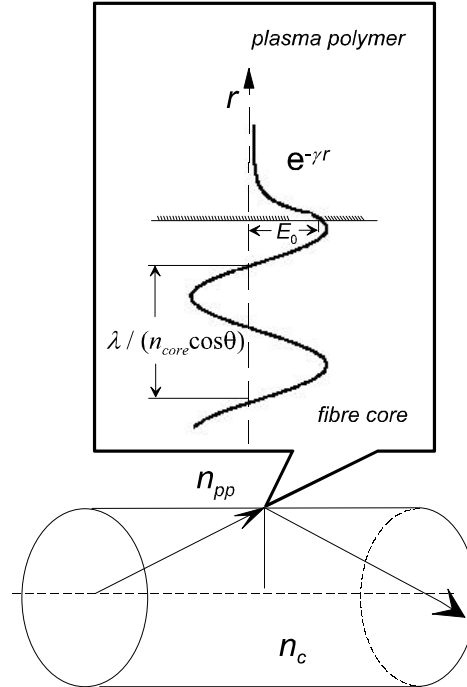

Figure 14. Evanescent wave penetrating into the rare medium (plasma polymer) and standing cosine wave in the denser medium (fibre core).

The electric field component polarized parallel to the plane of incidence becomes elliptically polarized after the reflection. The electric field amplitude can be represented by its components:

$$E_x = 2\cos\theta\cos(k_r r - \phi_x), \tag{33}$$

and

$$E_r = 2i\sin\theta\cos(k_r r - \phi_r), \tag{34}$$

where $\cos\phi_x = [1 + k_r/(\gamma n_c/n_{pp})^2]^{-1/2}, \cos\phi_r = [1 + (\gamma n_c/n_{pp})^2/k_r]^{-1/2}$. When total internal reflection occurs, the electromagnetic field penetrating into the rarer medium decays exponentially in amplitude with distance from the reflecting interface:

$$E = E_0 e^{-\gamma r} \tag{35}$$

where $\gamma = 2\pi n_c[\sin^2\theta - (n_{pp}/n_c)^2]^{1/2}/\lambda$.

This nonpropagating electromagnetic field, called an evanescent wave, decays exponentially with distance from the surface, see Figure 14. The standing cosine wave must satisfy the boundary conditions for the homogeneous reflecting interface [59]:

$$\overline{E}_{t_{pp}} = \overline{E}_{t_c} \qquad \overline{D}_{n_{pp}} = \overline{D}_{n_c}. \tag{36}$$

Thus the standing wave joins smoothly onto the evanescent wave in the rare medium for the tangential components E_x and E_y. For the normal component E_r there is a discontinuity because of the requirement $D = \varepsilon_0 \varepsilon E$, which means that the electric field amplitude in the rare medium
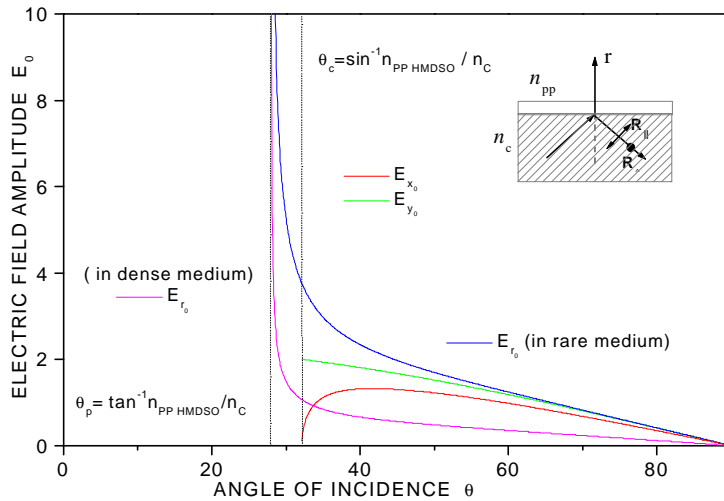

Figure 15. Incidence angle dependence of the amplitudes of electric field components for unit incident amplitude at the totally reflecting interface Chalcogenide glass/ HMDSO plasma polymer.

is magnified by $\varepsilon_c/\varepsilon_{pp}$. For unit incoming amplitude of $\perp$- and $\parallel$-polarized modes the electric field amplitudes at the interface in the rare medium are given by the following expressions [39, 58]:

$$E_{y0} = \frac{2\cos\theta}{[1 - (n_{pp}/n_c)^2]^{1/2}}, \tag{37}$$

$$E_{x0} = 2\frac{[\sin^2\theta - (n_{pp}/n_c)^2]^{1/2}}{[1 - (n_{pp}/n_c)^2]^{1/2}\left([1 + (n_{pp}/n_c)^2]\sin^2\theta - (n_{pp}/n_c)^2\right)^{1/2}}, \tag{38}$$

and

$$E_{r0} = \frac{2\sin\theta\cos\theta}{[1 - (n_{pp}/n_c)^2]^{1/2}\left([1 + (n_{pp}/n_c)^2]\sin^2\theta - (n_{pp}/n_c)^2\right)^{1/2}} \tag{39}$$

The variation of the electric fields with the angle of incidence is shown in Figure 15. E_{y0} represents the electric field amplitude for $\perp$-polarization. The $\parallel$-polarized mode is defined by both E_{x0} and E_{r0} components. The electric field components are calculated for unit incident amplitude in the system chalcogenide glass (As-Se-Te, $n_c = 2.81$)/ HMDSO plasma polymer ($n_{pp} \approx 1.5$).

The evanescent wave decays without energy dissipation, i.e. there is no net flow energy from the dense medium into the non-absorbing medium, the flux density inside the dense medium is given by the time average axial component of the Pointing's vector $\overline{S}_x = \frac{1}{2}Re\{\frac{c}{4\pi}[\mathbf{EH^*}]\}$, which is zero. In case of the absorbing rare medium the energy of the reflected wave is extracted and absorbed in the near interface region. Thus, the attenuated total reflection occurs.

This region, where the absorption occurs, is defined by the depth of penetration, d_p, of the evanescent wave into the rare medium: $d_p = 1/\gamma$. Note, that both values d_p and γ are independent of polarization. Thus, the depth of penetration is one of the values that determines the ATR spectrum. The wavelength dependence upon the penetration depth causes the distortion of the ATR spectrum comparing to the transmission spectrum. The increase of the penetration depth with the wavelength results in the more intense absorption bands in the ATR spectrum. The correlation between the reflection and transmission spectra is described by so called effective thickness, d_e, which defines the thickness of the film of the same material which would give the same absorption for transmission at normal incidence as the corresponding ATR spectrum. Here, one should distinguish between two cases: the analysed sample is a bulk material, $d \gg d_p$, or a thin film, $d_p \ll d$.

In case of a bulk medium the actual sampling depth, d_s, is defined by the full absorption of the evanescent wave and results in the value of about $3d_p$ [60]. The spectral information is averaged along the fibre length. Moreover, the absorption is composed of decreasing contributions from deeper layers of the analysed medium. The effective thickness for the bulk material is expressed in the following way in case of the low absorption approximation [39]:

$$d_e = \frac{E_0^2 d_p n_{pp}/n_c}{2\cos\theta} \tag{40}$$

In general, the ATR spectrum is determined by the coupling of the evanescent wave to the absorbing rare medium. As it is seen from (32-34), this coupling is influenced by the following factors: electric field strength, depth of penetration, sampling area, index matching. The strength of coupling increases with decreasing θ. The spectra appear normal, as the angle of incidence approaches the

critical angle from higher values. Moreover, the signal-to-noise ratio, S/N, increases because of the increase of the penetration depth d_p and the electric field intensity of the standing wave E_0. The reducing of the sampling area has a negligible influence in the net effect. When the critical angle is reached and crossed, the spectra become more and more distorted which was experimentally shown by Mirabella [60].

Another case of interest is that of thin films. The electric field can be considered constant over the film thickness d. The effective thickness d_e is given by [39]:

$$d_e = \frac{E_0^2 \, d n_{pp}/n_c}{\cos \theta} \tag{41}$$

For different polarization modes the effective thicknesses are:

$$d_{e\perp} = \frac{4 d n_{pp} \cos \theta}{n_c - 1/n_c} \tag{42}$$

$$d_{e\parallel} = \frac{4 d n_{pp} \cos \theta}{n_c - 1/n_c} \frac{(1 + n_{pp}^{-4}) \sin^2 \theta - n_c^{-2}}{(1 + n_c^{-2}) \sin^2 \theta - n_c^{-2}} \tag{43}$$

From (41) it follows that the effective thickness for thin films is controlled by the same factors ensued from (40) except for penetration depth. The effective thickness is proportional to the actual film thickness d. The important consequencies of this consist in the following:

— there is no ATR spectrum distortion caused by the wavelength dependence;
— the effective thickness becomes a finite value as the angle of incidence reaches the critical angle;
— the spectra are not distorted for measurements done near the critical angle.

In case of thin films the critical angle for measurements is determined by n_{gp}/n_c and not by n_{pp}/n_c where n_{gp} is the refractive index of the medium surrounding the fibre with a thin film, e.g. the gaseous stable products of plasma-chemical conversion in a process vessel. There is no discontinuity in the effective thickness when the angle of incidence crosses θ_c defined by (25).

Due to absorbing thin film the evanescent wave loses some of its power what in turn leads to a power loss from the propagating radiation. The power attenuation coefficient γ_f of a ray can be found either by summing the loss at the reflection points in unit length of the fibre or by averaging the power transmission coefficient over the ray half-period between successive reflections.

According Snider and Love [56] the absorption per unit length of the fibre γ_f is related to the absorption coefficient of the film material α_{pp} ($\alpha_{pp} = 4\pi k_{pp}/\lambda$, $\widehat{n}_{pp} = n_{pp} + i k_{pp}$) in such a way:

$$\gamma_f = \frac{\alpha_{pp}}{V} \left(\frac{\theta}{\theta_c}\right)^2 \frac{1}{[1 - (\theta/\theta_c)^2 \sin^2 \theta_\phi]^{1/2}} \tag{44}$$

where V is the fibre parameter.

The attenuation is a maximum when the ray is meridional, i.e. $\theta_\phi = \frac{\pi}{2}$, and decreases with increasing skewness.

Analysis of the expression (44) lets to mark out the parameters which influence the sensitivity of the method. The functional dependence of γ_f can be rewritten in the following form:

$$\gamma_f = f_1(1/\rho, 1/n_c) \, f_2 \qquad (45)$$

where f_2 represents the functional dependence on the illumination of the fibre cross-section, in other words on angles of incidence.

The fibre properties as well as the parameters of the measurement could have a twofold influence on the sensitivity of the method. The use of tiny fibres with small ρ allows one to enhance the power attenuation. Moreover, as it follows from (30) lower values of the fibre diameter results in higher number of reflections. At the same time the sampling area becomes smaller. It seems difficult to estimate correctly the change of the sampling area as a result of the ρ decrease. Note, that ρ can not be chosen arbitrary small: the criteria $\rho \gg \lambda$ must be fulfilled.

Lower values of the refraction index of the fibre core lead to lower values of the angle of incidence θ at the fixed illumination conditions. This results in the increase of the number of reflections. Note, the value of n_c must be high enough that the total reflection on the interface "fibre/film" occurs.

The launch conditions determine the angle of incidence θ, the angle distribution of the electric field of propagating radiation. The endface of the fibre should be illuminated by collimated beam.

4.2   Infrared transmitting fibres

The crucial point of the method is the internal reflection element — the optical fibre here. At the current moment a set of infrared fibres are available for the infrared spectroscopy. The progress done in the development of IR fibres in the last few years was induced mainly by remote sensor applications and power delivery applications [61 − 65]. The IR fibres can be divided into three large groups: glass fibres, crystal fibres and hollow waveguides, see Table 5.

The detailed information on the materials utilized for the fabrication technology of IR fibres can be found in recent publications, e.g. [66 − 69]. At the moment there are three classes of the fibres which are transparent in the mid-IR spectral region: chalcogenide fibres, halide fibres and hollow fibres, e.g. see [66]. For reasons discussed later chalcogenide fibres were chosen for the infrared evanescent wave spectroscopy. That is why the main attention will be devoted to this kind of the waveguides. Chalcogenide glasses are formed on the basis of some elements belonging to groups 4B and 5B in the periodic table. Chalcogenide glasses are classified usually into three groups: sulfide, selenide, and telluride [70]. Depending on the composition chalcogenides exhibit various physical properties which have been widely reported [70 − 75].

IR transmission characteristics are influenced strongly by structural imperfections and impurities. The common impurities contained in chalcogenides are oxygen, hydrogen and water. The assignment of the impurity absorption bands are summarized in Table 6. Here is presented the information on the impurities forming R-O, R-O bonds (R= As, Te, Se).

Glass	Heavy metal fluoride (HMFG)	ZBLAN (ZrF$_4$-BaF$_2$-LaF$_3$-AlF$_3$-NaF)
	Germanate	GeO$_2$-PbO
	Silica-based glasses	SiO$_2$-dopant
	Chalcogenide	As$_2$S$_3$, AsTeSe, AsGeTeSe
Crystal	Polycrystalline (PC)	Thallium halides, alkali halides, silver halides
	Single crystal (SC)	Sapphire
Hollow waveguide	Metal/dielectric	Hollow glass waveguide
	Refractive index <1	Hollow sapphire, BeO, SiC guides at $10.6\mu m$

Table 5. Classification of IR fibres on the fibre material and structure with common examples (adapted from [65]).

Assignment	Wavenumber, cm^{-1}	Glass System	Reference
AsO–H, stretching	925	As–S	75
overtone	1825		75
Se–O	965	As$_2$–S$_3$	76
SeO–H	3420	As–Se, Ge–As–Se	72, 76
	2190	As–Se	72, 76
combination Se-H stretch + AsSe$_3$ stretch	2410	Ge–As–Se	75
Se–H	2430	As–Se	76
combination Se-H stretch + AsSe–H stretch	2815	Ge–As–Se	75
	2830	As–Se	76
H$_2$O	1585		76
	1580		75
	3610	As–S	75
OH	3520	As–Se	76
	3600		76

Table 6. Impurity absorption bands in chalcogenide glasses.

4.3   Experimental realization of method

The application of the evanescent wave spectroscopy for *in situ* analysis of the films growth in the plasma of gas discharge sets some special requirements on the fibre material. One can point out three types of them. The first one is originated from the spectroscopy technique and concerns the following issues: required transmittance spectral region, low absorption of step-graded core, refractive index of the core material, etc. The characteristic absorption bands of the moleculare structures in question lie mainly in the mid-infrared spectral region. The graded-profile fibres are not suitable for the evanescent wave spectroscopy: evanescent wave amplitude decreases considerably between the turning point and the reflection interface, therefore for the rays in the graded-profile fibres the fraction of power lost to the growing plasma polymer is much smaller than for rays in the step-graded fibres. The modern technology allows one to produce very fine fibres – up to 100 μm. Note,

that the smallest diameter is limited by the diffraction effect, i.e. the fibre should be a multimode waveguide with parameter $V \gg 1$ and comparatively large diameter $\rho \gg \lambda$.

The other requirements concern the stability of the fibre core against the effect of the plasma. The core material must be stable against UV radiation from plasma. High thermal loading during the plasma processing time requires high values of glass transition temperature, stability of the optical properties under the thermal effect. Moreover the fibre core should be chemical and mechanical resistant to ion bombardment.

The safety and the commercial aspects are of much importance also:
— the exposure of the fibre to the plasma should not lead to the formation of toxical compounds;
— the fibres of interest should be available on the market for acceptable prices.

At the moment there is a limited set of the commercially available infrared fibres which meet the main requirements mentioned above. The chalcogenide (As-Se-Te) fibres produced by Amorphous Materials Co. (USA) with various core diameter ($250\mu m$ and $750\mu m$) were used in the experiments described in this work. Step-graded fibres can be purchased without cladding, only with polymer coating which protects the core. The characteristic transmission spectrum of the fibre with diameter of $750 \ \mu m$ is shown in Figure 16. The characteristic absorption lines are due to impurities described above. It seems impossible to separate correctly the absorption bands originated from the water and/or hydroxyl group containing in the spectrometer and absorbed on the active part of the core from those bands appeared due to these impurities formed in the chalcogenide glass already at the stage of the fibre fabrication. The absorption bands at the $2400 - 2250 \ cm^{-1}$ wavenumbers are caused by vibrations of CO_2 molecules presented in the spectrometer and the fibre couplings. The chalcogenide glass has the refractive index n_c of 2.82 at the $4\mu m$.

These fibres are chemically and mechanically durable, stable to UV radiation (in the contrary to silver halides fibres). They possess relatively low optical losses, 1 dB/m from 2 to 10 μm in comparison with PC and SC fibres.

The numerical aperture varies from $0.5 - 0.6$ ($\pm \ 35 - 40°$) up to $0.6 - 0.7$ ($\pm 40 - 50°$) [78]. Thus, the fibre parameter V is equal to 112 at $7\mu m$ wavelength for the chalcogenide fibre ($n_c = 2.81$) with $250\mu m$ core diameter. The drawback of these fibres in regard to diagnostics of plasma processed films is their low glass transition temperature $Tg = 136^0C$. However, one should point out a relatively low value of thermal expansion coefficient, $23.5 \times 10^{-6}/°C$, and good thermal stability of the index of refraction, $3 \times 10^{-5}/°C$. Such parameters assure the stable transmission characteristics of the chalcogenide fibres after a exposure to a discharge plasma. Moreover, the performed computer simulation [79] showed that an estimated thinning of the fibre in plasma results in the increase of the detected absorption from 0.3% (at 700 cm^{-1}) up to 5% (at 3200 cm^{-1}).

A totally cladding- and coating-free part of the fibre serves as the internal reflection element. The protecting polymer coating can be removed from the core glass by chloroform (99%, Merck KGaA, Germany). Developed technique consists in the successive drop by drop solution of the appropriate region of the polymer film in the fresh portion of the solvent along the required length of the fibre. A thin residual film of the protecting polymer is removed from the dryed fibre core by etching in the O_2-plasma.
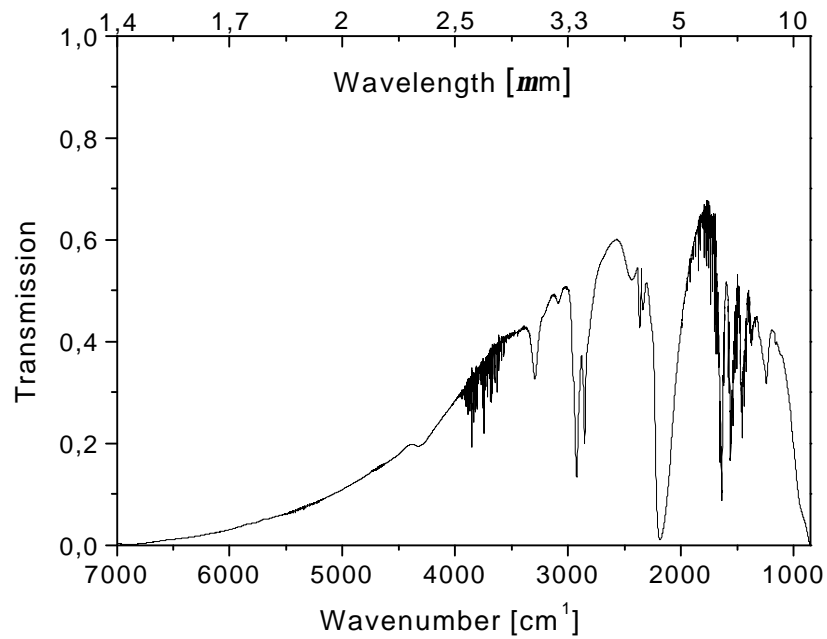
Figure 16. The measured transmission spectrum of chalcogenide (As-Se-Te) fibre with protecting coating from polyamide.
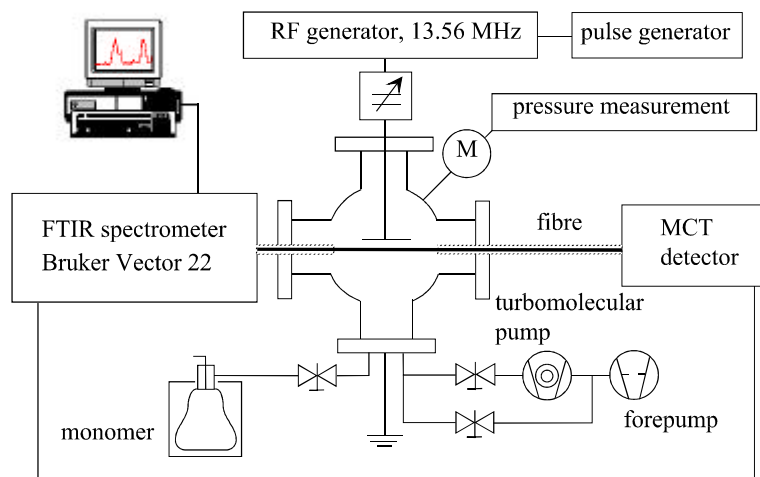
Figure 17. Typical experimental arrangement for in situ IR evanescent wave spectroscopy on plasma polymerization.

The prepared fibre was arranged directly from the Vector 22 IR spectrometer (Bruker, Germany) through the vacuum chamber to the external MCT-detector. The bare part of the fibre is exposed to the gas discharge plasma of organic vapour. The distance between the fibre core and the powered electrode, which is capacitively coupled to rf (13.56 MHz) generator, can be varied. The fibre is typically situated in the plasma bulk and, hence, is under the floating potential. The variation of the distance between the fibre core and the electrode allows a space-resolved study of the structure formation in the axial direction. Infrared evanescent wave absorption spectra can be taken after every plasma pulse or a set of the pulses in dependence upon the deposition rate. After the accumulation series the fibre must be exposed in etching plasma in order to regenerate the active part of the fibre. Note, that it is also possible to investigate the etching of the deposited plasma polymer film at the regeneration stage accumulating the absorption spectra in the same way. The experimental arrangement for evanescent wave spectroscopy is shown in Figure 17.

4.4   Modification of method

The number of reflections per unit of fibre and the length of the active part of the fibre used as IRE are the factors determining the sensitivity of the evanescent wave spectroscopy. There are two simple ways to increase considerably the number of reflections. The use of very fine fibres up to 100 μm, however with $\rho \gg \lambda$. The other way assumes the thinning of the active part of relatively thick fibre. In the last case the launch conditions for the transmitted beam in the tapered part of the fibre define the number of reflections as well as the propagation of the radiation. These launch conditions are determined not only by the illumination of the fibre endface, but also by the taper shape, its length and the geometric parameters of the tapered part of the fibre.

There are various theoretical models developed for theoretical analysis of the radiation propagation in the tapered fibre [80 − 83]. The influence of launch conditions on the number of total reflections, average effective thickness and output radiation intensity was simulated by means of geometric optics [79]. Besides, the simulation provides the information on the optimal thinning of the fibre in order to get a maximal magnification of detected absorption. The following simplifications were accepted: the meridional rays of IR non-polarized radiation propagate through the fibre of a perfect geometry without any absorption caused by cladding or core glass. The simulation was carried out with the following parameters:

- fibre diameter 750 μm; fibre length 80 mm;
- refractive index of the fibre core, 2.82;
- refractive index of the environment (HMDSO), 1.38;
- radiation wavelength, 4 μm;

The influence of the tapered shape is well illustrated in Figure 18 where the dependence of average effective thickness on the angle of incidence, α, is shown for various shapes of the fibre tapering. Simulation shows that the maximum of the number of total reflections is achieved at the fibre thinning when the diameter ratio, d_o/d_{thin}, is about of the factor 3, see Figure 19. Moreover, further thinning of the fibre does not influence remarkably on magnification of absorption, see Figure 20.
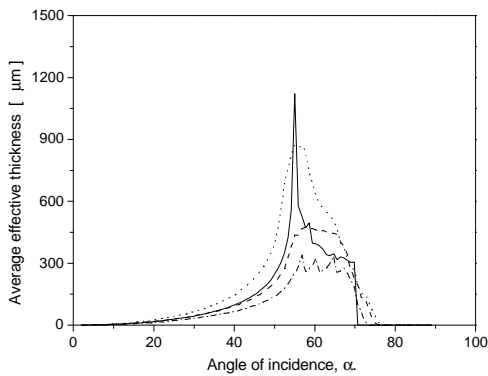
Figure 18. Influence of the tapering profile on the dependence of average effective thickness on the angle of incidence α. The fibre thinning from 750 μm to 250 μm, length of the taperd part 8 cm. Profiles: solid line - polynomial profile, dot line - parabolic, dash-dot line - linear, dash line - exponential.
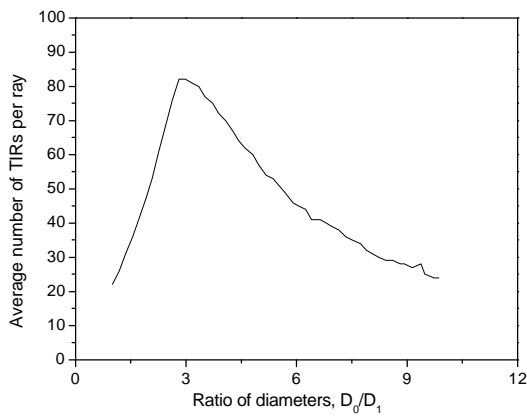

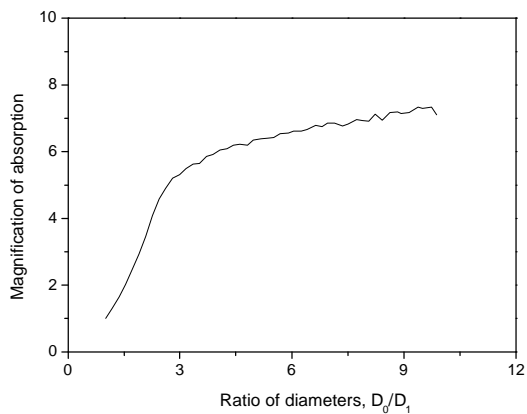Figure 19. Influence of the fibre thinning on average effective thickness.

Figure 20. Influence of the fibre thinning on the magnification of absorption. HWHM of the distribution function of the incidence angle α 30°, medium absorption $1.5 \times 10^4 m^{-1}$.
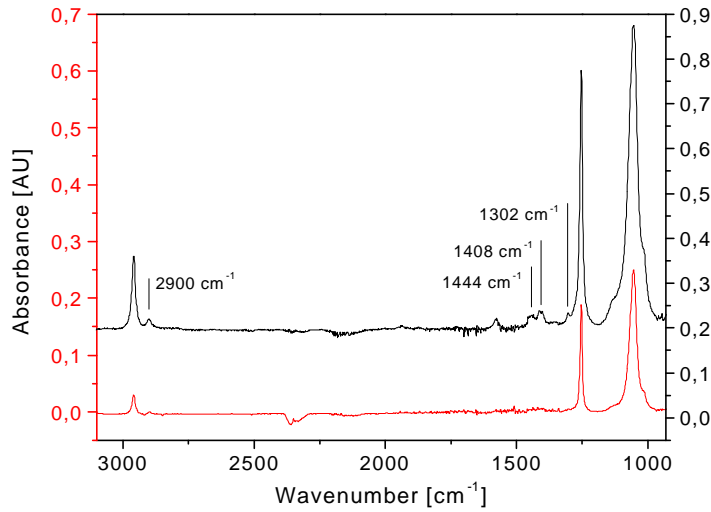
Figure 21. Comparison of the IR absorption spectra of liqiud HMDSO monomer obtained
by means of normal and tapered fibres. Right Y-axis is for the spectrum from
the tapered fibre, left Y-axis is for the spectrum from the normal fibre.

The potentials of the fibre thinning for the enhancement of sensitivity is illustrated by the comparison of IR absorption spectra obtained by means of both normal (red curve) and bi-tapered fibres (black curve), see Figure 21.

The spectrum from liquid HMDSO monomer was taken with chalcogenide (As-Se-Te) glass fibre with $\rho = 750\mu m$. The length of the active part of the fibre was 83 mm. A part of the analogous fibre was heated up to the softening point and then pulled in order to get very fine bi-tapered active part with the diameter of 300 μm and the length of 83 mm, h.e. equal to that of the normal fibre. The ratio of the reflection numbers is $N_{tapered\,fibre}/N_{normal\,fibre} \approx 2.5$. One should note unequal increase of the absorbance for the different bands:

$I_{tapered}/I_{normal}\ (1050\ cm^{-1}) = 2.7;$
$I_{tapered}/I_{normal}\ (1250\ cm^{-1}) = 3.1;$
$I_{tapered}/I_{normal}\ (2960\ cm^{-1}) = 4.7.$

The spectra presented in Figure 21 were obtained from a half-continuous medium — monomer liquid. As it was mentioned above, the effective thickness, i.e. the resulted spectrum, depends on the wavelength in the case of the bulk sample. This causes the observed irregularity in the absorbance ratios at the different wavenumbers.

Plasma polymerization of styrene in low pressure rf discharge

Plasma polymerization of aromatic compounds, in particular styrene, has been very intensively studied for many years [1, 84 − 91]. The wide range of gaseous products were detected in styrene discharge by means of mass spectrometry, optical emission spectroscopy: from molecular hydrogen up to high-molecular compounds [1, 87, 91 − 93]. The surface analysis of plasma polymerized styrene (PPS) allowed one to study the correlations between process conditions and the composition of the deposited films [1, 85 − 88]. Though the great quantity of the experimental data, the comprehensive mechanism of the film formation has not yet completely understood. Nevertheless, the known experimental results allow one to control the structure and the composition of PPS in a necessary way by the choice of appropriate process parameters. Thus, styrene plasma polymerization represents a good exemplary process for the study of the novel FTIR diagnostic technique.

The aim of the work summarized in this chapter consists in the experimental study of the application and the potentials of the IR evanescent wave spectroscopy for *in situ* diagnostics of thin organic film deposition in gas discharge plasma. Besides this, the investigation of the structure formation at the styrene plasma polymerization was in the scope of this work also. The accent was done at the initial steps of the film growth.

5.1   Deposition of plasma polymerized styrene films

5.1.1   Experimental details

The experimental arrangement for *in situ* evanescent wave spectroscopy on plasma polymerization of styrene is shown schematically in Figure 17. The plasma polymerization process was carried out in the stainless steel vacuum chamber with the volume of about $3l$, where a capacitive rf discharge was maintained between the powered electrode and the grounded wall (the characteristic distance between them is about of $8\ cm$). The powered electrode was coupled to a rf generator $(13.56\text{MHz}, 500W)$ by a fully tuneable π-type matching network.

The styrene (99%, Sigma-Aldrich Chemical Co., Germany) monomer was evaporated and then

introduced into the reactor vessel. The monomer reservoir was protected against exposure to light by enclosing it in aluminium foil which prevents the chemical polymerization of the monomer. Some physical and chemical properties of styrene monomer and chemically prepared polystyrene are summarized in Appendix B. The fibre was placed at the distance of about 22 mm from the driven electrode, i.e. under the floating potential. The deposition rate as well as the film thickness of the plasma polymer films were derived from measurements by spectroscopic ($300 - 800nm$) ellipsometry using Si wafers as a substrate material. Ordinary and gold coated Si wafers (1×2 cm) were placed at the distance of about 1 cm near to the fibre in the plasma bulk. A two-layer optical model was used for calculation of optical constants from ellipsometrical data: plasma polymer on the bulk gold material. Sellmeier and Couchy optical models allowed one to obtain the dispersion relations of the refractive index and the extinction coefficient. The samples with gold coated substrate were also used for film characterization by IR reflection absorption spectroscopy (IRRAS). The evolution of the molecular structure of the growing film was studied by means of evanescent wave FTIR spectroscopy based on the mid-IR transparent chalcogenide fibre (As-Se-Te glass, $250\mu m$ core diameter, Amorphous Materials Co., USA).

The spectral resolution was 2 cm^{-1}. All measurements presented in this chapter were performed with a Norton-Beer weak apodization function and a Mertz phase correction.

The plasma polymerization of styrene was carried out in a pulsed discharge because of the following reasons:

— the appropriate degree of monomer molecule fragmentation can be specified by means of different plasma-on times and thereby it is possible to investigate every process phase, from discharge ignition up to full fragmentation of monomer molecules in the closed reactor or steady state in the reactor with monomer vapour flow.

— plasma polymerization in a pulsed discharge allows one to synthesize thin films with more monomer functional structures, e.g. phenyl rings of aromatic compounds [1, 88 − 90].

— The fibre core material is effected by considerably less thermal loading in the pulsed discharge than in the continuous discharge. Moreover, the variation of plasma pulse duration allows to compensate non-sufficient time resolution of the used IR spectrometer.

The process chamber was pumped up to background pressure (< 0.01 Pa) and the fresh portion of the monomer was introduced every time before the plasma ignition for the fixed pulse duration, τ_{plasma}. Then a discharge was ignited in the closed chamber under the conditions fixed in the accumulation series. Infrared evanescent wave absorption spectra were taken after every plasma pulse or a set of the pulses, depending on the deposition rate. After the accumulation series in the styrene plasma the fibre was exposed to an oxygen plasma (50Pa, $200\ W$), whereby the active part of the fibre was regenerated. The pressure in the chamber was regulated by manual valve adjustment at a fixed pumping speed. During the etching the absorption spectra were accumulated in the same manner. The spectra analysis provides information on the changes of the molecular structure as a result of the exposure of the deposited film to the oxygen plasma.

5.1.2   Styrene plasma and polymerization mechanism

The mass spectrometric analysis of the styrene plasma of rf discharge [85, 91 − 93] showed the significant fragmentation of the monomer molecules into the wide range of the products: C_8H_8 (104 *amu*), C_8H_7 (103 *amu*), C_8H_6 (102 *amu*), C_6H_6 (78 *amu*), C_6H_5 (7 *amu*), C_5H_3 (63 *amu*), C_4H_4 (52 *amu*),C_4H_3 (51 *amu*), C_4H_2 (50 *amu*), C_3H_5 (41 *amu*), C_3H_3 (39 *amu*), C_3H_2 (38 *amu*), C_2H_5 (29 *amu*), C_2H_4 (28 *amu*), C_2H_3 (27 *amu*), C_2H_2 (26 *amu*), CH_2 (14 *amu*), CH (13 *amu*), C (12 *amu*), H_2 (2 *amu*). Radicals and ions do not form the oligomers of styrene in the gas phase. Hence, the gas-surface reactions and dissociative processes prevail for the high molecular species, comparing to the ion-molecule or molecule-molecule reactions in the gas phase.

The increase of the energy input results in the stronger dissociation of the high molecular aromatic compounds (C_8H_8, C_8H_7, C_8H_6, C_6H_6, C_6H_5) and considerable yield of the low molecular species. Decomposition of styrene molecules in the plasma results in the formation of unsaturated hydrocarbons: ethylene [93], acetylene [92]. As a result of dissociation and dissociative ionization processes active species are formed from the unsaturated hydrocarbons. These active species also serve as the precursors of the growing film.

The residual gas, composed of N_2, O_2, etc, can influence the film composition. Even at a small content of the residual gas in a vacuum system, oxygen was found in the plasma polymerized styrene film by XPS [92].

Examination of the experimental data available at the current moment indicates that there is no complete understanding of the polymerization mechanism. The knowledge of the internal plasma parameters (T_e, n_e, EEDF, etc) and the rates of the reaction channels would clarify which mechanism is realized at the chosen process conditions. Despite the general opinion on the mechanism of the styrene plasma polymerization assuming a chain radical mechanism [1, 86, 87, 94 − 96], there are experimentally observed evidences supported the assumption of an ionic mechanism [85].

5.2   Molecular structure of plasma polymerized styrene films

5.2.1   Influence of energy input on structure

The effective energy delivered into the system can be controlled by discharge power, by plasma pulse format (plasma-on time, plasma pulse frequency) at the other fixed process parameters. As it is well known, the enhancement of discharge power leads to the strong fragmentation of monomer molecules in the plasma due to dissociation and dissociative ionization processes [1, 87, 91].

At the high energy input the most of phenyl rings are opened and converted into aliphatic structures which become precursors for the growing plasma polymer. The initiation reactions in the plasma can go through the detachment of hydrogen atoms, break of π-bonds in the phenyl ring or double bond in the vinyl groups. Thus, the characteristic absorption bands of aromatic compounds

are not observed in the IR spectrum. The same effect is realized by the increasing of the plasma pulse frequency [88]. Here, the plasma pulse duration was chosen as the parameter of the variation of the effective energy input into the system. One should expect the mentioned trend in the molecular structure of deposited polymer at the increasing plasma pulse duration, i.e. the formation of aliphatic a-C:H films at the longer plasma pulses.

For the used plasma reactor it was found optimal plasma pulse duration τ_{plasma} $3 - 10$ s at the chosen energy input. Very short plasma pulses do not provide sufficiently high deposition rate. Long plasma pulses in the closed reactor result in the break-up of the considerable amount of the monomer functional groups, see Figure 22. The plasma polymer deposition at the pulse time of $10s$, see curve II on Figure 22, results in the complete destroying of the aromatic functional groups. This is reflected in the vanishing absorption bands from phenyl rings which are present in the plasma polymer obtained in the regime of 5 s plasma pulse. The bands in the region $3080 - 3010 cm^{-1}$ are caused by aromatic C-H stretching vibrations: at the 3083 cm^{-1}, 3058 cm^{-1} and $3025 cm^{-1}$ wavenumbers. Absorption bands in the region $1450 - 1490$ cm^{-1} are caused by ring semicircle stretch vibrations: strong lines at 1495 cm^{-1} and $1452 cm^{-1}$. The latter vibrations are mixed, sometimes strongly, with in-plane C-H bending vibrations [97, 98]. The absorption line at the $1600 cm^{-1}$ is due to quadrant stretching vibrations of C-C in the phenyl ring.
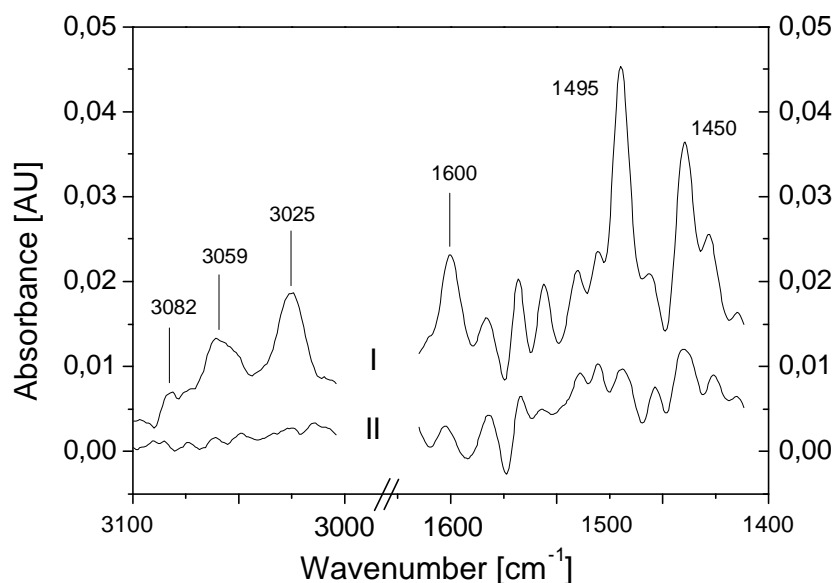

Figure 22. Infrared absorption spectra:
        (I) weak fragmentation of phenyl rings (process conditions: 20 Pa, 60 W, τ_{plasma} 5 s),
        (II) strong fragmentation of phenyl rings (process conditions: 20 Pa, 60 W, τ_{plasma} 10 s).

5.2.2   Formation of molecular structure

The IR spectra of chemically prepared polystyrene [4, 97 − 101] shows that absorption intensities of the bands from both spectral regions are more or less equal. IRRAS spectrum of polystyrene film prepared by dip coating [4, 102] on the gold coated Si wafer and evanescent wave absorption spectrum of plasma polymerized styrene film are shown in Figure 23. The molecular structure of plasma polymerized films, distinct from that one of chemically prepared polystyrene, not only represents other molecular configuration, but also induces specific intermolecular interactions (dipolar forces, hydrogen bonding, etc). Both factors are responsible for the differences in the peak intensities and positions as well as lineshapes. In plasma polymerized thin films the aromatic C-H stretching oscillations are hampered because of high cross-linked molecular structure. This is the reason for the considerable difference between peaks intensities of the stretching and bending vibrations bands. Moreover, the absorption line due to deformation aromatic C-H vibrations can be detected earlier than that one from stretching oscillations of the same molecular group, see Figure 23, what is also explained by the cross-linking. The stretching frequency of double bond C=C in styrene molecule (C_6H_5CH=CH_2) occurs in the region $1637 − 1616$ cm^{-1} in infrared spectra. The cross-linking results in the shift of this band to higher wavenumbers, closer to the C=C stretching frequency of aliphatic compounds, e.g. $1650 − 1638 cm^{-1}$ in vinyl group. Indeed, it is very difficult to distinguish the absorption bands of C=C group conjugated to phenyl ring from those of non-aromatic alkenes. The growth of the aromatic structures is explicitly seen at the shorter plasma pulse duration, here τ_{plasma} 5 s, see Figure 24. The same characteristic absorption bands of phenyl ring are presented on the accumulated spectra.

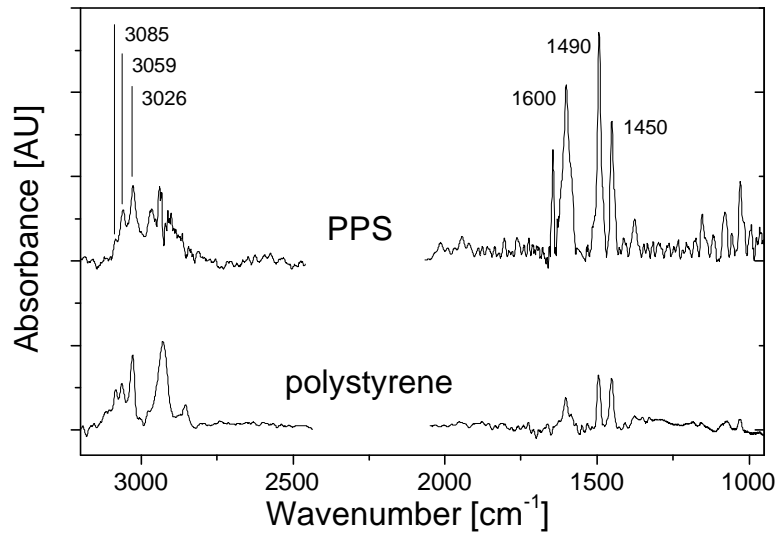

Figure 23. Comparison of IR absorption spectra of chemically prepared polystyrene (IRRAS, 100 nm thick film) and plasma polymerized styrene (IR EWS, 64 nm thick PP film, 10 Pa, 50 W, τ_{plasma} 5 s). The spectrum of PPS is shifted relative to the first one.
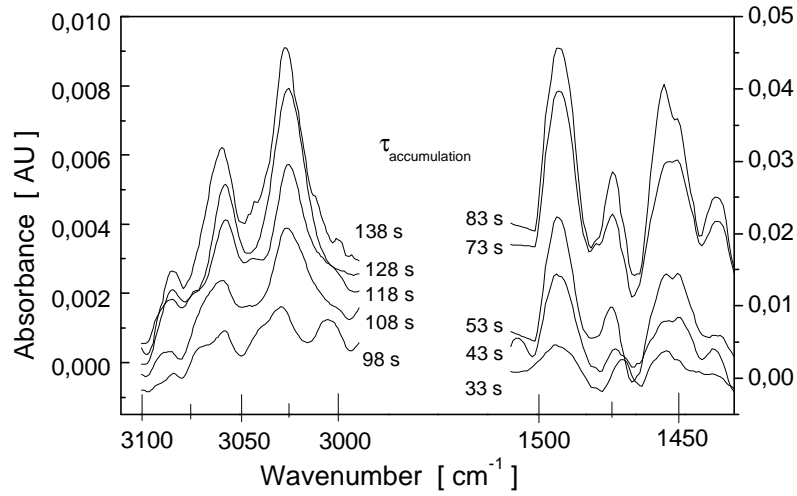
Figure 24. Evolution of infrared absorption spectra of plasma polymerized films with the accumulation time. Absorption bands due to aromatic C-H stretching vibrations lie in the spectral region $3080 - 3010$ cm^{-1}. Absorption bands in the spectral range $1495 - 1450$ cm^{-1} are caused by ring semicircle stretching and in-plane C-H bending vibrations. Deposition conditions: 40 Pa, 100 W, τ_{plasma} 5 s.
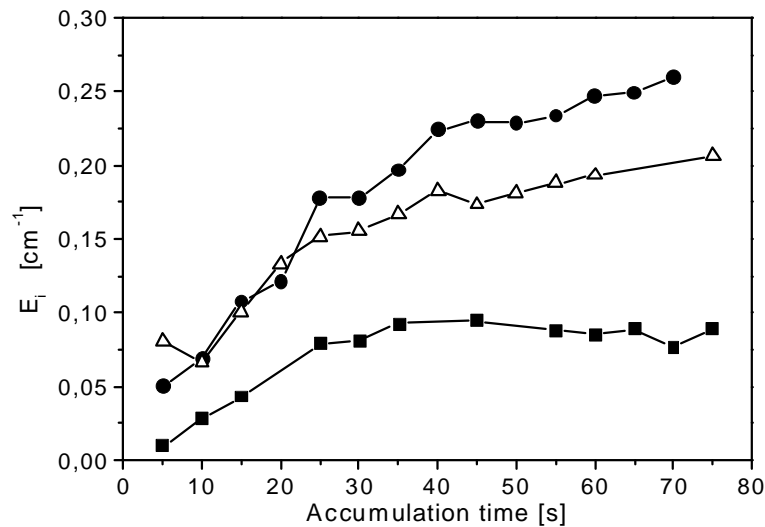

Figure 25. Dependencies of the integrated absorbance on the accumulation time.
■ - aromatic C-H stretching vibration at the 3025 cm^{-1},
△ - quadrant ring C-C stretching vibration at the 1600 cm^{-1},
● in-plane C-H bending vibration at the 1495 cm^{-1}.
Deposition conditions: 10 Pa, 50 W, τ_{plasma} 5 s.

The accumulation time can be interpreted as the thickness of plasma polymer film. The equal process conditions in the series of plasma pulses guaranty the same plasma-chemical conversion of the monomer molecules during every pulse and, hence, the same gas phase composition and the deposition mechanism. Thus, during every plasma pulse we deposit the plasma polymer film of equal thickness and constant composition. But the dependencies of integrated absorbance on the accumulation time show a non-linear alteration of absorption character, see Figure 25. After the accumulation time of about 25 s the integrated absorbance of aromatic C-H stretching vibration band at $3025cm^{-1}$ remains constant. Two bands, at $1495cm^{-1}$ and $1600cm^{-1}$ undergo the change of their development rate. This alteration of absorption behaviour of the plasma polymer film takes place at the thickness of about $5-6nm$. This effect can be explained by existence of interface layer between the fibre core and the bulk plasma polymer. The size of the monomer group in polystyrene can be taken for the estimation of the thickness of plasma polymer monolayer. It is estimated from the molar volume V_m (cm^3mole^{-1}) of polystyrene monomer group, see Appendix B:

$$s \sim \sqrt[1/3]{V_m/N_a} \qquad (46)$$

where N_a is the Avogadro constant, V_m is equal to 99.1 cm^3mole^{-1} [103, 104]. The calculation gives the value $s \simeq 0.6nm$. The inhomogeneous growth of plasma polymer at the deposition beginning goes through activated sites formed on the substrate surface by ions and radicals from plasma. When the thickness reaches the critical value, $5-6$ nm here, plasma polymer builds the closed film on the substrate surface and then the film formation is effected by cross-linking. Aromatic C-H stretching vibrations are hampered. The following deposition leads to the formation of dense, highly cross-linked bulk plasma polymer. The inhomogeneous structure of plasma polymer films was noted by Wrobel et al [105, 106] who studied plasma polymerized organosilicones. However, they did not study the internal, adjacent to the substrate surface, layer of the growing plasma polymer film in detail. According to them the composite structure consists of two regions: dense highly cross-linked bulk layer and top thin ($50nm$) oligomeric layer. The existence of the internal layer was shown by Poll et al for the plasma polymerized hexamethyldisiloxane (HMDSO) films [10]. The interface between substrate and the bulk plasma polymer film was nearly $30nm$ thick. In comparison with the bulk layer this interface had different elemental composition, the molecular structure of thin interface layer was not analyzed.

The thickness of plasma polymer films and the deposition rate were derived from *ex situ* ellipsometrical measurements in the spectral range $300-800nm$. Sellmeier and Cauchy dispersion models were used for the ellipsometrical data processing. Both models yield nearly the same results for film thickness and optical properties of plasma polymerized styrene. The deposition rate was equal to $13nm/min$ at the chosen process conditions: 40 Pa pressure, $100W$ discharge power, τ_{plasma} 5 s. The absorption of stretching aromatic C-H vibrations is always detectable when plasma polymer film, deposited at these conditions, is nearly $21nm$ thick. The signal from deformation aromatic C-H vibrations can be recognized at the nearly $7nm$ thickness of plasma polymer film. The lowest measurable thickness depends on the analysed material. In case of the strong absorber one can get a detectable characteristic absorption bands at the thickness of a few monolayers. The sensitivity of the technique has to be treated in terms of lowest detectable absorbance. The IR evanescent wave spectroscopy with $8cm$ long active part resulted in the absorbance value of nearly $5-9 \times 10^{-4}$ absorbance units for 21 nm thick film or the absorption coefficient of $0.508 - 0.914$ cm^{-1}. IRE plate optical element (9 cm long, maximal reflection number is 34 at 45° incidence angle) showed

a little worse value: $1 - 5 \times 10^{-3}$ absorbance units for 25 nm thick polystyrene film [4].

5.2.3 Formation of domains of various molecular orientations

Irregular, cross-linked amorphous molecular structure is characteristic for plasma polymers. The high variety of monomer units of different kinds accounts for this. Moreover, in contrast to the ordinary chemical polymerization the propagation reactions occur not only at the ends of "growing polymer chain", but at any activated point of the surface of plasma polymer film. The deposition of regular structures by plasma polymerization requires very specific conditions which can provide a set of the processes in the plasma and on the surface. The initial organic compound, in vapour of which the discharge is ignited, has to contain the functional group (aromatic constituent, functional group with inorganic elements etc) which position and orientation on the surface is responsible for the possible regularity. The state of the substrate surface and the ion bombardment determine the distribution of the active centers where initiation and propagation reactions occur. The structure of the first monolayers formed on the substrate surface and then on the plasma polymer surface controls the position of the functional groups: their orientation, surface distribution, etc.

Spectral regions $1100-1000$ cm^{-1} and $950-850$ cm^{-1} are very sensitive to the molecular orientation of phenyl rings relative to backbone chains. Detailed study of both spectral regions provides the comprehensive information on IR spectra of chemically prepared polystyrene films with various tacticity [107]. Possible phenyl ring orientations relative to the backbone chain of a polymer are presented in Figure 26.

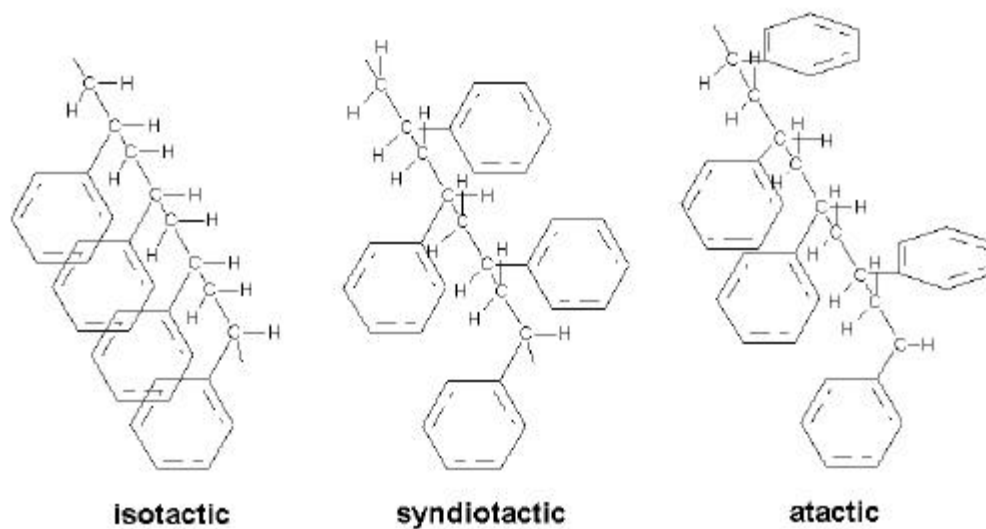**isotactic**   **syndiotactic**   **atactic**

Figure 26. In dependence on the way of phenyl rings arrangement along the backbone chain one differentiates the following tacticities of polystyrene: isotactic, syndiotactic and atactic.

Atactic polystyrene is a disordered material with regard to the phenyl ring orientations relative to the chain. The disordered nature of the atactic polymer prevents polymer chains from regular aligning in crystal structures. Atactic polystyrene is synthesized commonly by free radical vinyl polymerization. Syndiotactic polystyrene has a regular structure: the phenyl rings come on alternating sides of the backbone chain.

Syndiotactic polymer chains can form crystalline structures. Syndiotactic polystyrene can be prepared by metallocene catalysis polymerization. Polystyrene can also possess short-range oriented isotactic structure when the phenyl rings are attached to the backbone chain on the same side. Atactic amorphous polystyrene has the only absorption line in the latter spectral region, at 906 cm^{-1}, corresponding to out-of-plane mode of the phenyl ring. In the isotactic crystalline polymer one observes the splitting in two absorption bands at 898 cm^{-1} (parallel dichroism) and 920 cm^{-1} (perpendicular dichroism).

Plasma polymerized styrene (PPS) film II (deposition conditions: 40 Pa, 100 W, τ_{plasma} 5 s) has a spectrum like an atactic amorphous polystyrene: absorption band at 905 cm^{-1}, see Figure 27. PPS film I (deposition conditions: 10 Pa, 100 W, τ_{plasma} 10 s) has 3 peaks in this region: 923 cm^{-1}, 912 cm^{-1} and 895 cm^{-1}. Two of them appropriate to the bands mentioned above.
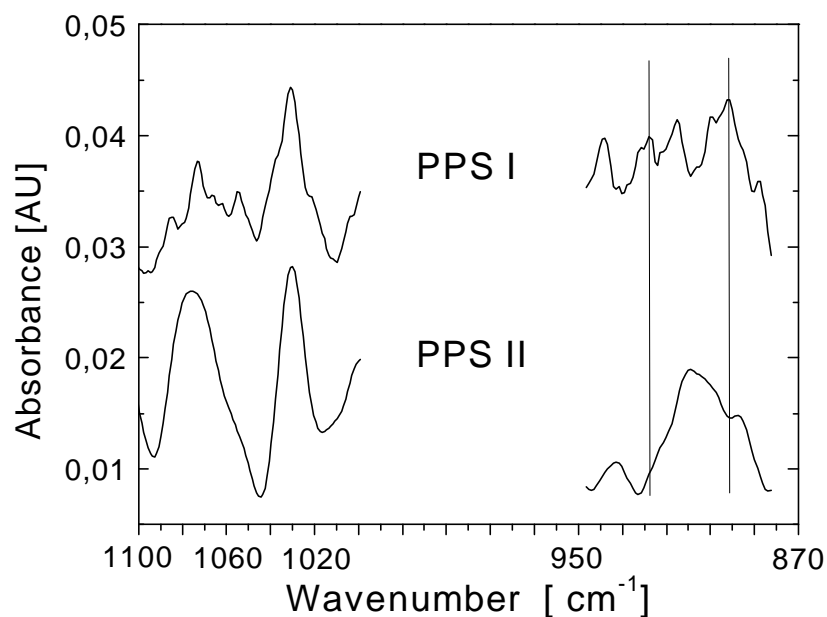

Figure 27. Evanescent wave infrared absorption spectra of plasma polymerized styrene films: frequency expanded scale for spectral regions $1100 - 1000$ cm^{-1} and $950 - 870$ cm^{-1}. Deposition conditions of plasma polymers: (a) PPS I 10 Pa, 100 W, τ_{plasma} 10 s and (b) PPS II 40 Pa, 100 W, τ_{plasma} 5 s.

The absorption band in the middle is a mixture of =CH_2 wagging mode and shifted out-of-plane mode of the phenyl ring characteristic for atactic amorphous polystyrene. The analysis of this spectral range allows to conclude that PPS I film represents a mixture of isotactic crystalline and atactic amorphous structures when PPS II film demonstrates atactic amorphous structure. Atactic polystyrene is characterized by the absorption band at 1069 cm^{-1} in the spectral region of $1100 - 1000$ cm^{-1}. This line is splitted into two bands at 1083 and 1052 cm^{-1}. These two bands consist of a mixture of ring and chain vibrations. Jasse et al [107] observed really four bands in this region 1083 cm^{-1} (perpendicular dichroism), 1075 cm^{-1} (parallel dichroism), 1064 cm^{-1} (parallel), and 1052 cm^{-1} (perpendicular) for isotactic amorphous polystyrene. Thus, one can add to our previous conclusion on the structure of the PPS I film that it contains also isotactic amorphous part. The C-H in-plane bending mode at 1028 cm^{-1} relates to well-defined absorption bands of ring in polystyrene. The intensity of this band is also dependent on the molecular orientation.

5.3 Optical properties of deposited films

Dispersion of the refractive index and the extinction coefficient of plasma polymerized styrene film is shown in Figure 28. The atactic PPS film was obtained at the following process conditions: 10 Pa, 50 W, τ_{plasma} 5 s. Sellmeier and Cauchy dispersion relations provided the same results for two-layer model. Aromatic compounds represent the conjugated polymers. It is known that the magnitude of gap energy, E_g, depends on the π-bonded clusters which have sp^2 coordination [108, 109]. E_g is a function of the quantity of phenyl rings inside a larger cluster and is expressed in the following way:

$$E_g = E_{g0}/\sqrt{N_{ring}} \tag{47}$$

where N_{ring} is the number of phenyl rings inside the larger cluster in a film network, E_{g0} is the gap energy associated with one ring cluster. Robertson et al determined the theoretical value of E_{g0} to be equal to 5.8 eV [109]. Thus, the monomer-like plasma polymer films with high content of the phenyl rings possess smaller gap energy than those with the short-chain aliphatic structure. Moreover, Yi et al [110] found that the deposition of a-C:H films with higher coordination (sp^3) corresponding to the aliphatic molecular structure results in the higher values of the refractive index. Have the gap energy for plasma polymer been determined, so it is possible to calculate the number of rings inside a cluster. The optical band gap E_g of the PPS film was determined from a Tauc plot, see Figure 14. For atactic plasma polymerized styrene film it was found $E_g = 1.4$ eV what results in the $N_{ring} = 16$. Comparison of plasma polymers (this work and [110]) deposited in rf discharge shows other structure-property correlation in addition: with the decrease of aromaticity not only the gap energy increases, but also the index of refraction.

n	1.6	2.1	2.5	2.7
E_g, eV	1.4	1.5	1.7	2.1
N_{ring}	16	15	11	7

Stochiometric ratio [C]/[H] in the phenyl ring is equal to 1.2. The deposition of hydrocarbon plasma polymer with aliphatic structure means the increase of the content of carbon atoms with sp^3 and sp^2 coordinations in the obtained film. The stochiometric ration [C]/[H] for such molecular
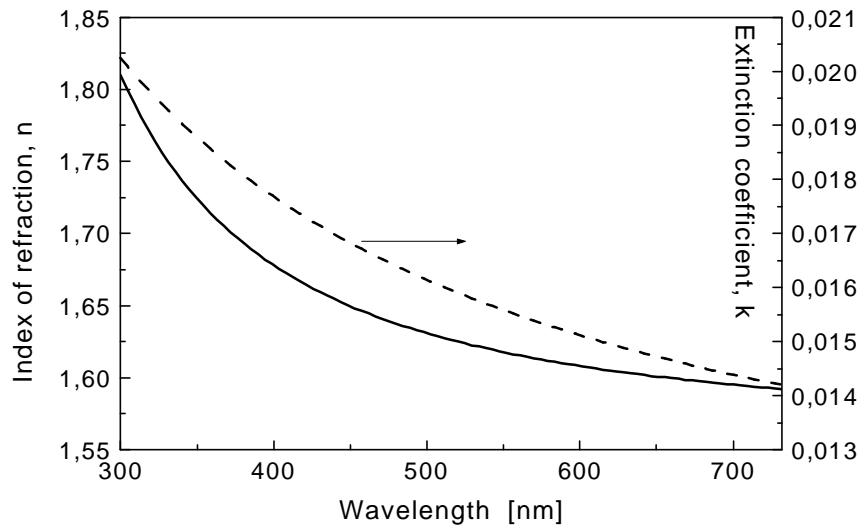
Figure 28. Dispersion of plasma polymerized styrene films of 64 nm thickness.
Deposition conditions: 10 Pa, 50 W, τ_{plasma} 5 s.
The fitting is done with minimal square error of about 2.
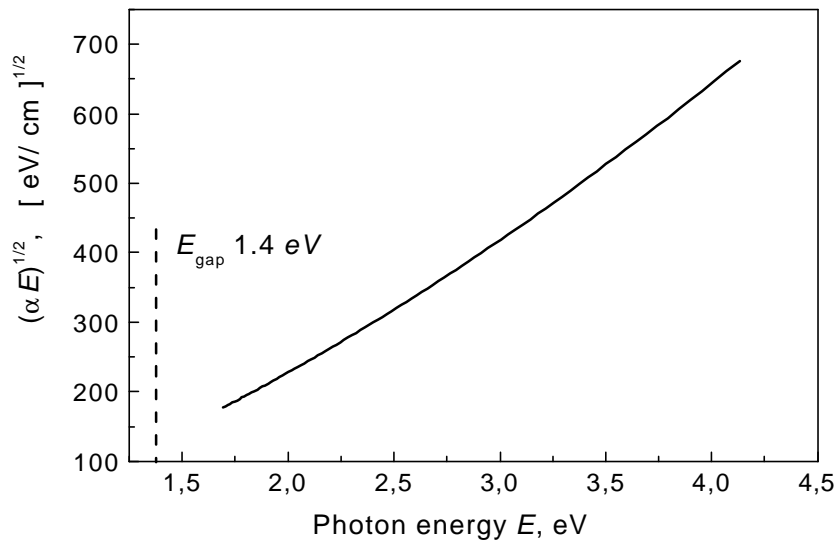

Figure 29. Tauc plot for plasma polymerized styrene film of 64 nm thickness.
Deposition conditions: 10 Pa, 50 W, τ_{plasma} 5 s.

structure is higher than 1.2, i.e. the hydrogen content is enhanced. Thus, it can be concluded that the enhancement of hydrogen content leads also to the increase of the gap energy and the index of refraction. This correlation for the gap energy was confirmed experimentally [111 − 113].

5.4   Fibre regeneration

The active part of the fibre can be regenerated by the oxygen plasma treatment. The etching was carried out in the pulsed regime at the following process conditions: 50 Pa, 200 W, τ_{plasma} 7 s. In order to avoid the overheating of the fibre, the time lag between two subsequent plasma pulses was 30 s. The infrared absorption spectra were accumulated in the same way as at the plasma polymerization. The last absorption spectrum of the accumulation series, taken at the deposition, served as the background spectrum for the following measurements at the etching, i.e. every subsequent spectrum taken at the etching represented the difference spectrum:

    ”spectrum from the rest film”

  −

    ”spectrum from the film grown after the plasma polymerization series”

The characteristic functional groups constituting the plasma polymer are destructed in the oxygen plasma and the deposited film is ablated from the fibre surface, see Figure 30. It can be more clearly seen on the absorption spectrum recorded at the end of etching process, here is about after 1850 s of the etching time. The etching process was continued up to the spectra show no further absorption from the aromatic functional group.
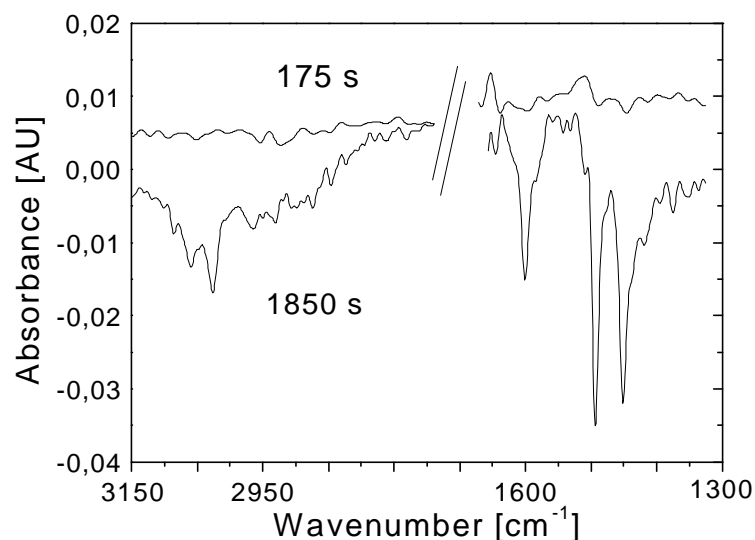

Figure 30. Destruction of functional groups in plasma polymer as a result of the etching in oxygen plasma. Process conditions: 50 Pa, 200 W, τ_{plasma} 7 s. Etching time corresponding to the obtained spectrum is shown near the appropriate curve.

Film deposition in HMDSO plasma of low pressure rf discharge

6.1 State of investigation of HMDSO plasmas

Hexamethyldisiloxane (HMDSO) is one of the most utilized organosilicon compounds used for a thin film deposition in discharge plasma. The variation of the process parameters allows one to obtain either organic $SiO_xC_yH_z$-like films or inorganic SiO_x-like films. Plasma enhanced deposition (plasma polymerization, PECVD, etc) of silicon dioxide films has already found many important applications in industry for manufacturing of optic coatings [10, 11], barrier films for food packaging or gas separating membranes [12 − 14], dielectric coatings [15, 16], and corrosion protection layers [17, 18]. The comprehensive review of the applications of plasma deposited organosilicon films is presented by Wrobel and Wertheimer [19]. Despite of numerous publications devoted to the organosilicon deposition the main aspects of the film deposition have not been clarified: the plasma chemistry, the plasma-substrate interaction, the film formation.

The first problem, which one faces, lies in the plasma diagnostics. The traditional Langmuir probes can be hardly used in plasma of organic compounds. Although there have been developed some modifications of Langmuir probe method for film-forming plasmas of rf discharges [114, 115], it is very difficult to obtain reliable results by the probe technique. Moreover, Langmuir probes do not allow one to identify the molecular structure of any ionic carriers. Schwabedissen et al [116] suggested the plasma oscillation method for the diagnostics of such plasmas. However, this method delivers the electron density only. Electron densities were measured in the $HMDSO/Ar/O_2$ plasma of a 2.45 GHz microwave discharge and were found to be of $3 \times 10^9 - 2 \times 10^{11}\ cm^{-3}$ in dependence on the oxygen partial pressure (discharge power $1.4 \pm 0.2\ W$, total pressure 8 Pa).

The gas phase composition (ions, neutral molecules) has been analysed mainly by mass spectrometry [10, 117 − 125], gas chromotography [105, 106], IR absorption spectroscopy [5, 6, 126, 127] and optical emission spectroscopy [119, 128 − 131].

Hays described the HMDSO decomposition in rf (13.56 MHz) discharge [132]. The obtained mass spectrometric data gave only the qualitative information because the species, extracted from the

plasmas, were not differentiated from those produced within the ion source of mass spectrometer. Furthermore, only fragments of the monomer were analysed. Seefeldt et al carried out the comprehensive study of the HMDSO ionization by electron impact [120]. The authors measured appearance potentials of the fragment ions and suggested the formation mechanisms of some chosen fragment ions. These data were later used by authors in their study of an Ar/HMDSO glow discharge [133]. Relatively high concentrations of ethane and methane were found in the gas phase. Recently Basner et al measured absolute total and partial electron impact ionization cross sections of HMDSO [123]. The investigation of the ion component of the Ar/HMDSO plasma of rf discharge, done by the same authors, revealed that the ion flux density was small to provide relatively high deposition rate and, hence, the film growth must be determined by neutral particles, at least in highly diluted HMDSO-containing plasmas of low pressure rf discharge.

Alexander et al concluded the ions contribute to a film growth in a twofold way [121, 122]:

— ions arriving at the surface will directy take place in the film growth;
— ion bombardment results in the intensive formation of radical centres which can react
  with species from the gas phase.

Due to dissociation in the ion source of mass spectrometer it is very difficult or even impossible to ascertain the initial high molecular neutral product of the HMDSO decomposition in plasma. Hence, the interpretation of some intermediate molecular weight species in the mass spectra of the HMDSO plasmas is very difficult and ambigious. Stable neutral particles of the HMDSO plasma-chemical conversion can be detected by means of gas chromatography. These products can be accumulated in the sample volume and then can be analysed in gas chromatograph or GC/MS apparatus. Thus, it is possible to get the information on the gaseous stable products of the monomer conversion in electric discharge. Among hydrocarbons (up to C_3H_8) various silane and siloxane derivatives were identified in the low pressure rf discharge in HMDSO vapour [134]: di, -tri- and tetramethylsilane, ethyldimethylsilane and ethyltrimethylsilane, tetramethyl- and pentamethyldisiloxane.

The FTIR spectroscopy is the technique which allows a description of the most abundant neutral species produced in the HMDSO-containing plasmas. The most important issue provided by *in situ* detecting of the gaseous products containing the Si-O-Si, Si-O-C and Si-C molecular groups is the possibility to follow the formation of precursors of interest, although not directly. Besides, other stable neutral products of the HMDSO plasma-chemical conversion can detected: CH_4, C_2H_4, C_2H_6, CO, CO_2, etc. Raynaud et al showed that high discharge power ($> 50\ W$ at 6 $mTorr$ of initial pressure, DECR reactor) results not only in the enhanced fragmentation of HMDSO, but also in re-dissociation of hydrocarbons what, in turn, can lead to the increase of organic part in the film structure [126]. The infrared spectra, i*n situ* obtained in oxygen diluted HMDSO rf (13.56 MHz) plasma, revealed the presence of oxidation steps of the methyl groups, formaldehyde, formic acid CO, CO_2 and water, as combustion products [6]. Hollenstein et al made the conclusion that the carbon concentration in the deposit is controlled by the oxygen concentration due to heterogeneous oxidation processes. Moreover, the IR spectra showed that in highly oxygen diluted HMDSO plasma SiO_2 powders are produced whereas essentially SiO particles are formed in a plasma at high concentration of HMDSO [134].

IR diode laser spectroscopy offers significant advantages to gas phase diagnostics: very high wave-

length resolution, high space and time resolution, detection of transient species, possibility of quantitative analysis (particle density, vibrational and rotational temperatures). However, this technique have been not applied to the diagnostics of HMDSO plasmas. The first results in the study of hydrocarbons in the HMDSO-containing rf plasmas are presented in this work, see also reference [136].

Optical emission spectroscopy (OES) is the most popular technique for plasma diagnostics. This method allows one to probe only electronically excited states. Moreover, the concentration of the excited species are by orders of magnitude lower than that of ground state excited species which play the main role in the plasma chemistry in the gas phase as well as on the surface. Lamendola et al obtained the following information by means of actinometric OES as result of the study of the HMDSO rf discharge [128]:

— only Si- and H- atoms were detected in the pure HMDSO plasma;
— relative concentration of O-atoms almost linearly increases with the O_2 content in the feed;
— relative concentration of H-atoms is not affected by oxygen addition;
— relative concentrations of SiO, CO and OH radicals increase rapidly with the feed ratio O_2/HMDSO (up to the value 5) and then reach the plateau;
— relative concentrations of C-containing radicals like C and CH achieve an early maximum at O_2/HMDSO = 2 and then fall drastically;
— relative concentrations of Si-atoms decreases with the oxygen addition in the feed.

These observations support the author's hypothesis that SiO fragments are mainly produced as a result of the homogeneous gas phase reaction consuming silicon atoms. The presence of only Si and H radicals in the pure HMDSO plasma indicates a low degree of monomer fragmentation.

The knowledge of structure and composition of plasma deposited film is necessary both for the understanding of deposition mechanism and for the prediction of film properties or for an analysis of structure/property correlations. The latter issue represents a complex problem in itself. The properties of interest require that the plasma deposited film should possess appropriate structure and composition. Thus, the aimed film preparation can be realized if it is known, from one side, what structure and composition the final deposit should have and, from the other side, how process parameters influence on the plasma parameters and consequently on deposition mechanism. That is why, the analysis of growing film is a key issue of plasma processing of deposits.

There are numerous publications devoted to the study of correlations between process parameters and either structure/composition or properties of plasma deposited HMDSO films. Here are some general trends concerning structure and composition of plasma deposited HMDSO films (applied diagnostics is given in the brackets):

— the film morphology demonstrates spherical or hemispherical structures on the surface of plasma polymers at the appropriate process conditions [137, 138]. These structures can be built in the gas phase and then be incorporated in plasma polymer or can grow on the surface of plasma polymer.
— the structure of plasma polymerized organosilicones is not homogeneous, but consists of two regions at least:

- thin interface layer formed during the monomer conversion (typical of deposition in non steady state) [10];
- bulk, dense, cross-linked plasma polymer;
- top oligomeric layer of thickness of about 500 Å or top oxidated layer [10, 139].

— polymer chains of plasma deposited HMDSO film are linear [140 (FTIR), 106, 139, (P/GC)];
— in plasma polymerization at low energy input the films rich in organic (C_xH_y) constituent are formed;
  in high fragmentation regime, i.e. at high energy input, the silicone-like films are formed;
— relatively high oxygen admixture allows one to deposit SiO_2-like films;

Because of the complexity of gas phase composition only a model of deposition mechanism based on the macroscopic description is possible. The following kinds of models developed for the description of the plasma deposition can be pointed out:

— model based on the correlations of the deposition rate with the content of radicals or ions which are considered to be the precursors for the growing film [128];
— model based on the structural analysis or the correlations of deposition rate with the content of the appropriate molecular groups (e.g. Si-O-Si, SiO) and the process parameters [106,139, 141 − 143];
— model based on the correlations of deposition rate with the process parameters [1, 85, 93, 143].

The latter utilize often a concept of the composite process parameter W/FM proposed by Yasuda [1, 145] which means apparent input energy per mass of the monomer, where W, F and M are the discharge power, F is the flow rate and M is the monomer molecular weight respectively.

Presented above short overview summarizes results and trends of the research activity devoted to the HMDSO plasma deposition and allows one to mark out the problems have to be still studied. The following tasks were formulated for the investigation of the HMDSO deposition in rf low pressure discharge:

— to study the influence of the process parameters on the formation of molecular structure;
— to perform the structure analysis of the films deposited at the intensive and moderate ion bombardment;
— to investigate the formation of molecular structure of plasma deposited films at the various steps of plasma chemical conversion of the monomer.

The analysis of the optical and gas separating properties of the HMDSO plasma deposited films is also in the scope of this part of the work.

The first part of this chapter presents the results of the study of the gas phase. Neutral species were detected by means of mass spectrometry and tuneable diode laser absorption spectroscopy. Representative measurements were also carried out with the help of a combined gas chromotograph/ mass spectrometer system. The accent was done, first of all, on the monomer conversion process. The influence of the process parameters is analysed.

The deposition rate is analysed both in terms of the process parameters and a composite parameter analogous to that one introduced by Yasuda. The experimental data on the pressure dependence of the deposition rate is analysed also with the help of a simple model. An attempt to separate the contributions of ions and neutrals is done. The appropriate correlations of the deposition rate are compared with those describing the gas phase processes.

The third part of the chapter deals with the study of the formation of molecular structure. The main points of study have been mentioned above. The structural analysis were carried out by means of various techniques of FTIR spectroscopy including the developed fibre based tool.

The samples deposited at the conditions of extremely different energy input were examed respectively their optical and gas separating properties.

6.2 Analysis of gas phase

The accepted issue of the HMDSO plasma polymerization mechanism suggests that neutral species are the precursors of plasma polymer, ions contribute slightly in the film growth. Low degree of ionization in low pressure rf discharge makes the contribution of ions in the mass transport to a substrate negligible. That is why, the neutral component of HMDSO plasma was studied in detail in this work.

6.2.1 Ion component of HMDSO plasma

The ion component of the HMDSO plasma has been very intensively studied in discharges of various types. The main results of these studies are summarized here.

It seems impossible to determine experimentally the main processes leading to the ion formation in the HMDSO plasma among different possibilities: electron impact ionization of ground state molecules, Penning ionization, stepwise ionization, photo-ionization, ion-molecule reactions. Usually, the first process is considered as the main ionization channel. According to Schmidt et al [124] the rate coefficients of electron impact ionization of pentamethyldisiloxane ($m/z = 147$), 9.0×10^{-16} $m^3 s^{-1}$, and tetramethylsilane ($m/z = 73$), 5.1×10^{-16} $m^3 s^{-1}$, are higher than that of hydrocarbon (methane and methyl) ions, 9.0×10^{-17} $m^3 s^{-1}$ and 1.7×10^{-16} $m^3 s^{-1}$ respectively. As it was shown by Foest [125] the CH_3^+ ion is formed from low weight hydrocarbons and, moreover, via ion-molecule reactions. The electron impact ionization of methane results rather in production of CH_4^+ ions. The intensities not only of organosilicon ions, but also hydrocarbon ions (ethene and acetylene) decreased with the increase of the discharge power (up to 120 W at 10 Pa of total pressure), except methane and methyl ions.

6.2.2 Neutral component of HMDSO plasma

The mass spectrum of the monomer vapour, taken with the discharge switched off, is presented in Figure 31 (a). The detected fragment ions appear as a result of electron impact dissociative ionization in the ion source of the mass spectrometer, electron energy is 70 eV. Observed spectrum,

see Table 7, is in accordance with those reported in the literature [120 − 123, 146]. The signal from the parent ion at 162 m/z has very low intensity. The dominant peak at 147 m/z is ascribed to the monomer molecule since this fragment ion is the direct product of the cleavage of methyl group from the HMDSO molecule (162 u). According Schmidt et al the ionization of the HMDSO molecule is realized through the O-atom which posseses a free π-electron responding for a secession [120]. Because of the isotope presence, ^{29}Si and ^{30}Si, there are two additional peaks at 148 m/z and 149 m/z with relative intensities of 16% and 8%. The mass spectrum taken with the ignited discharge show the stable neutral products of the HMDSO fragmentation in the plasma, see Figure 31 (b). No signal was detected from the ions formed in the plasma.

The monomer molecules undergo strong fragmentation in the plasma at the chosen process conditions. The intensity of the peak at 147 m/z is drastically reduced while the signals of low molecular compounds become high. One should notice considerable intensities of atomic and molecular hydrogen mass signals. The fragment ion with 15 m/z is formed mainly from methane and organosilicon compounds as a result of dissociative ionization in the ion source. The orifice is far from the plasma zone so the methyl radicals formed in the plasma do not add significantly to the peak at 15 m/z.

The electron impact ionization cross section of CH_3^+ formation from ethane C_2H_6 (0.5×10^{-17} cm^2) [147] is nearly an order lower than that from methane (0.38×10^{-16} cm^2) [147] or HMDSO (0.35×10^{-16} cm^2) [123]. Thus, the contribution of ethane in the peak at 15 m/z is negligible. At high discharge power, when the monomer molecules as well as the high molecular organosilicon compounds are strong fragmented in the plasma, only methane can be considered as the main source of detected signal at 15 m/z. Moreover, the 15 m/z and 16 m/z fragment ions behave in the same way at the variation of process parameters.

Methyl radicals, formed as a result of the cleavage from the HMDSO and organosilicon molecules, recombine readily in the plasma zone giving the stable ethane molecules. The rate constant for this reaction is $(3.8 - 5) \times 10^{-11}$ $cm^3 molecule^{-1} s^{-1}$ [149, 150] comparing to 2.1×10^{-12} $cm^3 molecule^{-1} s^{-1}$ of the alternative reaction involving methyl radical and atomic hydrogen and leading to the formation of methane. The appropriate signals of the detected fragment ions from ethane molecules appear at 30, 28 and 26 m/z [151]. Indeed, the last two peaks are also due to the fragment ions of ethene and acetylene at 28 m/z and 26 m/z respectively. High concentration of ethane in the steady state of plasma-chemical conversion of HMDSO reflects the effectiveness of the HMDSO decomposition into siloxane and organic constituents. The high ethane content in the HMDSO plasmas was observed not only by mass spectrometry, but also gas chromatography and IR TD-LAS spectroscopy [134, 136].

The most complicated issue of the interpretation of mass spectra are various organosilicon species detected in the HMDSO plasmas. Among them one should note the 73 m/z ion which is the base peak of $Si(CH_3)_4$. The 147 m/z fragment is the base of the $(CH_3)_3SiOSi(CH_3)_2H$ molecule which is the precursor for the 133 m/z ion appeared as a result of the methyl group cleavage and for the 59 m/z ion, $(CH_3)_2SiH^+$. The molecule $(CH_3)_3SiH$ can be also the base of the 59 m/z ion what is confirmed by the appearance potential mass spectrum. Two appearance potentials are measured for this fragment ion: 12.1 eV and 22.2 eV. The second value is in agreement with that published in the literature [120, 123, 125] and corresponds to the 59 m/z ion formation from the $(CH_3)_3SiOSi(CH_3)_2H$ molecule.
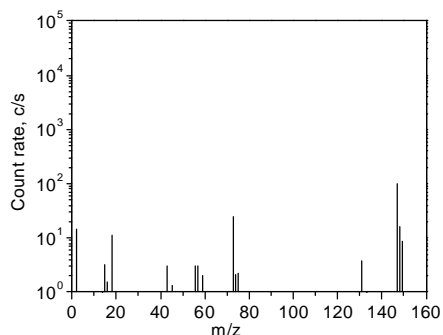
Figure 31(a).
The mass spectrum
of the HMDSO vapour
taken with plasma switched off.
Pressure 10 Pa,
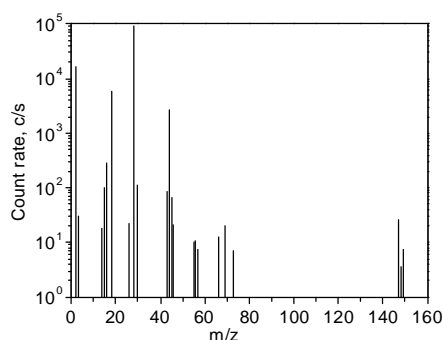HMDSO vapour flow rate 4 *sccm*.

Figure 31(b).
The mass spectrum
of stable neutral component
of the HMDSO plasma.
Process conditions:
discharge power 60 W,
gas pressure 10 Pa,
HMDSO vapour flow rate 4 *sccm*.

m/z	Relative intensity	Fragment ion
162		$(CH_3)_6Si_2O^+$
149	8.5	$(CH_3)_5\ ^{28}Si\ ^{30}SiO^+$
148	16.4	$(CH_3)_5\ ^{28}Si\ ^{29}SiO^+$
147	100	$(CH_3)_5Si_2O^+$
133	0.8	$(CH_3)_4Si_2OH^+$
131	3.8	$(CH_3)_3Si_2OCH_2^+$
75	2.2	$(CH_3)_2SiOH^+$; $(CH_3)_3\ ^{30}Si^+$
74	2.1	$(CH_3)_3SiH^+$; $(CH_3)_3\ ^{29}Si^+$
73	24.8	$(CH_3)_3Si^+$; Si_2OH^+
59	2.0	$(CH_3)_2SiH^+$
57	3.0	$CH_3CH_2Si^+$
56	3.1	CH_3CHSi^+
45	1.3	$(CH_3)SiH_2^+$; $SiOH^+$
43	3.1	CH_3Si^+
16	2.3	CH_4^+
15	3.2	CH_3^+
2	14.6	H_2^+

Table 7. The mass spectrum of the HMDSO vapour. The electron energy
in the ion source is 70 eV. Conditions: 10 Pa, 4 *sccm* HMDSO.

The identification of the neutral species giving the rise to the peaks at 45 m/z and 43 m/z seems too ambiguous and requests additional information on these fragment ions: appearance potential, shape of the ion efficiency curve, fragment ion energy distribution function, etc. The fragment ions $(CH_3)SiH_2^+$ / $SiOH^+$ (45 m/z) as well as methylsilane ion, $(CH_3)Si$ (43 m/z), can appear from various organosilicon molecular patterns of the HMDSO molecule fragmentation.

6.2.3   HMDSO plasma-chemical conversion in rf discharge

The time evolution of mass spectra shows formation and consumption of important stable compounds in the plasma after the discharge ignition. The HMDSO content decreases continuously after the ignition while organosilicon molecules, hydrocarbons and hydrogen are formed in the gas phase with the process time. In the case of the system without gas flow, the HMDSO molecules are fragmented completely up to molecular hydrogen and light weight hydrocarbons. The increase of the density of the low molecular species, particularly molecular hydrogen, results in the enhancement of the total pressure, see Figure 32.

This conversion is demonstrated for some chosen species in Figure 33. Poll et al [10, 152] who first studied the HMDSO conversion in the closed vacuum chamber found out very intensive formation of $C_2H_4^+$ and CH_4^+ fragment ions in the plasma at the similar process conditions.

The monomer conversion in the system with the gas flow leads to the moderate fragmentation of the HMDSO molecules and is characterized by the constant gas phase composition at the steady state, see Figure 34.
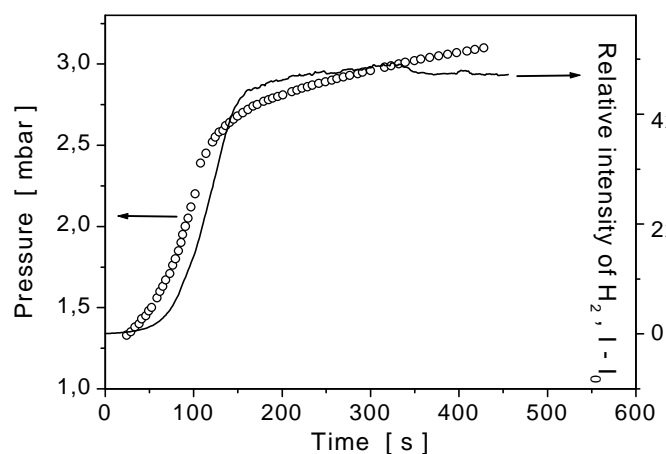

Figure 32. The increase of the total pressure and the H_2 content in the closed chamber during the time after the discharge ignition at the initial pressure 10 Pa and 60 W power. I_0 is the count rate (MS) without discharge.
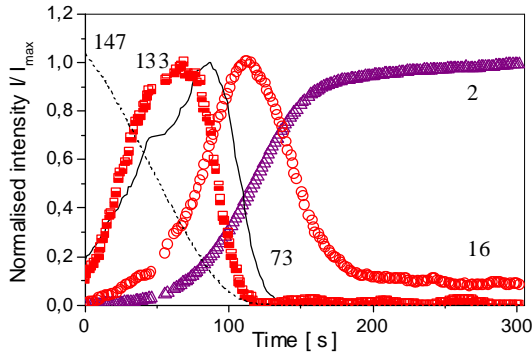
Figure 33. The monomer conversion in rf discharge ignited in the closed chamber. Process conditions: 60 W, 10 Pa. Short dash line: 147 m/z. Half-filled squares:133 m/z. Open triangles: 2 m/z. Solid line: 73 m/z. Open circles: 16 m/z.
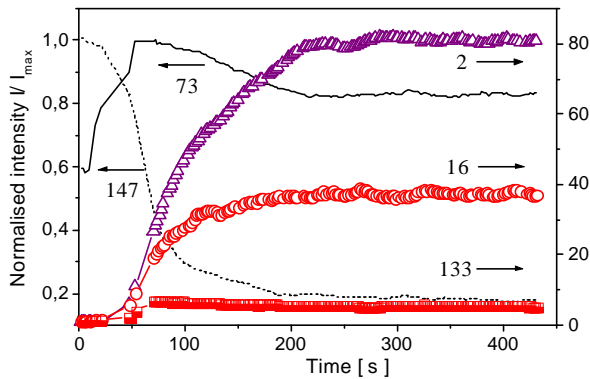

Figire 34. The monomer conversion in rf discharge ignited in the chamber with gas flow at the following conditions: 60 W, 10 Pa, f_{total} 4 $sccm$, HMDSO:Ar 9:1. Short dash line: 147 m/z. Half-filled squares: 133 m/z. Open triangles: 2 m/z. Solid line: 73 m/z. Open circles: 16 m/z.

6.2.4   Influence of process parameters

Discharge power was varied in the range from 40 to 200 W at 15 Pa total pressure and 5 $sccm$ monomer flow rate. The enhancement of discharge power leads to the decrease of the signal intensities of high molecular compounds, see Figure 35(a). The absolute concentration of methane and ethane molecules was measured by means of IR TDLAS in the plasma zone which is 12 mm above the rf electrode. Nevertheless, the mass spectrometric measurements on these species done in the wall region correlate with those obtained by the IR TDLAS. The ethane density is nearly constant, the methane content grows with discharge power and reaches the maximum level, compare Figure 35(b) and Figure 36.

The total pressure was varied in the small range from 8 to 50 Pa at the discharge power of 130 W and the HMDSO flow rate of 5 $sccm$. The increase of the total pressure leads to the growth of the concentration of high molecular species, see Figure 37(a). The energy shortage to maintain the strong fragmentation of high molecular species evokes the drop of the density of low molecular species: hydrogen and methane, see Figure 37(b). The studies of hydrocarbons in the HMDSO rf plasma by the IR TDLAS revealed analogous pressure dependency of the density for methane and ethane molecules, see Figure 38.
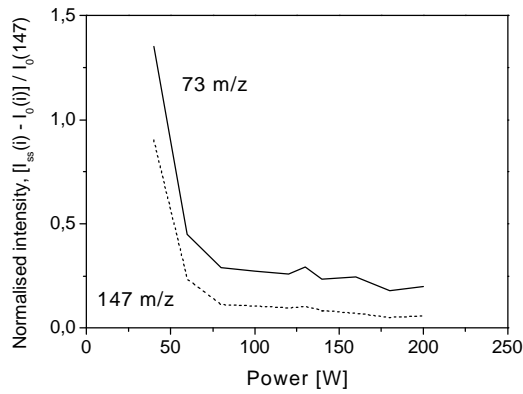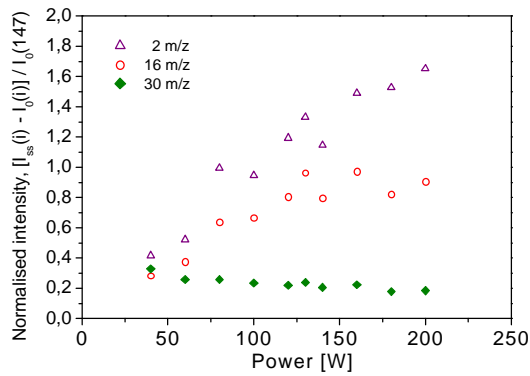
Figure 35
Power dependency of the normalized intensity $[I_{ss}(i)\text{-}I_0(i)]/I_0(147)$ of the i fragment ion, where $I_{ss}(i)$ is the intensity of the i fragment ion in the steady state, $I_0(147)$ is the intensity of the 147 m/z ion without discharge.
Process conditions: HMDSO, 15 Pa, 5 $sccm$.

(a) The 147 m/z and 73 m/z fragment ions formed from organosilicon compounds $[(CH_3)_6Si_2O]/[(CH_3)_5Si_2O]$ and $[(CH_3)_4Si]/[(CH_3)_3Si]$ respectively.

(b) The fragment ions 2 m/z , 16 m/z and 30 m/z formed from low molecular species H_2, CH_4 and C_2H_6.
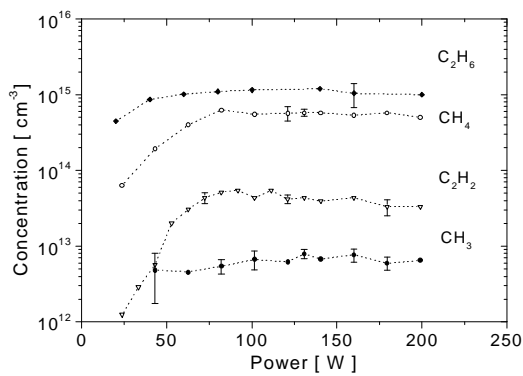
Figure 36. Power dependency of the molecular concentration of hydrocarbons in a pure HMDSO plasma measured by IR TDLAS.
Process conditions: 15 Pa, 5 $sccm$.
Solid diamant - C_2H_6; filled circle - CH_3; down triangle - C_2H_2 ; open circle - CH_4
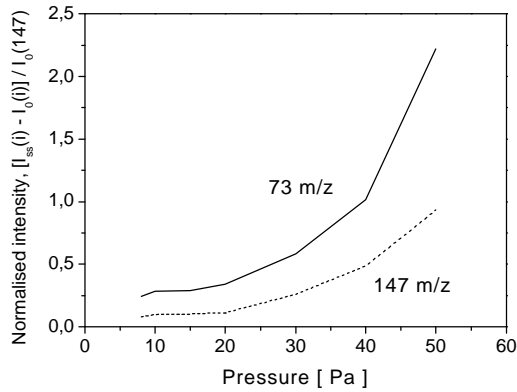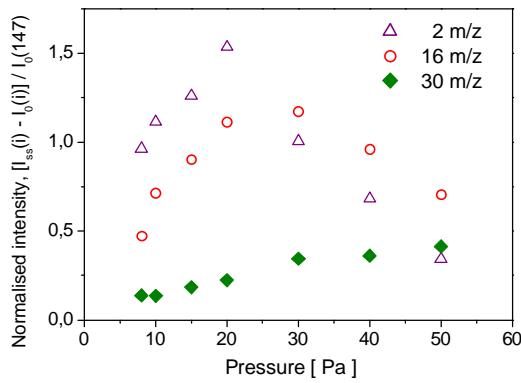.

Figure 37.
Pressure dependency of the normalized intensity
$[I_{ss}(i)\text{-}I_0(i)]/I_0(147)$ of the i fragment ion,
where $I_{ss}(i)$ is the intensity of the i fragment
ion in the steady state, $I_0(147)$ is the intensity
of the 147 m/z ion without discharge.
Process conditions: HMDSO, 130 W, 5 $sccm$.

(a) The 147 m/z and 73 m/z fragment ions.

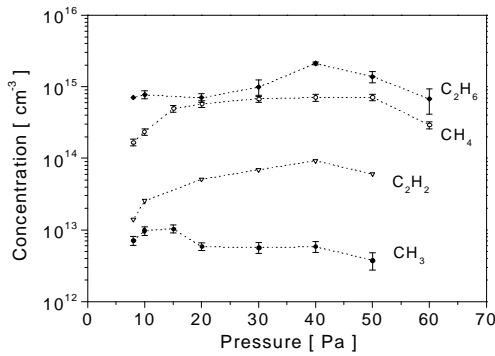(b) The fragment ions 2 m/z , 16 m/z
and 30 m/z.

Figure 38. Pressure dependency
of the molecular concentration of hydrocarbons
in a pure HMDSO plasma
measured by IR TDLAS.
Process conditions: 15 Pa, 5 $sccm$.
Solid diamant - C_2H_6; filled circle - CH_3;
down triangle - C_2H_2; open circle - CH_4.

In contrast to the IR TDLAS, mass spectrometry does not provide quantitative analysis of the concentrations. Nevertheless, the electron impact mass spectra of the gas mixtures H_2/CH_4 and H_2/C_2H_6 taken without discharge ignition showed that the data presented on the appropriate figures reflect the real proportions of molecular hydrogen, methane and ethane. The following gas mixtures were prepared: $CH_4 : H_2 = 16\% : 84\%$ (or 0.2) and $C_2H_6 : H_2 = 83\% : 17\%$ (or 4.9) for the trial . The measurements were done at the conditions used in the studies on the HMDSO plasma in this work: 15 Pa, f_{total} 5 *sccm*. The intensity $(I-I_0)$ was measured in the same way described above. I is the fragment ion intensity taken at the ignited discharge, I_0 is the fragment ion intensity in the electron impact mass spectrum without plasma. The observed intensity relations give the values: $I_{CH_4} : I_{H_2} = 0.1$, $I_{C_2H_6} : I_{H_2} = 4.8$. Thus one has the same gas mixture proportions at the output as at the input.

The characteristic HMDSO conversion time τ_{conv} is defined as the time of the exponential fall of the intensity (I_0-I) of the 147 m/z fragment ion. The fragmentation rate, defined as $(I_0-I)/\tau_{conv}$, and the conversion time are the function of the process parameters. The HMDSO fragmentation rate grows with the energy input. Figure 39 shows the appropriate dependencies of both values on the composite process parameter ϕ, analogous to that introduced by Yasuda [1].

The effectiveness of such parameters for the description of plasma polymerization has been discussed in detail by many authors, e.g. see the overview by Morosoff [153]. This parameter can be used for comparison of the influence of different experimental conditions on deposition rate, molecular structure and macroscopic properties of plasma polymer films. The composite process parameter is given by:

$$\phi = WkT/(pMf) \tag{48}$$

where W is the discharge power, T is the gas temperature (300 K was taken here), p is the total gas pressure, M is the monomer molecule mass, f is the monomer flow rate. Here, this parameter is used for the analysis of the behaviour of the gaseous species in dependence on the energy input. The characteristic conversion time of the 147 m/z fragment ion drops drastically with the increase of the composite parameter and reaches the minimum value at the parameter ϕ of about 10^{12} J kg^{-1} , see Figure 39. The fragmentation rate reaches its maximal value. The variation of the discharge power and the total pressure result in the similar dependencies of the HMDSO fragmentation rate and the conversion time on the parameter ϕ. The parameter value of about 10^{12} J kg^{-1} can be designated as a critical value, ϕ_C, characterizing the minimal input energy necessary for the maximal conversion of the monomer molecules into the active species which are the precursors for a thin film. It seems that the concentration of such species should reach the maximum at the critical value of the composite parameter. Among the analyzed species the fragments with 133, 75, 74, 73, 45 m/z have a maximal level at the ϕ_C. Then, the deposition rate should attain the maximum at the ϕ_C also.

The admixture of oxygen to monomer results in acceleration of the hexamethyldisiloxane fragmentation in discharge, see Figure 40. Low content of oxygen ($< 60\%$ in monomer flow at the chosen process conditions) does not influence on the hydrocarbon chemistry: the content of hydrocarbons as well as their behaviour on process parameters are nearly the same as in the pure HMDSO plasma, see Figure 41.
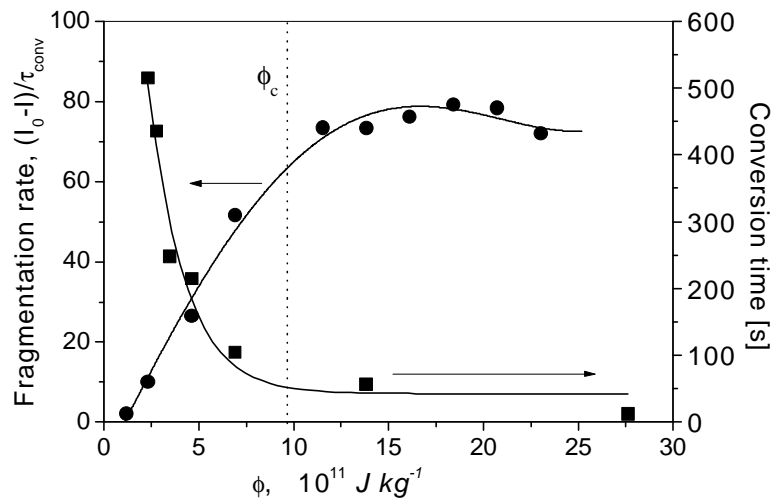
Figure 39. The fragmentation rate as well as the conversion time in dependence on the composite
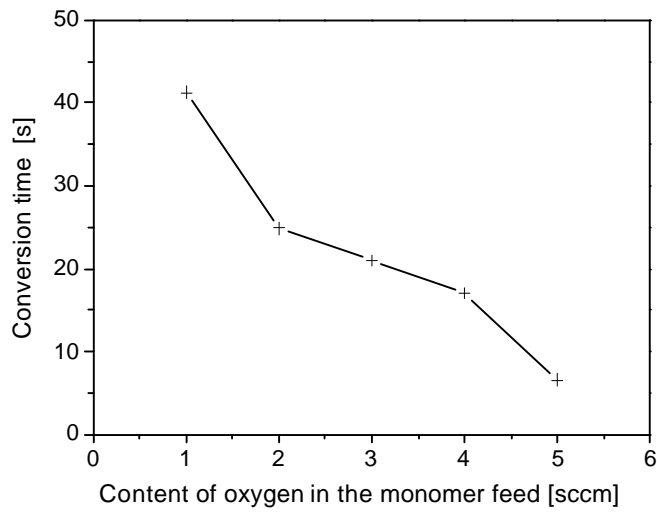parameter ϕ.

Figure 40. Influence of the oxygen content in the monomer feed on the HMDSO conversion time.
Process conditions: 15 Pa total pressure, 130 W discharge power, 6 *sccm* total flow rate.
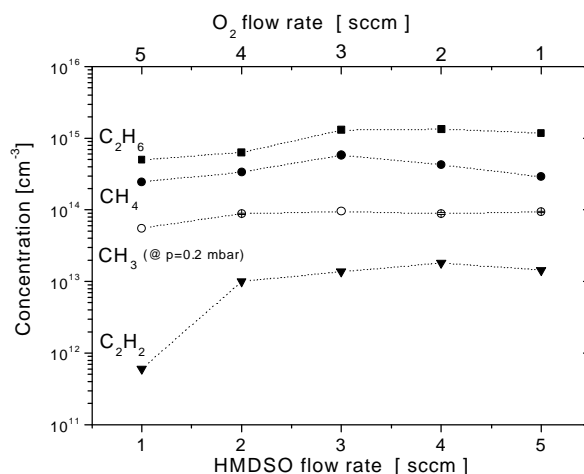
Figure 41. Influence of the oxygen content in the monomer feed on concentrations of hydrocarbon products. Process conditions: 15 Pa, 130 W. Open circle - CH_4; solid diamant - C_2H_6; filled circle - CH_3; down triangle - C_2H_2.

High oxygen dilution of the HMDSO plasma results in the intensive building of CO, OH C_xH_yO species in the gas phase and promotes the formation of SiO radicals, SiO_2 and other Si-containing products of oxidation reactions in the gas phase. This trend has been observed experimentally by Lamendola et al [127] who found the strong increase of densities of SiO, CO, OH with the enhancement of the oxygen content in the monomer feed.

6.3   Film deposition

6.3.1   Influence of process parameters on deposition rate

There is no any plasma-chemical equilibrium state in the case of closed reactor, i.e. without monomer flow. The film deposition in such a system allows to make some interesting conclusions about the process. As it was shown above, the composition of gas phase in reactor is a function of discharge ignition time, see Figures 33 and 34. Hence, the film growth is also dependent on the process time. While there is sufficient organosilicon species in the gas phase, the deposition rate is constant, see Figure 42. After the monomer is used up, plasma polymer film does not grows further. Earlier study has shown that the plasma-chemical conversion of HMDSO reflects itself not also in the deposition kinetics, but also in the composition of the PP HMDSO films [154].

The content of the gaseous stable products of plasma-chemical conversion as well as the deposition rate of a solid state product, i.e. thin film, should reach the maximum level at high values of power input. IR TDLAS measurements of absolute concentrations of stable hydrocarbons in the HMDSO plasmas [136] confirm this suggestion, see Figure 36. The discussed behaviour of the fragmentation rate and the conversion time of the HMDSO fragment ion (147 m/z) assumes two distinct ranges of the deposition rate dependency on the power input.
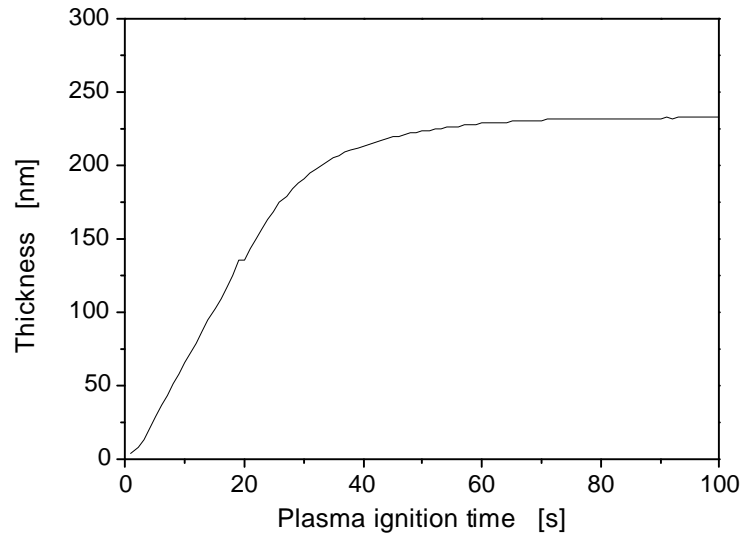
Figure 42. The thickness of the HMDSO plasma deposited film as a function of the process time. Process conditions: closed reactor, 10 Pa initial pressure, 60 W discharge power.

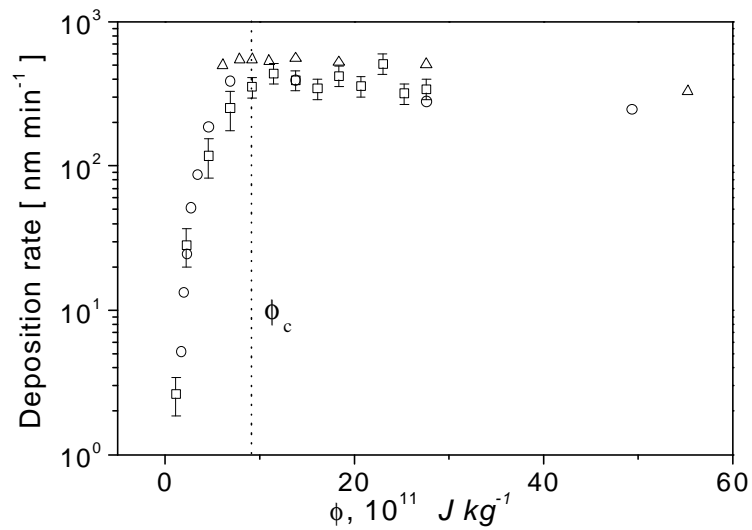Figure 43. The HMDSO film deposition rate in the dependence on the composite parameter ϕ obtained at the ($\square$) power variation (10 Pa, 4 *sccm*), (O) pressure variation (60 W, 4 *sccm*), ($\triangle$) monomer flow rate variation (60 W, 10 Pa).

Firstly, the range of low energy input where the deposition rate increases strongly due to the raising fragmentation of the monomer molecules and the intensive formation of the active species. Secondly, the range of the maximal deposition rate where a slight dependency on the energy input is due to a complete fragmentation of the monomer molecules. Figure 43 shows the HMDSO deposition rate in dependence on the composite process parameter. The curves represent the variation of a single process parameter: power, pressure or monomer flow rate. Here the composite parameter is used for the description of the surface process in contrary to the analysis of the HMDSO fragmentation kinetics in Part 6.2.3 where it was applied to the gas phase process.

Indeed, such a composite process parameter can be expressed in terms of the basic plasma parameters [155]: the electron density n_e, the electron energy distribution function $f(E_e)$, the gas density N and the residence time for a gas molecule in plasma τ_{res}, which determine the scheme of elementary reactions in the gas phase as well as on the surface and, hence, the overall deposition process (process kinetics) as well as the deposits (composition and molecular structure of deposited films and consequently their properties). In the literature such composite process parameters have been used mainly for the study of correlations between deposition conditions, deposition rate and/or film structure and properties, i.e. focusing on the surface processes and the solid state products of the deposition, e.g. [1, 153, 156, 157].

The simple estimation of the current density shows that the film formation should be determined by neutral species [124]. These active neutral species are formed mainly as result of electron impact reactions. Meichsner et al [20] measured the axial electron density distribution in low pressure capacitively coupled discharge for the asymmetric reactor geometry. They found the n_e has the maximum (at $\sim 2\ cm$ from the rf electrode) in the region of the plasma sheath and falls sharply in the axial direction with the distance from the rf electrode, see Figure 2(b). The active neutral species should have the similar axial distribution as electrons what, in turn, reflects on the dependence of deposition rate on the distance between substrate and rf electrode. The measurements of the deposition rate showed the strong decrease with the distance from the rf electrode with the maximum value on the electrode what can be explained by the effect of ion bombardment. The control of the deposition process is brought into the effect by ions through the surface activation and/or initiation of the growth reactions on the surface. The ion bombardment of the substrate on the rf electrode is very intensive due to the negative self bias voltage, see e.g. Figure 3(a). Due to both factors the deposition rate on the rf electrode is nearly one order of magnitude higher than that at the distance of 125 mm from the electrode, where the substrate is under the floating potential: 350 $nm\ min^{-1}$ vs 30 $nm\ min^{-1}$.

6.3.2 Model analysis of deposition rate

In order to analyse the influence of the main process parameters like discharge power and monomer pressure, the following simple model is suggested.

The model of plasma polymer growth assumes the following stages:

i) as a result of ionization and dissociation processes active species, n_a, (the appropriate

values are marked with an index '$_a$' are formed from the monomer molecules in the gas phase; for the sake of simplicity all types and sorts of active species are treated as single type (under the type of active species one assumes ions, radicals, metastable particles; the various kinds of particles of a specific type are treated as sorts of particles for a given type)

ii) then occurs an adsorption of a monolayer of active species on the substrate surface. The adsorption is considered under the following assumptions:
— this is a localized adsorption;
— there is no interactions among absorbed particles;
— the adsorption centers have equal affinity to the active species.
The covering grade is represented by the Langmuir isotherm: $\Theta = K_{ads}\, n_a\, /\, (1 + K_{ads}\, n_a)$

iii) the growth of PP is envisioned to occur via the heterogeneous bimolecular reactions between the active species from the gas phase and the absorbed particles at the initial step, and the growing macroparticles of a plasma polymer later.
These reactions take place only on the activated centres which appear as a result of ion bombardment. It is assumed, that all ions crossing the plasma sheath boundary accelerate within the sheath and strike the substrate or growing film with high energy enough to form such an activated centre.

The growth of the film thickness is analysed here. The deposition rate is defined as

$$L \equiv a^3 dn_s/dt \qquad\qquad (49)$$

where n_s is the surface concentration of the growing plasma polymer, a is the characteristic size of an active particle. The latter varies in dependence on the kind of a particle, but for the current analysis it is not necessary to determine this parameter exactly, one can take for a quantitative estimation the value of the characteristic size of HMDSO molecule.

We consider here only the process of the plasma polymerization on the surface. The incorporation of the oligomers into the growing matrix of plasma polymer is neglected. The ratio of the values of the collision frequencies in the gas phase and the gas-surface interphases, which determine the rate constants for the appropriate bimolecular reactions, is proportional to the total pressure. The pressure was not varied in a wide range and, moreover, the value of the total pressure was relatively small, $5 - 150$ Pa . Moreover, the surface of the deposited plasma polymer was controlled by scanning electron microscopy and very smooth surface without microparticles was observed for plasma polymers deposited on Si wafers.

There are two main channels for a film growth in accordance with the type of the active species: ion polymerization, radical polymerization. Here these mechanisms do not mean their chemical analogs and show only the type of the active species, which make a main contribution to the growth process. Taking into account the properties of the rf discharge one can expect that the ion polymerization makes remarkable contribution in the deposition kinetics and, hence, the dependence of the deposition rate on the main parameters (pressure, power) will be determined by this polymerization mechanism. Among the rf discharge properties one points out the existence of plasma sheathes, where the ions are accelerated passing through them, the higher sheath voltage at the powered

electrode because of the asymmetrical electrode geometry. These issues are very well described in the literature reviewing the physics of the capacitively coupled rf discharge, e.g. see [21, 22] nad chapter II of this work.

As it was defined, the deposition rate is determined by the time derivative of the surface concentration of the growing macroparticles, dn_s/dt. According the model the film grows through the active centres which are formed as a result of bimolecular heterogeneous reactions between the ions which go on the substrate surface from the sheath, A, and the adsorbed at the initial stage particles, A_s, which form the first monolayer, and the growing macroparticles later: $A + A_s \rightarrow P_j$. The reaction rate is defined as following:

$$dn_s/dt = Z/n_{s0} \cdot j_i \cdot \tau_0 \tag{50}$$

The first term describes the collision frequency with the adsorbed particles, $Z = 9.49 \times 10^{20} p_a (M_a T)^{-1/2}$ $[s^{-1}]$; n_{s0} is the surface concentration of the absorbed particles (first monolayer). The second term defines the quantity of the ions coming on the surface unit. j_i is the ion flux from the sheath to the substrate surface, τ_0 is the characteristic flight time through the sheath. Ion flux can be estimated by the expression: $j_i = e n_i u_b$, where u_b is the Bohm velocity. The deposition rate is independent on the plasma-on time, see Figure 44.

In the steady state the ion balance equation looks like a following:

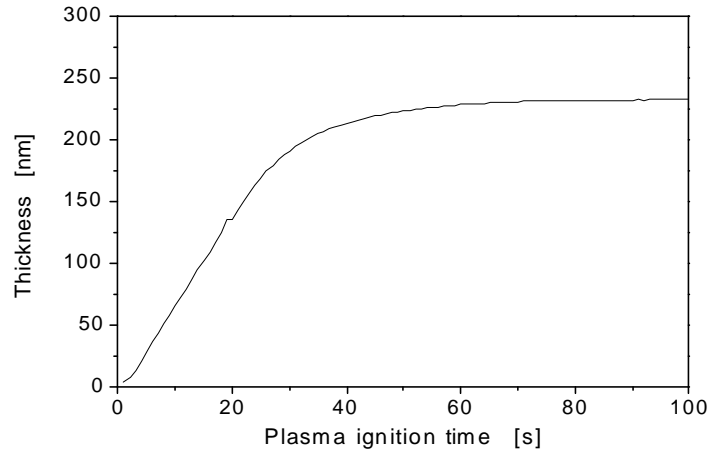$$0 = \nu_i n_e - \beta_{dis} n_e n_i - n_i/\tau_{dif} \tag{51}$$

Figure 44. The thickness of the growing plasma polymerized HMDSO film vs plasma-on time. Process conditions: 10 Pa, 60 *W*, 2 *sccm* HMDSO.

The ion disappear as a result of dissociative recombination and diffusion on the walls. Here we are interested in the ion concentration as a "source" for the following plasma polymerization, that is why the possible termination term, describing the deposition, is absent. The characteristic time τ_{dif} is defined by the volume sizes and the ambipolar diffusion coefficient, $\tau_{dif} = \Lambda^2/\mathrm{D}_{amb}$, where $\Lambda = ((2.4/R)^2 + (\pi/l)^2)^{-1/2}$ for the cylindrical geometry with radius R and hight l .

Because of the non-equilibrium plasma, it is possible to use the expression $\mathrm{D}_{amb} \approx \mu_i T_e/T_i$, or, taking into account the pressure dependence of the ion mobility coefficient, $\mathrm{D}_{amb} \approx \gamma_i \mathrm{M}_i T_e/T_i p$, where γ_i is the constant for specific ion, M_i is the ion mass. Thus, the equilibrium ion concentration is equal to:

$$n_i = \nu_i n_e/(\beta_{dis} n_e + \gamma \mathrm{M}_i T_e/T_i p \Lambda^2) \tag{52}$$

The estimations of the characteristic frequencies in rf discharge for the experimental conditions, used here, show that $\nu_m >> \omega > \nu_u$, where $\omega = 8.5 \times 10^7 \ s^{-1}$, ν_m is the electron elastic collision frequency; ν_u is the frequency of the energy loss for electrons as result of collisions with neutral particles, $\nu_u = \nu_m \delta$. This inequality means that energy spectrum of electrons does not react on the field oscillations and one can use the effective field value for the estimation of the ionization frequency [21, p. $26-27$]:

$$E_{eff} = E_0/\sqrt{2} \cdot \nu_m/(\omega^2 + \nu_m^2)^{1/2}, \qquad \nu_i = \nu_i(E_{eff}) \tag{53}$$

In this case the following pressure dependence can be used: $\nu_i \approx \upsilon_{de} A p \exp(-Bp/E_{eff})$ where υ_{de} is the electron drift velocity, A, B are the constants. The pressure dependence of the concentration of the active species has the following form:

$$n_i \approx n_e \upsilon_{de} A p \exp(-Bp/E_{eff})/(\beta_{dis} n_e + \gamma_i \mathrm{M}_i T_e/T_i p \Lambda^2) \tag{54}$$

Adsorption of the active species on the substrate surface occurs according the model conditions, (ii). The surface concentration of the absorbed particles of the first monolayer is defined as $1/\Theta S$, where S is the surface area. So one can obtain the equation for the deposition rate:

$$L = a^3 S Z e \mathrm{u}_b \tau_0 K_{ads} n_a^2/(1 + K_{ads} n_a) \tag{55}$$

Combining with the (54), one can get:

$$L \approx a^3 \eta p S e \mathrm{u}_b \tau_0 K_{ads} (n_e \upsilon_{de} A p)^2 \exp(-2Bp/E_{eff})/(\Sigma^2 + \Sigma K_{ads} n_e \upsilon_{de} A p \exp(-Bp/E_{eff})) \tag{56}$$

where $\eta = 9.49 \times 10^{20} (\mathrm{M}_i T)^{-1/2}$, $\Sigma = (\beta_{dis} n_e + \gamma_i \mathrm{M}_i T_e/T_i p \Lambda^2)$.

We consider, for the sake of a simplicity, only the drift velocity as the pressure-dependent parameter among the all members in brackets in the last equation. Let us estimate this dependence. In this model the transport cross-section and the free path are treated as constant. For a rough estimation the mean velocity value is derived under the assumption of the maxwellian distribution:

$$m\overline{u}^2 = 16/3\pi < \varepsilon > \tag{57}$$

The value of the average energy is obtained from the energy balance equation for electrons: $d\varepsilon/dt = (e^2 E_{eff}^2/m\nu_m^2 - \delta\varepsilon)\nu_m$. Thus one has: $< \varepsilon >= e^2 E_{eff}^2 \lambda^2/m\overline{u}^2 \delta$, and then, combining with (57):

$$< \varepsilon >= \sqrt{3\pi}/4 \cdot \delta^{-1/2} e E_{eff} \lambda \approx 0.8 kTe \sigma_{tr}^{-1} \delta^{-1/2} E_{eff}/p \tag{58}$$

The drift velocity is equal to: $v_{de} = \mu_e E$. Taking into account that $\mu_e = e/m\nu_m$, one obtaines: $v_{de} = eE/mn_e\bar{u}\sigma_{tr}$. Now one can get the following expression from the (57) and (58): $v_{de} \approx 0.9\delta^{1/4}(kTe/m\sigma_{tr})^{1/2}(E_{eff}/p)^{1/2}$. Thus the pressure dependence of the deposition rate has the following form:

$$L \approx \frac{a^3\eta p S e u_b \tau_0 K_{ads} n_e^2 0.81\delta^{1/2}(kTeE_{eff}/m\sigma_{tr})pA^2 \exp(-2Bp/E_{eff})}{(\Sigma^2 + \Sigma K_{ads}n_e 0.9\delta^{1/4}(kTeE_{eff}/m\sigma_{tr})^{1/2}p^{1/2}A\exp(-Bp/E_{eff}))} \qquad (59)$$

So dependence of the deposition rate on the total pressure can be described by the following general expression:

$$L \sim \frac{const_1 \cdot p^2 \exp(-2const_2 \cdot p)}{(const_4 + const_5/p)^2 + (const_4 + const_5/p)(const_3 \cdot p^{1/2}\exp(-const_2 \cdot p))} \qquad (60)$$

where: $const_1 = a^3\eta S e u_b \tau_0 K_{ads} n_e^2 0.81\delta^{1/2}(kTeE_{eff}/m\sigma_{tr})A^2$; $const_2 = B/E_{eff}$; $const_3 = K_{ads}n_e 0.9\delta^{1/4}(kTeE_{eff}/m\sigma_{tr})^{1/2}A$; $const_4 = \beta_{dis}n_e$; $const_5 = \gamma M T_e/T_i \Lambda^2$.
The experimental and simulated pressure dependencies of the deposition rate in the continuous rf discharge are shown in Figure 45. Here are the results of fitting: $const_1 = 8.1 \times 10^{18}$, $const_2 = 0.07538$, $const_3 = 7.4 \times 10^8$, $const_4 = 3.6 \times 10^8$, $const_5 = 3.0 \times 10^{-3}$, $\chi^2 = 271.8$.

It is very difficult to make an accurate analysis of the influence of discharge power in frame of the proposed model. At other fixed process parameters the input energy determines too many plasma parameters in a complicated way to be described analytically: electric field, plasma potential, energy distribution function for electrons and ions, sheath structure. Nevertheless, a rough estimation of the possible dependence of the deposition rate on the ϕ parameter can be done. The data obtained under the following experimental conditions were chosen for analysis and fitting procedure: total monomer pressure 10 Pa, flow rate 2 *sccm*. The following rough assumptions were made to choose the energy dependent parameters: $E^2 \sim W \sim (pMf/kT)\cdot\phi$, $n_e \sim \phi$, $u_i \sim \phi^{1/2}$. So from (59) follows the dependence of the deposition rate on the ϕ parameter in general form (under C_i, $i = 1-6$, one assumes the constants):

$$L \sim \frac{C_1 \cdot C_2^2\phi^3 \exp(-2C_6\phi^{-1/2})}{(C_4\phi + C_5)^2 + C_2C_3\phi^{5/4}\exp(-C_6\phi^{-1/2})(C_4\phi + C_5)} \qquad (61)$$

Note, that the constants C_i from (61) are associated with the constants $const_i$ from (60) in the following way:
$C_4 = const_4 n_e^{-1}$; $C_5 = const_5 p^{-1}$;
The value of C_5 can be fixed taking into account the results of the fitting of the pressure dependence, $C_5 = 10^{-4}/p$. The experimental as well as simulated dependencies are presented in Figure 46. Despite of the high value of χ^2, both dependencies have qualitatively the same character. The results of the fitting: $C_1 = 3.07944$, $C_2 = 6.1 \times 10^{45}$, $C_3 = 0.17806$, $C_4 = 0.52586$, $C_5 = 0.03015$, $C_6 = 0.04248$, $\chi^2 = 53014.1$. It follows that $n_e \sim 10^9$ cm^{-3} what is a reasonable value.
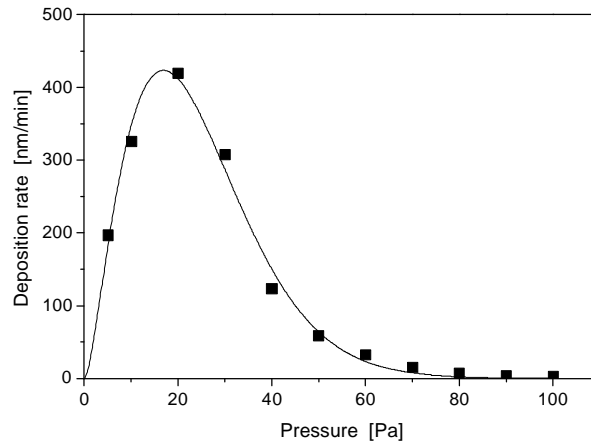
Figure 45. The HMDSO deposition rate vs total pressure.
          The experimental data (symbols) and fitting line.
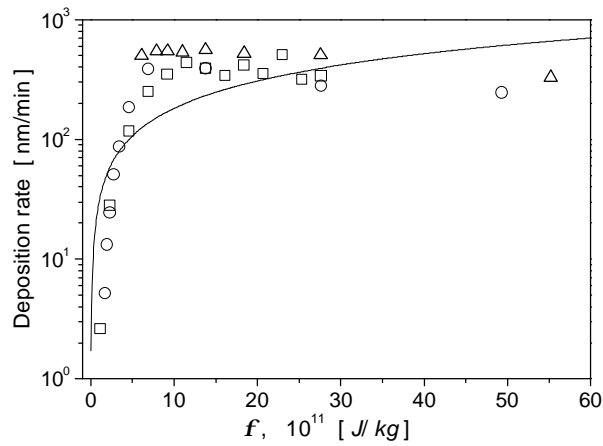   Process conditions: 60 W, 2 $sccm$ HMDSO flow rate.

Figure 46. The HMDSO deposition rate vs energy input.
          The experimental data (symbols), see Figure 43,
          and fitting line.

6.4   Chemical structure and composition

of plasma deposited films

6.4.1   Molecular structure of HMDSO

Molecular structure of hexamethyldisiloxane molecules has been intensively investigated by various methods: study of thermodynamic properties of the compound, IR and Raman spectroscopy, electron diffraction, etc $[158 - 160]$. The data on the molecular structure of HMDSO are presented in Appendix A. Interpretation of the vibrational spectra of hexamethyldisiloxane is well established and is used for the determination of molecular structure of plasma polymerized HMDSO films. Normal coordinate calculations provided the frequencies of HMDSO vibrations and force constants, see Appendix A.

The absorption lines caused by vibrations of the Si-containing linkages are very intensive due to ionic character of silicon bonds. The intensity of the absorption line depends not only on the electric charge located on the atoms, but also on the effective vibrating charges. Wright and Hunter [158] used a Pauling's concept of the ionic character to compare the intensities of infrared absorption lines of various bonds. They showed that the ratio of the ionic character of the Si-O and C-O bonds is exactly the same as the ratio of the intensities of the Si-O and C-O absorption peaks. The ratio of ionic character of the Si-O bond to that of C-O was estimated to have the value of 2.3. Some ionic character is also indicated for the Si-C bond. The vibration bands about 1250 cm^{-1} and 850 cm^{-1} wavelengthes are fairly strong. The Si-C dipole moment increases as the number of oxygen atoms attached to the silicon from 0 to 2. The inductive effect of the Si^+-C^- dipole results in a lessening of the C-H dipole moment in the Si-CH$_3$ groups in comparison with the C-CH$_3$. That is why, the absorption bands at 2900 cm^{-1} of the methyl group in Si-CH$_3$ are weak relative to those in C-CH$_3$. Moreover, attachment of oxygen atom to the silicon causes a further weakening of the methyl C-H band absorption.

The barrier to internal rotation of methyl group attached to silicon atom is relatively independent on the molecular environment. However, the barrier height differs from that one of methyl groups connected with carbon or oxygen atoms. The facts mentioned above can be used for the determination of the molecular structure of plasma polymerized HMDSO.

6.4.2   Influence of energy input

As it was shown above, there are two characteristic regimes of energy input determining the monomer conversion and the rate of deposition: the range of high energy input and the range of low energy input. The FTIR absorption spectra of two samples deposited on rf electrode are compared in Figure 47. Both films of the equal thickness of about 30 nm were deposited in the pure HMDSO plasma. The film PP HMDSO (I) is deposited in the regime of relatively low fragmentation, see Figure 39, when the deposition rate is small, see Figure 43. One could expect
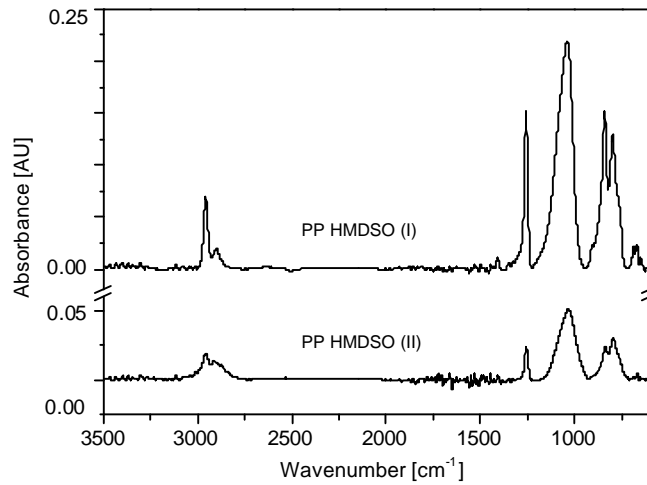
Figure 47. The FTIR absorption spectra of plasma polymer films deposited in
a pure HMDSO plasma at the different values of energy input.
PP HMDSO (I): $\phi = 1.2 \times 10^{11}$ J/kg (10 W, 10 Pa, 8 $sccm$).
PP HMDSO (II): $\phi = 2.8 \times 10^{12}$ J/kg (60 W, 10 Pa, 2 $sccm$).

the plasma polymer possesses a monomer-like molecular structure what is experimentally confirmed. The more intensive fragmentation and higher deposition rate result in the building of the dense PP HMDSO film. That is why, the intensity of absorption lines of PP HMDSO (II) film is considerably lower than those of PP HMDSO (I).

The absorption line due to symmetrical CH_3 bending vibration at the 1256 cm^{-1} reflects the content of methyl groups originated from monomer fragments. Two main sources of methyl groups can be assifned to the absorption line at the 2960 cm^{-1} : monomer fragments and hydrocarbons formed in the plasma. The latter can incorporate into the plasma polymer or build organic active species in the plasma which can then react with the growing film. The ratio of intensities of absorption line $I(1256\ cm^{-1})/I(2960\ cm^{-1})$ is higher for PP HMDSO (II), 1.48, than for PP HMDSO (I), 1.24. It means, that despite both films contain considerable organic constituent, its origin is quite different and depends upon the grade of the monomer fragmentation in plasma. The high fragmentation regime is more preferable for a deposition of SiO_x-like films. Taking into account the later conclusions, for deposition such films one should provide the process conditions which exclude the influence of the hydrocarbon chemistry in the plasma on the growth process on the surface.

6.4.3   Influence of substrate position: rf vs floating potential

The study of film formation realized at the different conditions of the ion bombardment reveals some useful information about the role of the ions in the deposition mechanism. The simple way to carry out a deposition under such conditions is the positioning of substrates at the floating and

rf potentials. The ions accelerated by a large self bias potential to the substrate on the rf electrode have one order of magnitude higher energy comparing to the ions impinging onto the surface at the floating potential. Applied novel FTIR technique allows one to analyse molecular structure of the thin films formed on the fibre surface under the floating potential in bulk plasma. The samples grown on the rf electrode are analysed by IRRAS technique.

The plasma-on time corresponds to different steps of plasma-chemical conversion of the monomer in discharge, see Figures 33, 34. There is a definitive content of stable gaseous at every stage of the monomer conversion at the chosen process conditions. The next issue of interest is the evolution of the molecular structure of plasma polymer films in connection with the monomer conversion.

The deposition experiments were carried out in the pure HMDSO plasma and HMDSO/O_2 gas mixture under the floating and rf potentials at the following process conditions:

− pure HMDSO plasma: 15 Pa, 130 *W*, 5 *sccm* HMDSO,
− HMDSO/O_2 plasma: 15 Pa, 130 *W*, 3 *sccm* HMDSO, 17 *sccm* O_2.

The IR absorption spectra of the film deposited on the fibre were accumulated in the same way described previously.
The figures 48 and 49 present absorption spectra of films deposited in the HMDSO and HMDSO/O_2 plasmas under floating and rf potentials. The general assignment of the absorption lines from the molecular groups of interest is summarized in Table 8. The complete accumulated spectra and the line positions of absorption bands obtained in the pure HMDSO and HMDSO/O_2 plasmas under floating and rf potentials at different plasma-on times are presented in Appendices C and D respectively. The variation parameter is the plasma pulse duration. The corresponding deposition rates are included in the figures. The relatively short total accumulation time in case of the HMDSO/O_2 plasma is caused by high deposition rates.

The deposition rates of the PP HMDSO films in the pure HMDSO plasma on the fibre surface are relatively low. However, a small variation of plasma-chemical conversion of the monomer results in remarkable change of the spectrum. The intensities of the absorption lines due to vibrations of an Si-O bond in siloxane groups and methyl vibrations in methylsilane groups decrease with plasma pulse duration. This is explained by the formation of denser films.

High molecular species formed at low fragmentation grades compose a monomer-like structure of

Spectral range, cm^{-1}	Assignment
$2980 - 2850$	CH_3, CH_2
1260	$Si(CH_3)$
$1200 - 1000$	SiO_x, $SiOSi$
$900 - 750$	CH_3, CH_2

Table 8. The general assignment of the infrared absorption bands to
the molecular groups of interest in plasma polymerized HMDSO films.

plasma polymer with relative high content of the $-(CH_3)$ groups. Free internal rotation about an Si-O bond in the siloxane group thereby is sustained in such films what results in the higher extinction coefficient and, hence, in the stronger absorption of the appropriate bands ($1100 - 1000$ cm^{-1}) in the spectra of films synthesized at shorter plasma pulses.

Symmetric deformation vibrations of methyl groups in Si-$(CH_3)_3$ cause asymmetric broad band around 1256 cm^{-1} which consists of two components of unequal intensity. The presence of this group indicates a low fragmentation grade of the monomer in the plasma bulk at short plasma pulses.

The oxygen admixture accelerates drastically the deposition of plasma polymer film on the fibre surface, see Figures 48(a) and 48(b). It is caused mainly by surface activation by oxygen radicals and ions as well as by shorter times of the monomer conversion, see Figure 40.

Molecular structure of the films deposited at the very short plasma pulses, ≤ 1 s, is like that one of the films obtained in the pure HMDSO plasma, see Figure 48. The increment of the plasma pulse duration leads to the formation of films with lower organic constituent due to stronger monomer fragmentation in the plasma and more intensive oxidation of the surface. Such a change in molecular structure causes a shift of the absorption line by Si-O-Si vibration to longer wavelengths. Despite the absorption in the region of $1020 - 1010$ cm^{-1} is associated with cyclic siloxane trimers, the presence of them in plasma polymerized HMDSO films is excluded. Wrobel et al. analysed the structure of plasma polymerized siloxanes by means of pyrolysis/gas chromotography and mass spectrometry [106, 139] and found that plasma polymerization of linear siloxanes yields only linear oligomers in the volatile fraction, cyclic structures can be formed only as a result of the plasma polymerization of the cyclic siloxanes. The bivalence of oxygen atom in siloxanes do not provide a possibility for branching, crosslinking, substitution and cycling of growing plasma polymer. All these are possible only through Si or C atoms. Despite of the high organic content due to low monomer fragmentation the plasma polymer grown on the fibre does not contain disilymethylene, Si-CH_2-Si, and disilyethylene, Si-CH_2-CH_2-Si, groups which have been detected in the deposites formed on the electrodes [106, 161]. The band due to their wagging vibrations at 1030 cm^{-1} laps over the Si-O-Si band and does not permit to identify the presence of the corresponding groups. However, the absorption line at the 1350 cm^{-1} due to -CH_2- scissoring vibrations is absent in the spectra of the PP HMDSO films. The absorption of methyl groups, $2900 - 2800$ cm^{-1}, is low.

The growth of plasma polymer under the rf potential is unlike that one of the films deposited under the floating potential due to ion bombardment of substrate and growing film on the rf electrode. The active centres are formed on the surface due to the influence of energetic ions on the surface. The propagation reactions of plasma polymer chains go through these active centres. The interaction of energetic ions with growing chains of plasma polymer film results in the surface radicals which are formed on the surface contrary to those incorporated from the gas phase. There is non-linear dependence of the deposition rate on the plasma pulse duration. Plasma etching reduces the rate of the film growth. The etching becomes intensive in the HMDSO/O_2 plasma in case of the long plasma pulse durations.
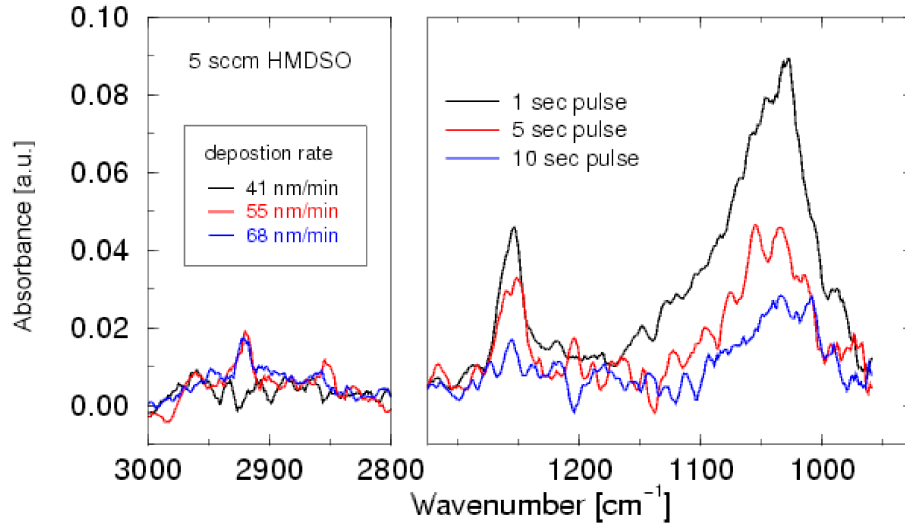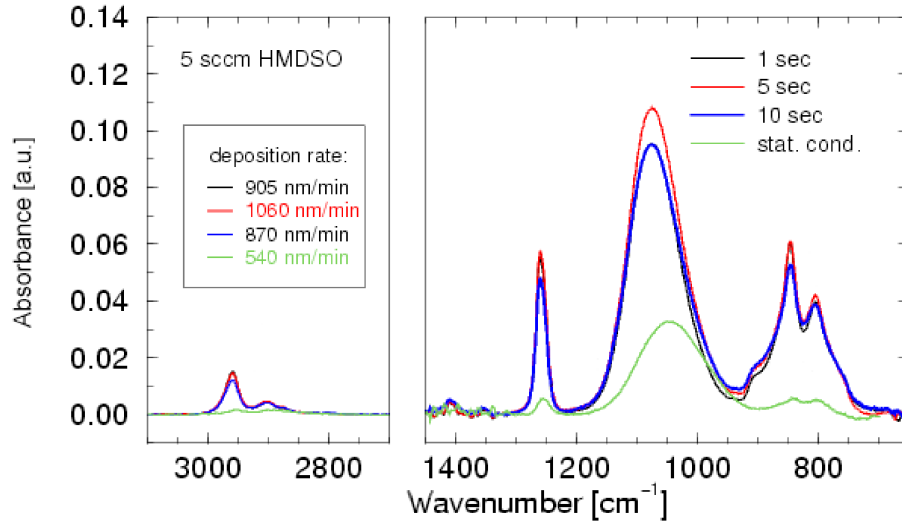
(a)
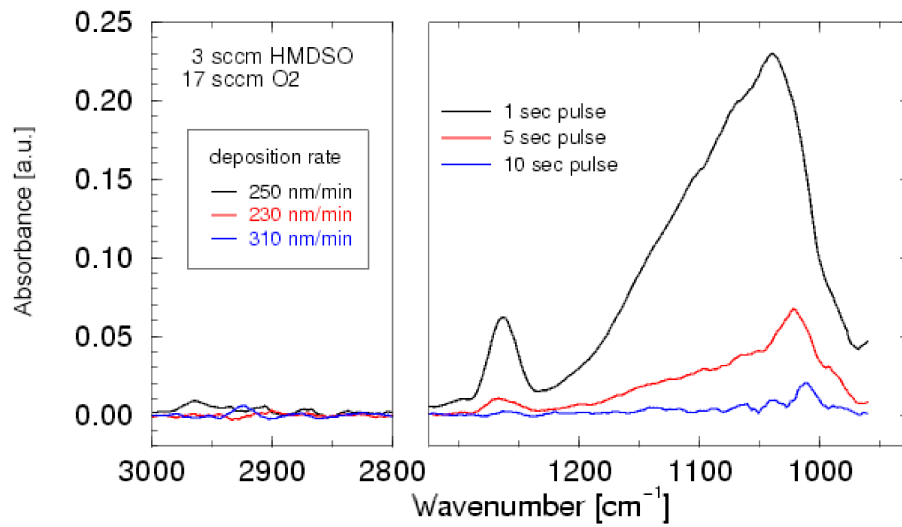
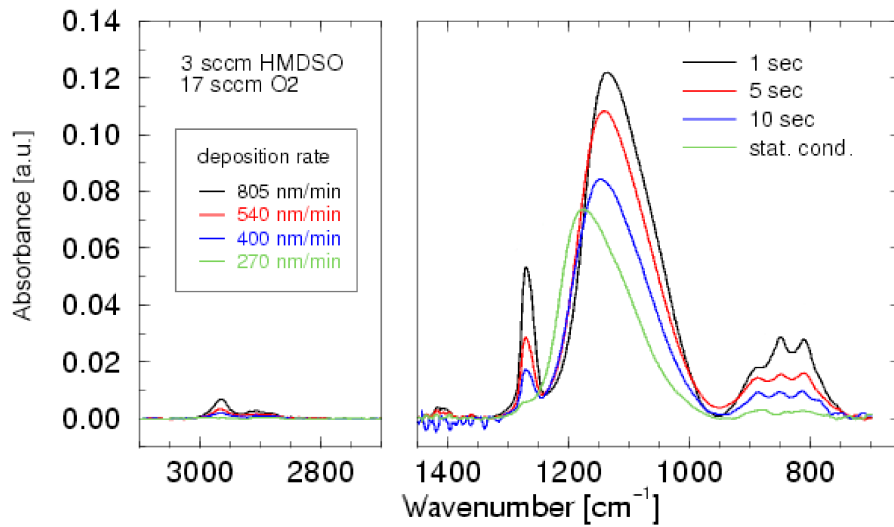
(b)

Figure 48. The FTIR absorption spectra of the films deposited on the fibre at the floating potential:
(a) in the HMDSO plasma; (b) in the HMDSO/O_2 plasma.
The absorption lines in the range $2980 - 2850$ cm^{-1} are ascribed to CH_3 groups;
1260 cm^{-1} - $Si(CH_3)$; $1200 - 1000$ cm^{-1} - SiO_x and Si-O-Si groups.

Figure 49. The FTIR absorption spectra of the films deposited on the rf electrode:
(a) in the HMDSO plasma; (b) in the HMDSO/O_2 plasma.
The absorption lines in the range $2980 - 2850$ cm^{-1} are ascribed to CH_3 and CH_2 groups;
1260 cm^{-1} - $Si(CH_3)$; $1200 - 1000$ cm^{-1} - SiO_x and Si-O-Si groups;
$900 - 750$ cm^{-1} - CH_3 and CH_2 groups.

Di	Tri	Tetra	Penta	Hexa	Hepta	Octa
		Open chain polymers				
	1076 (m)	1080 (s)	1086 (s)	1088 (s)	1092 (s)	1093 (s)
			1064 (m)	1056 (m)	1049 (w)	1045 (w)
1056 (s)	1046 (s)	1038 (s)	1033 (s)	1029 (s)	1027 (s)	1024 (s)
		Branched polymers				
	Isotetra				Neopenta	
	[3-(Trimethylsiloxy)-heptamethyltrisiloxane]				[3,3-Di-(trimethylsiloxy)-hexamethyltrisiloxane]	
	1104 (w); 1056 (s)				1068 (s)	

Table 9. The wavelengths (in cm^{-1}) of the infrared absorption bands due to Si-O vibration in various methylpolysiloxanes. The number of siloxane groups is shown in the column heads. The line intensity: (s) - strong, (m) - medium, (w) - weak. (adapted from [157]).

The following features of the IR spectra of plasma polymer films formed on the rf electrode are observed, see Figure 49(a). The absorption line due to Si-O stretching vibration do not have an explicit asymmetric form with main peak at the 1070 cm^{-1} and the shoulder at the 1037 cm^{-1}. There is a wide absorption line which lies in the range of $1072 - 1043$ cm^{-1}, see Figures 48 (a) and 49(a). The line position depends on the molecular group containing Si-O bond. Linear small-chain siloxanes tend to absorb at about 1050 cm^{-1} (HMDSO - at 1060 cm^{-1}). This line broadens gradually with increase in molecular weight: long-chain polymers have a broad, strong band with maxima at 1085 cm^{-1} and 1025 cm^{-1} [97, p. 192], see also Table 9.

The position of the line centre is shifted from 1072 cm^{-1} to 1043 cm^{-1} with the plasma pulse duration while the FWHH increases. These alterations in the IR absorption spectrum are explained by film density, molecular environment of siloxane group and crosslinking structure. The film deposited at the longer plasma pulse duration have a higher mass densities and more cross-linked structure. The molecular structure is formed mainly from the species of monomer-like structure $(CH_3)_{x=1\div3}-Si-O-Si-(CH_3)_{y=1\div3}$. Thus, the analysed films can be considered as a type of methylpolysiloxane.

The atomic composition of chosen samples was analysed by XPS, see Table 10. The XPS analysis of the chosen samples confirm the results of the FTIR spectroscopy. The oxygen dilution of the monomer results in the formation of the thin films with lower content of organic constituent. The influence of substrate position on the film composition is not so strong. The films deposited on the powered electrode have higher content of oxygen than that of carbon both in HMDSO and HMDSO/O_2 plasmas.

plasma pulse duration, [s]	HMDSO						HMDSO/O2					
	floating potential			rf potential			floating potential			rf potential		
	Si	O	C, [%]	Si	O	C, [%]	Si	O	C, [%]	Si	O	C, [%]
1	25	24	51	24	29	47	20	43	37	21	47	32
10	22	24	54				22	50	28			
240				24	31	45				22	58	20

Table 10. Elemental composition of plasma polymerized films by XPS analysis.

6.5   Physical properties of plasma deposited films

6.5.1   Optical properties

Optical propeties of the HMDSO plasma deposited films have been intensively investigated for a long time by many authors [10, 152, 119]. Here the optical constants were measured for the plasma polymerized HMDSO films deposited at the different energy inputs. The grade of the monomer fragmentation results in the deposition of the films of various molecular structure and density and, hence, of different optical properties.

The analysis of structure-property correlations for refractive index in terms of the connectivity indices [104] shows that the enhancement of refractive index is due to the increase of densities of Si-O, C-O, Si-H, C=O, Si-Si groups in polymers. Moreover, highly cross-linked structure should have the same influence on the refractive index. The experimental results obtained by Poll et al [152] confirm this correlation except the influence of the Si-Si group. Aumaille et al [119] found that the refractive index is a linear function of the density of the Si-H bonds.

The results of mass spectrometric measurements described above and literature data allow one to predict the trend in the value of refractive index in dependence on the energy input. The deposition at high energy input conditions leads to the formation of the films with considerable content of the Si-O, Si-H bonding [152], and hence, the films with higher values of the refractive index.

The films were deposited on Si wafers under the process conditions corresponding to low (PP HMDSO I) and high energy inputs (PP HMDSO II) with a nearly equal thickness of about 30 nm. The samples were analysed by means of spectroscopic ellipsometry. The measured ellipsometric angles, Ψ and Δ, were processed with the use of the Sellmeier dispersion model without absorption on the basis of the 2-layer optical model. The dispersion relations of the plasma deposited HMDSO films are shown in Figure 50. The values of the refractive index for both films are higher than that one of the monomer (1.377 at the 589 nm at 20^oC). There is a relatively slight dispersion relation in the spectral range.

The IR spectrum of the PP HMDSO II demonstrates a lower absorption in general comparing to the PP HMDSO I film because of the higher mass density. The film density seems to be the main factor in the difference of the absolute values of refractive indices here. Although there is also a contribution of the Si-O and Si-H groups. The influence of the Si-Si bonds (absorption line at nearly 400 cm^{-1} [5]) seems to be negligible because the detection of such bonds have not been reported for any HMDSO deposition process in literature.
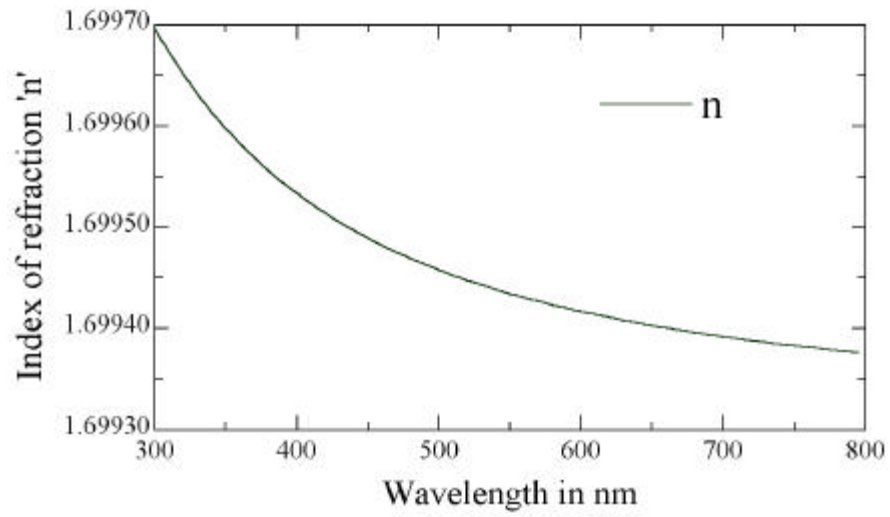
(a)
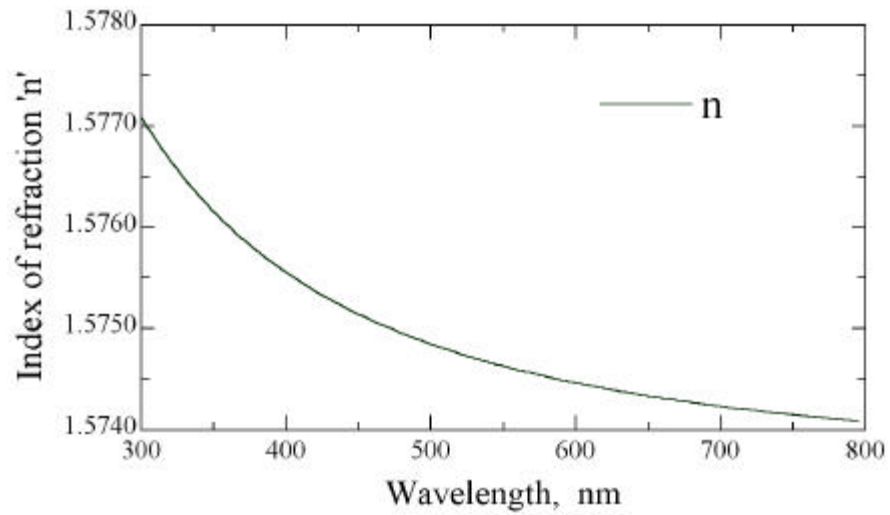
(b)

Figure 50. Dispersion relation of the HMDSO plasma deposited films. Process conditions:
(a) 10 *Pa*, 10 *W*, 8 *sccm* HMDSO; (b) 10 *Pa*, 60 *W*, 2 *sccm* HMDSO.
The fitting was done with minimal square error of about 3.

6.5.2   Surface morphology

The characterization of deposited plasma polymers by atomic force microscopy showed that the surface of the films deposited on Si wafers is very smooth, the roughness is about of 10 nm rms (root-mean-square). Contrary, the samples deposited on non-smooth substrates are characterized by spherical or hemispherical microstructures which can be observed by Secondary Electron Microscopy (SEM). Similar surface morphology has been observed earlier for plasma polymers of the various monomers, e.g. by Haraguchi [162] and by Huber [163]. The analysis of the obtained SEM micrographs allows one to draw the following tendency: the larger pore size of substrate, the higher surface roughness of plasma polymer. Besides Si wafers polymer films of various porosity were used as a substrate material: cellulose acetate (CA) membranes (ultrafiltration membranes, 500 MW cut-off, YC05, Millipore) and polyamide 6,6 membranes (microfiltration membranes, 100 μm pore size, Pall Gelman Sciences). The value of 500 MW cut-off corresponds to the pore size of about 0.5 nm [150]. One can see that plasma polymers on cellulose acetate membranes have smoother and more closed surface in comparison with that of the films on polyamide membranes. Nevertheless, the films produced at the chosen conditions do not have a closed plasma polymer for both substrate materials.

Below are some micrographs of the surfaces of plasma polymers deposited on different substrates, see Figures $51 - 53$. The images of various magnifications are presented also in Appendix E. The formation of such hemispherical microstructures can be explained of non-homogeneous growth of plasma polymer on non-smooth substrate. The second speculative mechanism is assumed the local inhomogeneity of the electric field. Various experiments have shown that electrons incident on the surface of substrate or growing plasma polymer get attached to it. Because of the roughness the electric field produced by the negatively charged surface is not homogeneous. The stronger field around convexities causes the more intensive ion flux what in turn results in the higher rate of the deposition in this region than that around cavities. The macroparticles formed in the gas phase (oligomers, plasma polymer powder) were not observed in the plasma, that is why, their influence on the formation of the hemispherical microstructures is excluded.

These microstructures can be clearly observed by atomic force microscopy, see Figure 54. The plasma polymerized HMDSO film was deposited on the substrate from polyamide 6.6 at the conditions of low energy input (20 W discharge power, 20 Pa total pressure, 4 $sccm$ HMDSO). The spherical microstructures have the sizes of about $300 - 600$ nm.
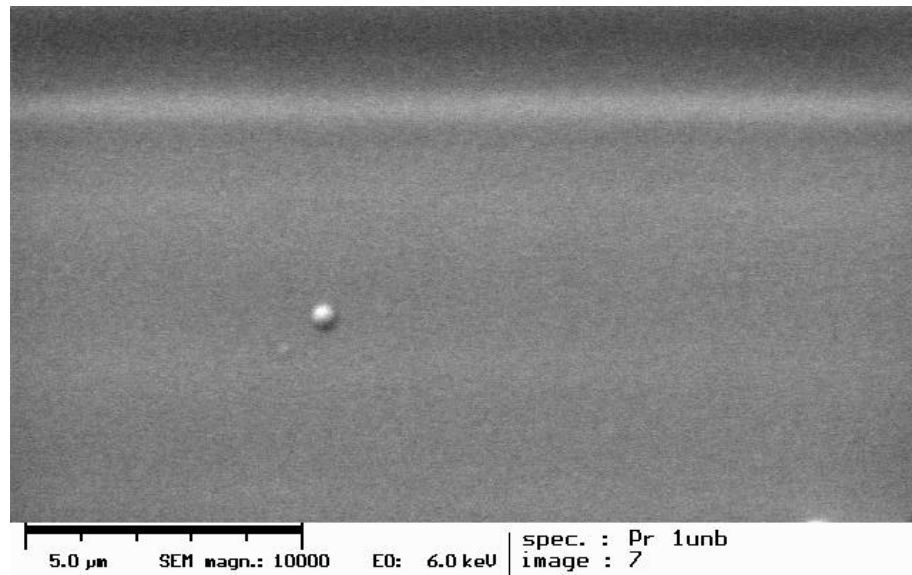
(a)
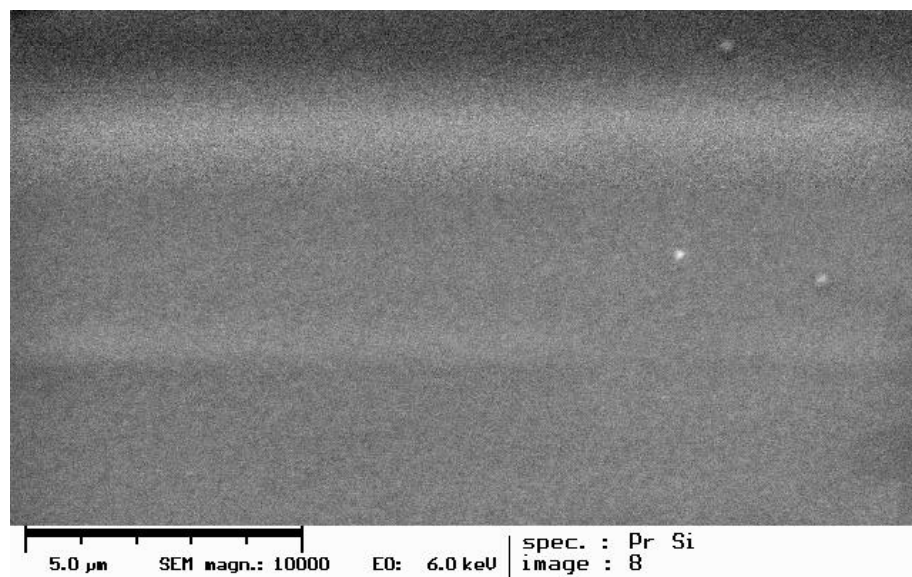
(b)

Figure 51. (a) SEM micrograph of Si substrate without plasma polymer,
(b) SEM micrograph of Si substrate with the HMDSO plasma polymer deposited
at the process conditions: 10 Pa, 60 *W*, 2 *sccm* HMDSO.
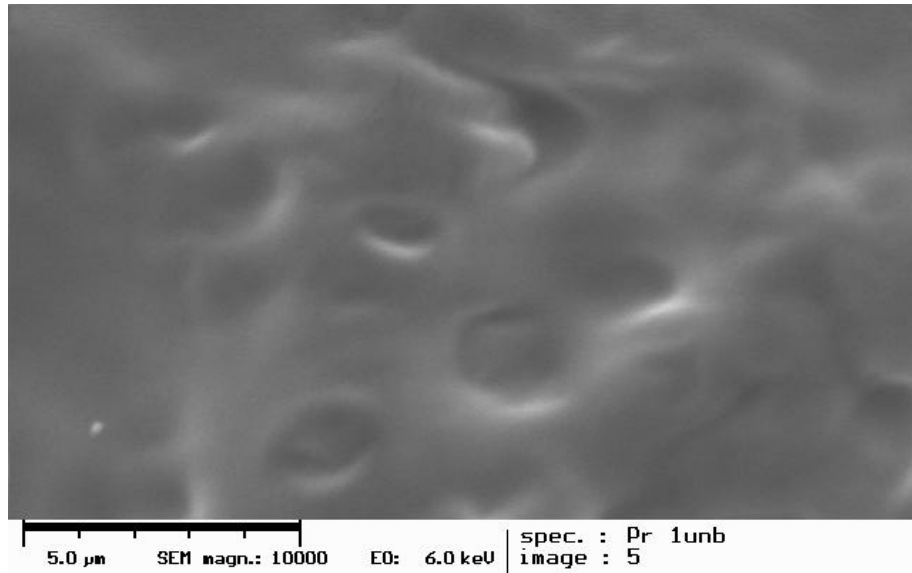
(a)
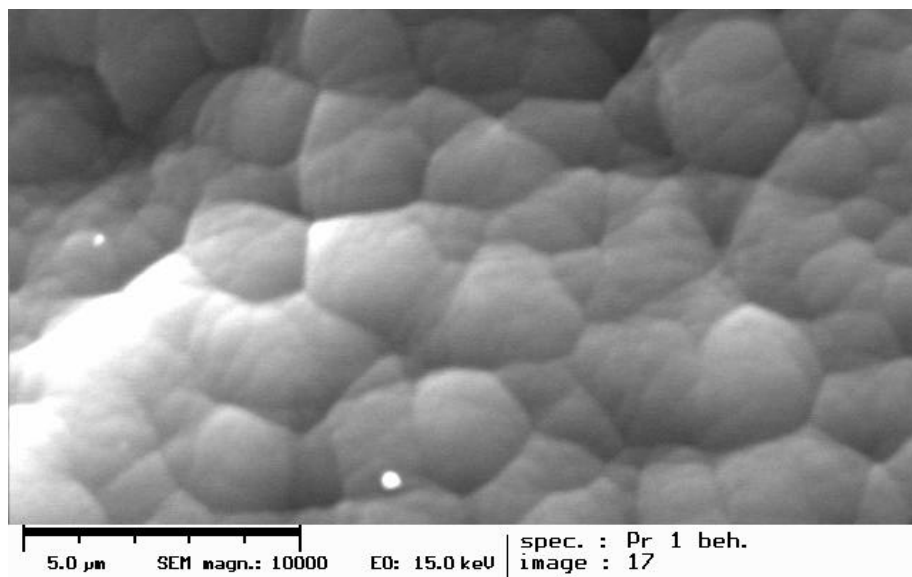
(b)

Figure 52. (a) SEM micrograph of cellulose acetate membrane without plasma polymer,
        (b) SEM micrograph of cellulose acetate membrane with the HMDSO plasma polymer
        deposited at the process conditions: 10 Pa, 60 *W*, 2 *sccm* HMDSO.

(a)

(b)

Figure 53. (a) SEM micrograph of polyamide 6,6 film without plasma polymer,
(b) SEM micrograph of polymide 6,6 film with the HMDSO plasma polymer
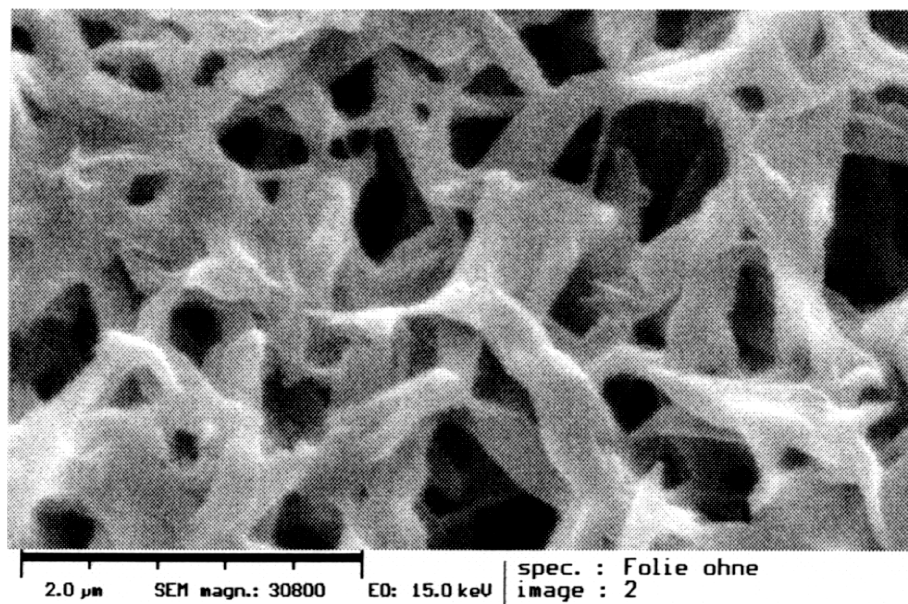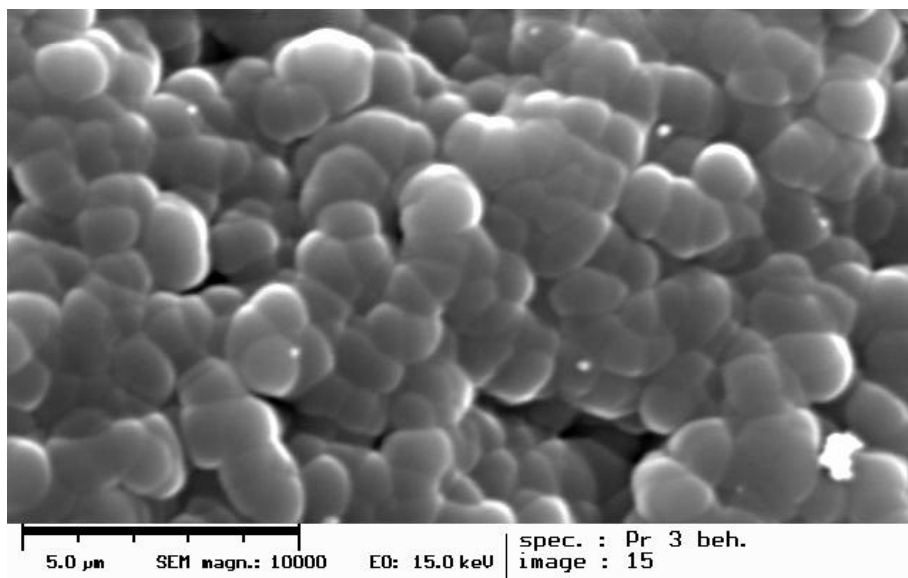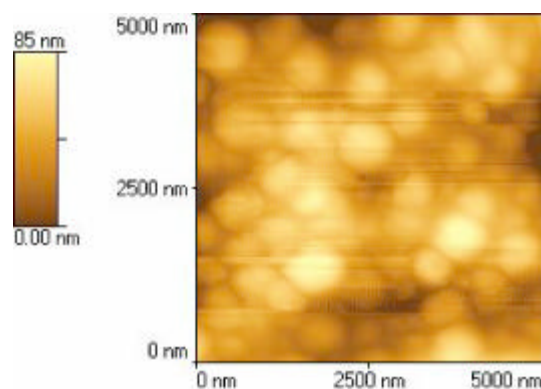deposited at the process conditions: 10 Pa, 60 W, 2 *sccm* HMDSO.

Figure 54. Spherical microstructures observed on the surface os plasma polymerized HMDSO film by atomic force microscopy. Plasma polymer film was deposited on the substrate from polyamide 6.6 at the process conditions: 20 Pa, 20 *W*, 4 *sccm* HMDSO.

6.5.3 Gas permeation

Membrane-based gas separation technique has been developing very intensively during last decades. This field is believed to be the one of the main areas of growth for the membrane technology [52]. For a commercial applicability the membrane must exhibit both high permeability to the desired gas (or the component of a gas mixture) and high level of selectivity (or separation factor). The first demand requires the polymer films to be sufficiently thin, the second one requires specific structure and composition of an active layer to provide desired selective properties.

Several authors have reported successful application of plasma polymerization for the preparation of gas separating membranes $[164 - 169]$. These composite membranes were studied for several gas separation applications (O_2/N_2, CO_2/CH_4, H_2/N_2, He/N_2). Plasma polymers were deposited from various organic compounds, including silicon-, halogen-containing monomers, on different substrates (polymeric as well as porous metal). The choice of the Si-containing monomer is based on the fact that the membranes produced from such compounds by conventional chemical methods demonstrate a high level of gas permeability because of the high mobility of the siloxane bonds. The aim of this part is to study the gas separating properties of the composite membranes with plasma polymerized HMDSO. N_2-, He- and O_2-permeation was measured.

Gas separating properties of membranes with PP HMDSO
As it was shown above the deposition at the high energy input conditions results in the films of high density with relatively low content of siloxane groups which is responsible for a high gas permeability of chemical polysiloxanes. Thus, one should expect the decrease of gas permeability respectively to all tested gases for the composite membranes with PP HMDSO deposited at such process conditions.

The results of the gas permeability measurements are summarized in Table 11. The permeability coefficients for a composite membrane on various gases are presented under appropriate preparation conditions.

Composite membranes prepared on CA substrates show lower permeability to the tested gases than those on the polyamide substrates. The gas transport occurs via two mechanisms: Knudsen flow and the diffusion-solution mechanism. As it was mentioned earlier, the latter defines the permeability coefficient in the following way: $Perm = D \cdot \sigma$, where D and σ are diffusion and solution coefficients respectively [50 − 52]. Plasma polymers deposited on CA substrates at the high energy input conditions differ in their properties not only from films polymerized on polyamide 6,6 substrates but also from ones synthesized in the other regime. It concerns mainly the N_2/O_2 separation. One can notice that the permeability of oxygen is greater than that one of nitrogen. This can be explained by a higher solubility of oxygen in plasma polymer. As for He/N_2 pair there is no changes of the trend in dependence on the substrate material (and accordingly pore size): the selectivity increases with a decrease of the pore size. It can also mean that membrane prepared at the high energy input conditions on CA substrates have more closed surface structure in comparison with the other membranes.

The obtained results are in a good agreement with measurements on plasma polymerized octamethyltrisiloxane from Matsuyama et al [64]. As the parameter W/fM (ϕ here) decreases the permeability increases, while the selectivity is not remarkably affected. Such a dependence can be explained by the fact that the content of siloxane groups in plasma polymer gets higher at low ϕ. The fragmentation in plasma is weak in this case. Sakata et al. [164] constructed oxygen enricher by polymerizing the HMDSO monomer on a bundle of hollow fibers with a length of about 23 cm. The selectivity for O_2/N_2 was 2.8 when the oxygen permeability was 3.4×10^{-7} $cm^3/(cm^2 \cdot s \cdot cmHg)$. This corresponds to 1.7×10^{-11} $cm^3 \cdot cm/(cm^2 \cdot s \cdot cmHg)$ for a flat 500 nm thick membrane what is significantly lower than permeabilities of membranes presented here.

conditions of low energy input	conditions of high energy input
10 Pa, 10 W, 8 $sccm$ HMDSO	10 Pa, 60 W, 2 $sccm$ HMDSO
PP HMDSO + Polyamide 6,6	
Permeability coefficients	
He 1048×10^{-7}	1036×10^{-7}
N_2 542×10^{-7}	518×10^{-7}
O_2 515×10^{-7}	506×10^{-7}
Ideal selectivity	
α(He/N_2) 1.9	2
α(O_2/N_2) 0.95	0.98
PP HMDSO + Cellulose Acetate	
Permeability coefficients	
He 14.1×10^{-7}	5.3×10^{-7}
N_2 6.5×10^{-7}	1.4×10^{-7}
O_2 5.9×10^{-7}	2.2×10^{-7}
Ideal selectivity	
α(He/N_2) 2.2	3.8
α(O_2/N_2) 0.91	1.6

Table 11. Gas permeability and ideal selectivity of the composite membranes with plasma polymerized HMDSO. Permeability coefficient, $cm^3 \cdot cm/(cm^2 \cdot s \cdot cmHg)$.

Huber et al. [163] polymerized membranes from hexafluoroethane/hydrogen mixtures. The maximum selectivity was approximately 3.4 when the oxygen permeability was 2.1×10^{-9} $cm^3 \cdot cm/(cm^2 \cdot s \cdot cmHg)$. Gas separating properties of conventional Si-containing membranes and those of a composite membrane with plasma polymer from HMDSO (this work) are given in Table 12.

The PP HMDSO membrane has comparable data on permeability with those of the others. Its selectivity, however, is higher for (He/N_2) pair and is lower for (O_2/N_2) pair. The PVTMS membrane has better selectivity, but considerably lower permeability coefficients in comparison with the composite membrane.

	PVTMS	PTMSP	PDMS	PP HMDSO + CA
P (He) Ba	160	5100	350	5339
P (N_2) Ba	11	2000	280	1405
P (O_2) Ba	44	4000	600	2248
$\alpha(O_2/N_2)$	4	2	2.1	1.6
$\alpha(He/N_2)$	14.5	2.6	1.3	3.8

PVTMS - Poly (vinyltrimethylsilane)

PTMSP - Poly (1-trimethylsilyl-1-propyne)

PDMS - Polydimethylsiloxane

PP HMDSO + CA - composite membrane with plasma polymerized HMDSO
        prepared at the high energy input conditions, see the Table 1.

Ba - Barrer, 1 Ba $= 10^{-10}$ $cm^3 \cdot cm/(cm^2 \cdot s \cdot cmHg)$

Table 12. Comparison of the gas separating characteristics of commercial membranes and composite membranes with PP HMDSO.

Summary

The thin film deposition in the HMDSO-containing plasmas of capacitively coupled rf discharge was investigated by methods of thin film characterization and gas phase analysis. The main subject of attention was the characterization of thin organic films, to be more specific, the formation of molecular structure and the film growth. For the investigation of these issues a novel fibre based FTIR diagnostic tool was developed which allows *in situ* time resolved measurements with low disturbance of plasma. Evanescent wave spectroscopy is the base of this technique applied for a diagnostics of reactive plasmas for the first time. The essence of the tool is an IR fibre served as a sensing element. The technique was tested on the well known process of styrene plasma polymerization.

The high complexity of plasma processing of thin films lays specific requirements on the diagnostic techniques. In order to understand the mechanisms of plasma-surface interaction one needs the information about the evolution of molecular structure of deposited or treated polymer films. *In situ* analysis of molecular structure of growing film also allows a real time control of the process. Moreover, samples would not be influenced by oxidation due to exposure to the ambient atmosphere. One of the aims of this work consisted in the development of novel FTIR diagnostic tool which makes *in situ* detection of molecular groups of growing plasma polymer possible. Evanescent wave spectroscopy was chosen as the base of the novel technique. Analysis of the theory of evanescent wave spectroscopy as well as fibre optics shows that suggested technique can be used for FTIR spectroscopy on thin films and, moreover, allows one to mark out the main parameters determining sensitivity of the technique. The number of total internal reflections is one of them. The technique can be modified through the thinning of the sensing part of the fibre what enhances the method's sensitivity. Undertaken simulation of the propagation of the IR radiation through a fibre provided the grade of the optimal thinning for the chosen experimental conditions. The results of the measurements by tapered IR fibre in the liquid hexamethyldisiloxane (HMDSO) monomer showed the signal amplification by factor of about 3 which is in accordance with that of the simulation. Chalcogenide (As-Se-Te) fibres meet the requirements of spectroscopic measurement and plasma experiment. These fibres are transparent in the wide mid-IR spectral range $(1 - 12 \ \mu m)$, UV and chemically stable. They possess a high index of refraction ($n_{core} = 2.82$). The chalcogenide glass can be drawn into very tiny fibres (up to 50 μm in diameter) what results in the very low disturbance of plasma, particularly in comparison with typical internal reflection elements which have been used for the surface diagnostics of plasma deposition by attenuated total reflection spectroscopy.

The developed diagnostic tool was approved on the well known process of styrene plasma polymerization. The main results of the study are:

— fibre based FTIR spectroscopic technique can be used for *in situ* investigation of thin organic film deposition in plasma as well as plasma treatment of conventional polymers;
— the use of the IR fibre provides higher sensitivity than that of the internal reflection element of the same length;
— the least detectable thickness is determined by fibre preparation and geometry and extinction coefficient of molecular group; e.g. the signal from deformation aromatic C-H vibrations can be recognized at the 7 nm thickness of plasma polymerized styrene film;
— film growth is inhomogeneous: a $5-6$ nm thick interface layer was observed between fibre core and cross-linked bulk plasma polymer;
— for the first time the short-range domains of different molecular orientations (tacticities) were found in plasma polymers;
— the structure-property correlation describing the relation between aromaticity and gap energy as well as refraction index is confirmed: the gap energy and the index of refraction increase with the decrease of aromaticity;
— O_2-plasma etching of plasma polymerized styrene performed with the aim of the fibre regeneration resulted in the formation of various carbonyl groups at the beginning of the treatment.

The second part of this work is devoted to the investigation of the film deposition in the discharge plasmas containing hexamethyldisiloxane which is one of the most utilized organosilicon compounds used for such an application.
Investigation of film deposition in the HMDSO and HMDSO/O_2 plasmas of capacitively coupled rf discharge includes both analyses of structure formation and of gas phase processes. The study covers the film formation under different conditions of ion bombardment, on the substrates at rf and floating potential, and at various stages of monomer conversion. The influence of the process parameters (total pressure $10-200$ Pa, power $10-200$ W, gas flow rate $1-10$ $sccm$) on rate of the monomer conversion and deposition rate could be summarized in terms of a composite process parameter analogous to that introduced by Yasuda.

After the discharge ignition, the HMDSO molecules are converted into active species (radicals, ions, etc) which are the precursors for the growing film and the stable gaseous products. The monomer molecules are mainly decomposed through the cleavage of methyl groups and dissociation of Si-O bond. Methyl radicals and ions serve as the source of stable gaseous hydrocarbon species. For the first time the absolute concentrations of methyl radicals and stable hydrocarbon molecules (CH_4, C_2H_2, C_2H_6) were measured in the HMDSO-containing plasmas by IR tuneable diode laser absorption spectroscopy. The detection of hydrocarbons by IR TDLAS and mass spectrometry reveals the high content of these species. At high values of composite process parameter ($> 10^{12} Jkg^{-1}$), when the deposition rate achieves the maximum value, the partial concentration of ethane is nearly 0.3 of the total particle quantity at the pressure of 15 Pa, the partial concentration of methane $-$ 0.1 and the partial concentration of molecular hydrogen $-$ nearly 0.5.

The film formation at different stages of the monomer conversion was studied with the use of pulsed

mode operation of rf discharge. Low grade of the monomer fragmentation at short plasma pulses ($\leq 1s$) results in a monomer-like, i.e. with the high content of organic constituent, molecular structure of the films deposited both at the floating and rf potentials. The intensive monomer fragmentation at long plasma ignition times results in the enhanced formation of low molecular species (hydrocarbons, molecular hydrogen) in the gas phase and growth of dense films with lower content of organic constituent. The rate of the film deposition at the floating potential increases with the plasma ignition time. The plasma etching due to intensive ion bombardment causes the decrease of the rate of film deposition on rf electrode with the plasma-on time.

These trends of deposition kinetics are also kept in case of the HMDSO/O$_2$ plasma although the O$_2$ admixture has a drastic influence on the film formation. The monomer fragmentation is accelerated, the rate of deposition at the floating potential increases, e.g. 55 nm/min in HMDSO plasma vs 230 nm/min in HMDSO/O$_2$ plasma. At the same time the deposition rate at rf potential in the HMDSO/O$_2$ plasma, e.g. 540 nm/min, is lower than that in the pure HMDSO plasma, e.g. 1060 nm/min, mainly, due to etching and oxidation processes. The latter contributes also to the formation of SiO$_x$-like molecular structure of the films.

The variation of different process parameters (total pressure, power, monomer flow rate) results in nearly the same dependency of the deposition rate on the composite parameter. The deposition kinetics at the different conditions of ion bombardment allows one to conclude that the control of the deposition process is brought into effect by ions due to surface activation and/or initiation of the growth reactions on the surface. A simple model based on a concept of the effective electric field was developed for analysis of the influence of the main process parameters on the deposition rate. The model allows to fit obtained experimental dependencies of the deposition rate on the pressure and the energy input expressed by the composite parameter. The value of electron density derived from the fitting was found to be nearly $10^9 cm^{-3}$ which is comparable with typical electron density values in rf plasmas of molecular gases.

The physical properties of the $30-500$ nm thick films deposited in the HMDSO plasmas were studied according to the optical properties, the film surface morphology and the permeation of N$_2$, O$_2$ and He gases. The refractive index of plasma polymerized HMDSO films increases with the energy input in the discharge. The surface morphology of films is dependant on the state of the substrate surface. The plasma polymers deposited on Si wafers have a smooth surface. The rough porous surface of substrate ensues the formation of non-closed films with hemispherical microstructures. Such a morphology results in high gas permeability of composite membranes with the HMDSO plasma polymerized films.

Undertaken study clears up some issue of the film formation in the HMDSO-containing plasmas. However, the following matters can be stated for study in the future works:

— detection of film precursors (SiO$_x$, SiOSi, C$_x$H$_y$SiO) and determination their contributions to the deposition kinetics;
— formation of the precursors in gas phase;
— influence of UV radiation from plasma on the film growth;
— determination of plasma parameters (n_e, T$_e$, etc)

FTIR diagnostic tool, developed in this work, should be modified further in order to minimize the plasma disturbance and to optimize the maintenance of the tool. A fibre probe is one of the possible solution. The following problems should be overcome
:
— fabrication of reflecting coating on the endface for re-directing of the propagating in
   the fibre core IR radiation;
— separation of input and output IR beams;
— improvement of fibre glass properties (e.g. enhancement of glass transition temperature).

References

[1] Yasuda H 1985 *Plasma Polymerization* (Orlando: Academic Press)

[2] Polak L S and Lebedev Yu A 1998 *Plasma Chemistry* (Cambridge: Cambridge International Science Publishing) p 266 - 311

[3] Schlemm H 1987 *Neutralgasreaktionskinetik in Gasentladungen* (Chemnitz: Technische Universität Chemnitz)

[4] Nitschke M 1995 *PhD thesis* (Chemnitz, Germany: Technical University of Chemnitz)

[5] Hollenstein Ch 1998 *Plasma and Polymers* **3** (4) p 249 - 256

[6] Magni D, Deschenaux Ch, Hollenstein Ch, Creatore A and Fayet P 2001 *Journal of Physics D: Applied Physics* **34** p 87 - 94

[7] Pan Y V, Barrios E Z and Denton D D 1996 *Applied Physics Letters* **68** (24) p 3386 - 3388

[8] Ishikawa K and Sekine M 2000 *Japanese Journal of Applied Physics* **39** (12B) p 6990 - 6995

[9] van Hest M F A M, Klaver A and van de Sanden M C M 2001 *A new and fast in situ spectroscopic IR absorption measurement technique* in Proceedings of 15th International Symposium on Plasma Chemistry ed Bouchoule A, Pouvesle J M, Thomann A L, Bauchire J M and Robert E (Orleans: GREMI, CNRS/University of Orleans) **VII** p 2282 - 2286

[10] Poll H U, Arzt M, Blaschta F, Friedrich M, Kreißig E, Meichsner J and Rochotzki R 1993 *Optische Eigenschaften von Plasmapolymerschichten* Schlussbericht (Chemnitz: TU Chemnitz)

[11] Martinu L and Poitras D 2000 *Journal of Vacuum Science and Technology* **A18** (6) p 2619 - 2645

[12] Matsuyama H, Shiraishi T and Teramoto M 1994 *Journal of Applied Polymer Science* **54** p 1665 - 1672

[13] Agres L, Segui Y, Delsol R and Raynaud P 1996 *Journal of Applied Polymer Science* **61** p 2015 - 2022

[14] Görbig O, Nehlsen S and Müller J 1998 *Journal of Membrane Science* **138** p 115 - 121

[15] Segui Y and Bui Ai 1978 *Thin Solid Films* **50** p 321 - 324

[16] Sadhir R K and Sanpana Z N 1991 *Journal of Material Science* p 4261

[17] Schreiber H P, Wertheimer M R and Wrobel A M 1980 *Thin Solid Films* **72** p 487 - 493

[18] Schwarz J, Schmidt M and Ohl A 1998 *Surface and Coating Technology* **98** p 859 - 864

[19] Wrobel A M and Wertheimer M R 1990 *Plasma-polymerized organosilicones and organometallics* in *Plasma Deposition, treatment, and etching of polymers* ed by d' Agostino R (London: Academic Press) p 163

[20] Meichsner J, Zeuner M, Krames B, Nitschke M, Rochotzki R and Barucki K 1998 *Surface and Coatings Technology* **98** p 1565 - 1571

[21] Raizer Yu P, Shneider M N and Yatsenko N A 1995 *Vysokochastotnyi emkostnyi razrjad* (Nauka: Moscow)

[22] Lieberman M A and Lichtenberg A J 1994 *Principles of Plasma Discharges and Materials Processing* (New York: John Wiley & Sons)

[23] Mechold L 2000 *PhD thesis* (Greifswald, Germany: University of Greifswald)

[24] Wai Yip Fan 1997 *Ph.D. Thesis* (University of Cambridge, UK)

[25] Yamada C, Hirota E and Kawaguchi K 1981 *Journal of chemical Physics* **75** p 5256 - 5264

[26] Wormhoudt J and McCurdy K E 1989 *Chemical Physics Letters* **156** p 47

[27] Rothman L S, Gamache R P, Tipping R H, Rinsland, C P, Smith M A H, Benner D C, Devi V M, Flaud J M, Peyret C C, Goldman A, Massie S T, Brown L R and Toth R A 1992 *Journal of Quantitative Spectroscopy and Radiative Transfer* **48** p 469 - 507

[28] Husson N, Bonnet B, Chédin A, Scott N A, Chursin A A, Golovko V F and Tyuterev Vl G 1994 *Journal of Quantitative Spectroscopy and Radiative Transfer* **52** p 425

[29] Morrison P W and Haigis J R 1993 *Journal of Vacuum Science and Technology* **A11** p 490

[30] Herzberg G 1989 *Molecular spectra and molecular structure* (Malabar, Florida: Krieger Publishing) reprint edition

[31] Steinfeld J I 1985 *Molecules and Radiation: An Introduction to Molecular Spectroscopy* (Cambridge, Massachusets: The MIT Press)

[32] Elyashevitch M A 2001 *Atomnaja i molekuljarnaja spektroskopija* (Moscow: Editorial URSS) 2-nd edition

[33] Gribov L A 1976 *Vvedenie v molekuljarnuju spektroskopiju* (Moscow: Nauka)

[34] Griffiths P R and de Haseth J A 1986 *Fourier Transform Infrared Spectrometry* (New York: John Wiley&Sons)

[35] Norton R H and Beer R 1976 *Journal of Optical society of America* **66** p 259 1977 *Erratum Journal of optical Society of America* **67** p 417

[36] Kauppinen J K, Moffatt D J, Cameron D G and Mautsch H H 1981 *Applied Optics* **20** p 1866

[37] Ramsay D A 1952 *Journal of American Chemical Society* **74** p 72

[38] Greenler R 1966 *Journal of Chemical Physics* **44** p 310

[39] Harrick N J 1967 *Internal Reflection Spectroscopy* (New York: John Wiley & Sons)

[40] Azzam R M A and Bashara N M 1999 *Ellipsometry and polarized light* (Amsterdam: Elsevier) 4^{-th} edition

[41] Fukarek W 1993 *Ellipsometrische Dickenbestimmung* in *Schichtdickenmessung* ed Hermann D (München: Oldenburg-Verlag) p 292 - 350

[42] Jellison G E 1993 *Thin Solid Films* **234** p 416 - 422

[43] Pohl R W 1967 *Optik und Atomphysik* (Berlin: Springer-Verlag)

[44] Born M 1972 *Optik* (Berlin: Springer-Verlag)

[45] Aspnes D E 1982 *Thin Solid Films* **89** p 249 - 262

[46] Tauc J 1974 *Amorphous and liquid semiconductors* (London: Plenum Press)

[47] Takeda K, Matsumoto N and Fukuchi M 1984 *Physical Review* **B 30** (N10) p 5871 - 5876

[48] Tanaka K, Kobayashi H, Koike T, Yamabe T, Osawa Y, Niwa Sh and Yasuda N 1988 *Synthetic Metals* **25** p 289 - 298

[49] Halwa H S 1997 *Handbook of Organic Conductive Molecules and Polymers*: Vol **2** *Conductive Polymers: Synthesis and Electrical Properties*

[50] Reitlinger S A 1974 *Permeability of Polymeric Materials* (Moscow: Khimia)

[51] Mulder M 1996 *Basic Principles of Membrane Technology* (Dordrecht: Kluwer Academic Publishers) 2-nd Ed

[52] Paul D R and Yampol'skii Y P 1994 *Polymeric Gas Separation Membranes* (Boca Raton: CRC Press)

[53] Barrer R M 1939 *Transactions of Faraday Society* **35** (5) p 628

[54] Buckner N and Schrickerb B 1960 *Kunststoffe* **50** (3) p 156

[55] Linowitzki V 1971 *Kunststoffe* **61** (3) p 188

[56] Snyder A W and Love J D 1983 *Optical waveguide theory* (London: Chapman and Hall)

[57] Lines M E and Klocek P 1998 *Optical Transmission Theory* in *Infrared Fiber Optics* ed Sanghera J S and Aggarwal I D (Boca Raton: CRC Press) p 1 - 30

[58] Harrick H J 1965 *Journal of the Optical Society of America* **55** (7) p 851 - 857

[59] Landau L D and Lifschitz E M 1992 *Electrodynamics of Continuous Media* Vol. **VIII** Course of Theoretical Physics (Moscow: Nauka) p 59 - 61

[60] Mirabella F M 1998 *Attenuated Total Reflection Spectroscopy* in *Modern Techniques in Applied Molecular Spectroscopy* ed Mirabella F M (New York: John Wiley & Sons) p 127 - 183

[61] Villarruel C A, Dominguez D D and Dandridge A 1987 *Fiber-Optic Sensors* II SPIE Proc **798** p 225 - 229

[62] Saggese S J, Shahriari M R and Siegel Jr G H 1988 *Infrared Optical Material* IV SPIE Proc **929** p 106 - 114

[63] Heo J, Rodriges M, Saggese S J and Sigel G H 1991 *Applied Optics* **30** (27) p 3944 - 3951

[64] Clausen S 1996 *Measurement Science and Technology* **7** p 888 - 896

[65] Shelly John M, Radhakrishnan P, Nampoori V P N and Vallabhan C P G 1999 *Measurement Science and Technology* **10** p N17 - N20

[66] Harrington J A 2000 *Fiber and Integrated Optics* **19** p 211 - 228

[67] Katsuyama T and Matsumura H 1989 *Infrared Optical Fibers* (Bristol: Adam Hilger)

[68] Klocek P 1991 *Handbook of infrared optical materials* (New York: Marcel Dekker)

[69] Sanghera J S and Aggarwal I D 1998 *Infrared Fiber Optics* (Boca Raton: CRC Press)

[70] Nishii J and Yamashita T 1998 *Chalcogenide Glass-Based Fibers* in *Infrared Fiber Optics* in *Infrared Fiber Optics* ed Sanghera J S and Aggarwal I D (Boca Raton: CRC Press) p 143 - 184

[71] Shibata S, Terunuma Y nad Manabe T 1981 *Material Research Bulleten* **16** p 703 - 714

[72] Dianov E M 1982 *Advances in IR Fibers* II Techn Dig SPIE (Los Angeles CA) p 320 - 324

[73] Kanamori T, Terunuma Y, Takahashi S and Miyashita T 1984 *Journal of Lightwave Technology* **LT-2** N5 p 607 - 613

[74] Hartouni E, Hulderman F and Guiton T 1984 *SPIE Proceedings* **505** p 131

[75] Nishii J, Yamashita T and Yamagishi T 1989 *Journal of Material Science* **24** p 4293 - 4297

[76] Kanamori T, Terunuma Y, Takahashi S and Miyashita T 1985 *Journal of Non-Crystalline Solids* **69** p 231 - 242

[77] Moynihan C T, Macedo P B, Maklad M S, Mohr R K and Howard R E 1976 *Journal of Non-Crystalline Solids* **17** p 369 - 385

[78] *Technical Data Sheet* Amorphous Materials Co.
    http://www.amorphousmaterials.com/IR-fibers.htm

[79] Gabriel O 2001 *Diplomarbeit* (University of Greifswald, Germany)

[80] Bornstein A, Katz M, Baram A and Wolfman D 1991 *Infrared Fiber Optics* III SPIE Proc **1591** p 256 - 262

[81] Burns W K, Abede M and Villarruel C A 1985 *Applied Optics* **24** (17) p 2753 - 2755

[82] Gupta B D and Singh C D 1994 *Fiber and Integrated Optics* **13** p 433 - 443

[83] Gupta B D and Singh C D 1994 *Applied optics* **33** (13) p 2737 - 2742

[84] Denaro A R, Owens P A and Crawshaw A 1968 *European Journal of Polymer* **4** p 93 - 106

[85] Thompson L F and Mayhan K G 1972 *Journal of Applied Polymer Science* **16**
p 2317 - 2341

[86] Lam D K, Baddour R F and Stancell A F 1976 in *Plasma Chemistry of Polymers*
ed Shen M (New York: Marcel Dekker) p 53

[87] Prohaska G W, Johnson E D and Evans J F 1984 *Journal of Polymer Science
Polymer Chemistry* **22** p 2953 - 2972

[88] Mackie N M, Castner D G and Fisher E R 1998 *Langmuir* **14** p 1227 - 1235

[89] Oehr Ch, Müller M , Elkin B, Hegemann D and Vohrer U 1999 *Surface and Coating
Technology* **25** p 116 -119

[90] Friedrich J, Retzko I, Kühn G, Unger W and Lippitz A 2001 *Metal doped Plasma Polymer
Films* in *Metallized Plastics* **VII** : *Fundamental and Applied Aspects* ed Mittal K L
(Utrecht: Kluwer Academic Publishers) p 117 - 142

[91] Chen M , Yang T-C and Zhou X 1996 *Journal of Polymer Science* **B 34** p 113 - 120

[92] Chen M and Yang T-C 1999 *Journal of Polymer Science Polymer Chemistry* **37** p 325 - 330

[93] Özden B, Hacaloglu J and Akovali G 1991 *European Polymer Journal* **27** (12) p 1405 - 1410

[94] Kobayashi H, Bell A T and Shen M, in *Plasma Chemistry of Polymers*, ed Shen M
(New York: Marcel Dekker) 1976

[95] Kobayashi H, Shen M and Bell A T 1974 Macromolecules **7** p 277

[96] Kobayashi H, Shen M and Bell A T 1974 Journal of Macromolecules Science Chemistry
A8 p 373

[97] Socrates G 1994 *Infrared Characteristic Group Frequencies* (Chichester: John Wiley)

[98] Lin-Vien D, Colthup N B, Fateley W G and Grasselli J G 1991 *Handbook of IR and
Raman Characteristic Frequencies of Organic Molecules* (London: Academic Press)

[99] *Galactic IR spectra* on-line Database http://spectra.galactic.com/spconline/
Compound: POLYSTYRENE CAS# 9003-53-6 Source: David Sullivan FT-IR Library

[100] Siesler H W and Holland-Moritz K 1980 *Infrared and Raman spectroscopy of Polymers*
(New York: Marcel Dekker) p 62

[101] Smith B 1999 *Infrared Spectral Interpretation. A systematic Approach*
(New York: CRC Press) p 5 - 6

[102] Cranfill B 1978 *Review of Scientific Instruments* **49** (2) p 264 - 265

[103] van Krevelen D W 1990 *Properties of Polymers* (Amsterdam: Elsevier Science)

[104] Bicerano J 1996 *Prediction of Polymer Properties* (New York: Marcel Dekker) p 68 - 69

[105] Wrobel A M, Wertheimer M R, Dib J and Schreiber H P 1980 *Journal of Macromolecular
Science Chemistry* A **14** p 321

[106] Wrobel A M, Kryszewski M and Gazicki M 1983 *Journal of Macromolecular
Science Chemistry* A **20** p 583 - 618

[107] Jasse B and Koenig J L 1981 *Polymer* **22** p 1040 - 1044

[108] Bredas J L and Street G B 1985 *Journal of Physics C Solid State Physics* **18** p L651 - L655

[109] Robertson J and O'Reilly E P 1987 *Physical Review B* **35** N6 p 2946 - 2957

[110] Yi J W, Lee Y H and Farouk B 1998 *Thin Solid Films* **326** p 154 - 159

[111] Coudere P and Catherine Y 1987 *Thin Solid Films* **146** p 93

[112] Stenzel O and Petrich R 1993 *Optical Engineering* **32** p 2951

[113] Hallil A and Despax B 2000 *Thin Solid Films* **358** p 30 - 39

[114] Ivanov Yu A 1981 *Methods of contact diagnostics in non-equilibrium plasma chemistry*
(Moscow: Nauka)

[115] Ovsyannikov A A and Zhukov M F 2000 *Plasma diagnostics* (Cambridge:
Cambridge International Science Publ.) p 338 - 355

[116] Schwabedissen A, Soll Ch, Brockhaus A and Engemann J 1999 *Plasma Sources Science
and Technology* **8** N3 p 440 - 447

[117] Smolinsky G and Vasile M J 1973 *International Journal of Mass Spectrometry
Ion Physics* **12** p 147 - 158

[118] Vasile M J and Smolinsky 1974 *International Journal of Mass Spectrometry
Ion Physics* **13** p 381 - 393

[119] Aumaille K, Vallee C, Granier A, Goullet A, Gaboriau F and Turban G 2000
Thin Solid Films **359** p 188 - 196

[120] Seefeldt R, Möller W and Schmidt M 1985 *Zeitschrift Phys Chemie* **266** p 797 - 807

[121] Alexander M R, Jones F R and Short R D 1997 *Journal of Physical Chemistry* B **101** N18 p 3614 - 3619

[122] Alexander M R, Jones F R and Short R D 1997 *Plasmas and Polymers* **2** N4 p 277 - 300

[123] Basner R, Foest R, Schmidt M, Becker K and Deutsch H 1998 *International Journal of Mass Spectrometry* **176** p 245 - 252

[124] Schmidt M, Foest R, Basner R and Hannemann M 1994 *Acta Physica Universitatis Comenianae* **XXXV** 2 p 217 - 227

[125] Foest R 1998 *Ph.D. Thesis* (University of Greifswald, Germany)

[126] Raynaud P, Segui Y, Balmer G, Boulanger A and Burke R R 1997 *Journal of Physics D: Applied Physics* **30** p L23 - L27

[127] Segui Y and Raynaud P 1997 *Plasma Diagnostic by Infrared Absorption Spectroscopy* in Plasma Processing of Polymers NATO ASI Series, Series E: Applied Sciences **346** ed d'Agostino R, Favia P and Fracassi F (Dordrecht: Kluwer Academic Publishers) p 81 - 100

[128] Lamendola R, dAgostino R and Fracassi F 1997 *Plasma and Polymers* **2** N3 p147 - 164

[129] Inoue Y and Takai O 1996 *Plasma Sources Science and Technology* **5** p 339 - 343

[130] Granier A, Nicolazo F, Vallee C, Goullet A, Turban G and Grolleau B 1997 *Plasma Sources Science and Technology* **6** p 147 - 156

[131] Granier A, Vallee C, Goullet A, Aumaille K and Turban G 1999 *Journal of Vacuum Science and Technology* A **17** (5) p 2470 - 2474

[132] Hays A K 1982 *Proceedings of Electrochemical Society* **82 - 86** (Princeton NY USA) p 75 - 87

[133] Seefeldt R and Schmidt M 1989 *Zeitschrift Phys Chemie* **270** p 427 - 441

[134] Sonnenfeld A, *private communications*

[135] Courteille C, Magni D, Deschenaux Ch, Howling A A and Hollenstein Ch 1998 *Gas Phase and Particle Diagnostic of HMDSO Plasmas by Infrared Absorption Spectroscopy* in Proceedings of 41st Annual Technical Conference Society of Vacuum Coaters 505/856-7188 (Boston, USA) p 327 - 332

[136] Röpcke J, Rivalde G, Osiac M, Li K and Meichsner J 2002 *Plasma Chemistry and Plasma Processing* **22** N1 p 139 - 159

[137] Sawada Y, Ogawa S and Kogoma M 1995 *Journal of Physics D : Applied Physics* **28** p 1661 - 1669

[138] Li K and Meichsner J 1999 *Surface and Coatings Technology* **116 - 119** p 841 - 847

[139] Gazicki M, Wrobel A M and Kryszewski M 1984 *Journal of Applied Polymer Science Symposium* **38** p 1 - 19

[140] Sahli S, Segui Y, Hadj Moussa S and Djouadi A 1992 *Thin Solid Films* **217** p 17 - 25

[141] Kim M T 1997 *Thin Solid Films* **311** p 157 - 163

[142] Wrobel A M, Kowalski J, Grebowicz J and Kryszewski M 1982 *Journal of Macromolecular Science Chemistry* **A 17** p 433 - 452

[143] Wrobel A M 1987 *Plasma Chemistry Plasma Processing* **7** p 429 - 450

[144] Poll H P, Arzt M, Wickleder K H 1976 *European Polymer Journal* **12** N7 505 - 512

[145] Yasuda H 1981 *Journal of Polymer Science Macromolecule Review* **16** p 199

[146] EPA MS number 61595 2001 *NIST Chemistry WebBook NIST Mass Spectrometry Data* Center

[147] Chatham H, Hils D, Robertson R and Gallagher A 1984 *Journal of Chemical Physics* **81** N4 p 1770 - 1777

[148] Sugai H and Toyoda H 1992 *Journal of Vacuum Science and Technology* **A10** N4 p 1193 - 1200

[149] Fan W Y, Knewstubb P F, Käning M, Mechold L, Röpcke J and Davies P B 1999 *Journal of Physical Chemistry* **A 103** p 4118 - 4128

[150] Scott K 1998 *Handbook of industrial membranes* (Kidlington: Elsevier) p 29

[151] *Eight Peak Index of Mass Spectra* 1974 Mass Spectrometric Data Centre (London: Elsevier) **I** p 1 - 2

[152] Poll H-U, Meichsner J, Arzt M, Friedrich M, Rochotzki R and Kreyßig E 1993 *Surface and Coating Technology* **59** p 365 - 370

[153] Morosoff N 1990 *An Introduction to Plasma Polymerization* in *Plasma Deposition, Treatment and Etching of Polymers* ed by d'Agostino R (London: Academic Press) p 17 - 27

[154] Rochotzki R 1996 *PhD thesis* (Chemnitz, Germany: Technical University of Chemnitz)

[155] Kay E, Coburn J and Dilks A 1980 *Topics Current Chemistry* **94** p 1

[156] Bieg K W 1981 *Thin Solid Films* **84** p 411

[157] Schwarz J, Schmidt M and Ohl A 1998 *Surface Coating Technology* **98** p 859 - 864

[158] Wright N and Hunter M J 1947 *Journal of American Chemical Society* **69** p 803

[159] Kilpatrick J E and Pitzer K S 1949 *Journal of Chemical Physics* **17** p 1064

[160] Scott D W, Messerly J F, Todd S S, Guthrie G B, Hossenlopp I A, Moore R T, Osborn Ann, Berg W T and McCullough J P 1961 *Journal of Physical Chemistry* **65** p 1320 - 1326

[161] Rau Ch and Kulisch W 1994 *Thin Solid Films* **249** p 28 - 37

[162] Haraguchi T and Ide S 1988 *Journal of Applied Polymer Science, Applied Polymer Symposium* **42** p 357

[163] Huber F, Springer J and Muhler M 1997 *Journal of Applied Polymer Science* **63** p 1517 - 1526

[164] Sakata J, Yamamoto M and Hirai M 1986 *Journal of Applied Polymer Science* **31** p 1999 - 2006

[165] Weichart J and Müller J 1993 *Surface and Coating Technology* **59** p 342 - 344

[166] Radeva E, Tsakov D, Bobev K and Spassov L 1993 *Journal of Applied Polymer Science* **50** p 165

[167] Morra M, Occhiello E and Garbassi F 1993 *Journal of Applied Polymer Science* **48** p 1331

[168] Nehlsen S, Hunte T and Müller J 1995 *Journal of Membrane Science* **106** p 1- 7

[169] Zuri L, Silverstein M S and Narkis M 1996 *Journal of Applied Polymer Science* **62** p 2147 - 2154

[170] NIST Chemistry Webbook Database 2001 http://webbook.nist.gov/ (Compound: Hexamethyldisiloxane, CAS Number: 107-46-0)

Appendix "A"

The hexamethyldisiloxane (HMDSO) is the simplest siloxane compound which is characterized by a siloxane group, Si-O-Si, in the molecular structure. In comparison with other monomers HMDSO is not toxic or explosive and has a high vapour pressure at the room temperature. Some physical and chemical properties of hexamethyldisiloxane monomer are summarized in Table 1.

Name	Hexamethyldisiloxane, HMDSO
CAS-number	107-46-0
Structure	$(CH_3)_3SiOSi(CH_3)_3$
Vapour pressure at 25°C, [kPa]	3.7
Molecular weight, [g/mol]	162.38
Density at 25°C, [g/cm^{-3}]	0.76
Index of refraction at 20°C, 589 nm	1.377

Table 1. Physical and chemical properties of hexamethyldisiloxane (the further data on the substance can be found in the NIST Web Database [170]).

Structure of hexamethyldisiloxane molecule:
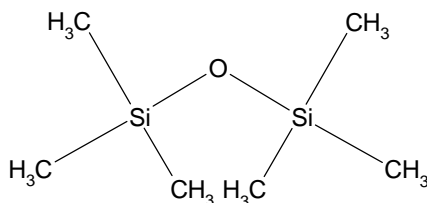
Data on bond distances and angles:

Si-O	1.63 Å
Si-C	1.88 Å
C-H	1.09 Å
Si-O-Si	135°

Calculated values of the force constants, according [169]:

the bond stretching force constants:	Si-C stretching	2.723×10^5	dynes cm^{-1}
	Si-O stretching	4.288×10^5	dynes cm^{-1}
the angle bending force constants:	Si-C-H bending	0.442×10^{-11}	ergs radian^{-2}
	C-Si-C bending	0.625×10^{-11}	ergs radian^{-2}
	C-Si-O bending	0.625×10^{-11}	ergs radian^{-2}
	Si-O-Si bending	0.500×10^{-11}	ergs radian^{-2}

The barrier heights for:

methyl rotations	1600 $cal\ mole^{-1}$
siloxane rotations	from 0 up to a few hundred $cal\ mole^{-1}$
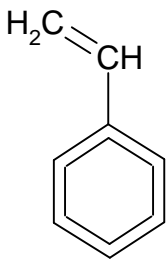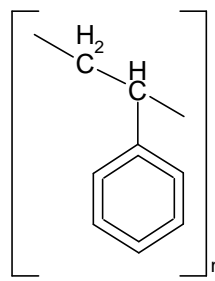
Vibrational spectrum of hexamethyldisiloxane:

Wavenumber, cm^{-1}	Assignment
331	skeletal C-Si-C bending
524	symmetrical Si-O stretching
619	Si-C stretching
687	Si-C stretching
756	Si-C stretching
832	CH_3 rocking
850	CH_3 rocking
1060	asymmetric Si-O stretching
1256	symmetrical CH_3 bending
1410	unsymmetrical CH_3 bending
1438	unsymmetrical CH_3 bending
2900	C-H stretching
2960	asymmetric C-H stretching

Appendix "B"

Physical and chemical properties of styrene and chemically prepared polystyrene

| Name	Styrene	Polystyrene
CAS-number	100-42-5	
Structure	C_8H_8	$-(C_8H_8)_n-$
Vapour pressure at 20°C, [hPa]	6	-
Molecular weight, [g/mol]	104.15	$(1-4) \times 10^5$
Density at 20°C, [g/cm^{-3}]	0.906	1.05
Index of refraction at 20°C, 589 nm	1.546	1.58 -1.60

Appendix "C"

Accumulated IR absorption spectra of plasma polymer films growing on the fibre in HMDSO-containing plasmas of rf discharge ignited for various plasma pulse durations.

HMDSO plasma (15 Pa, 130 W, 5 $sccm$)
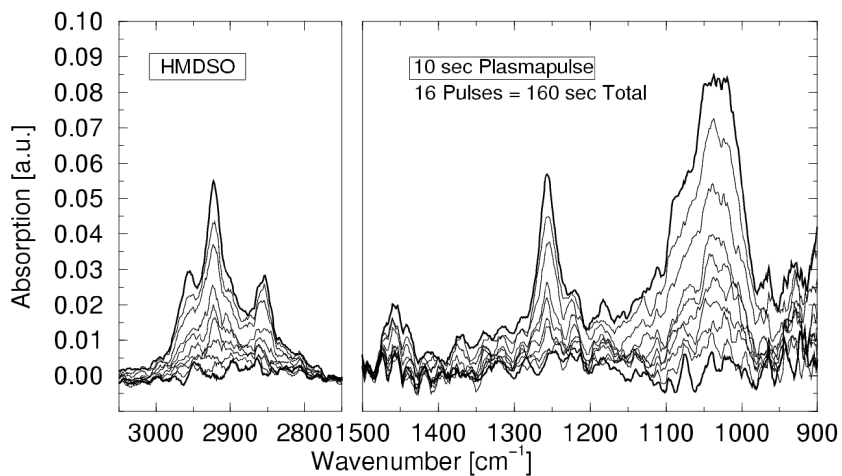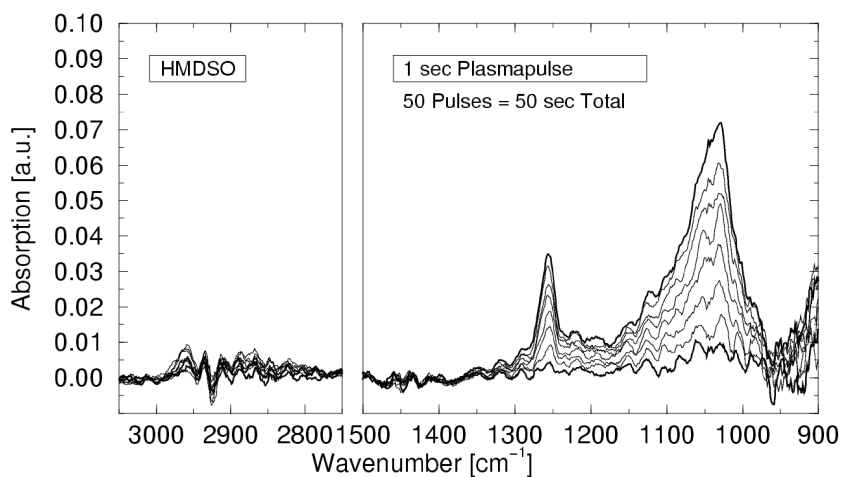
HMDSO/O$_2$ plasma (15 Pa, 130 W, 3 $sccm$ HMDSO, 17 $sccm$ O$_2$)
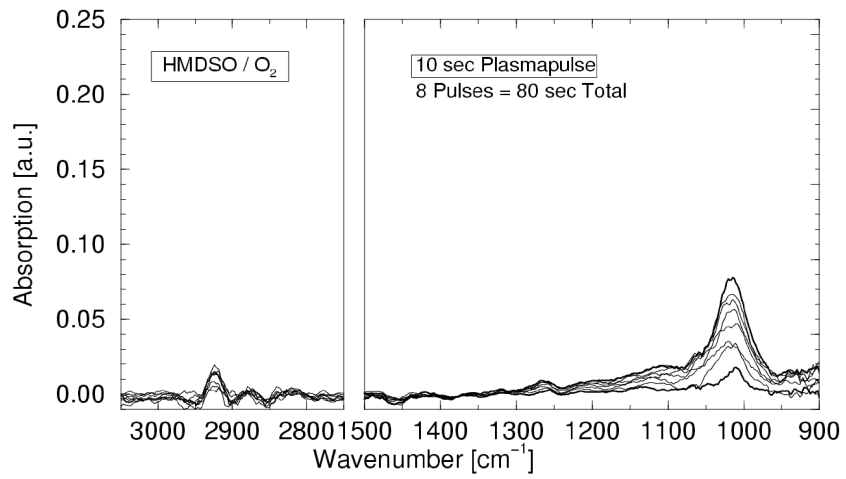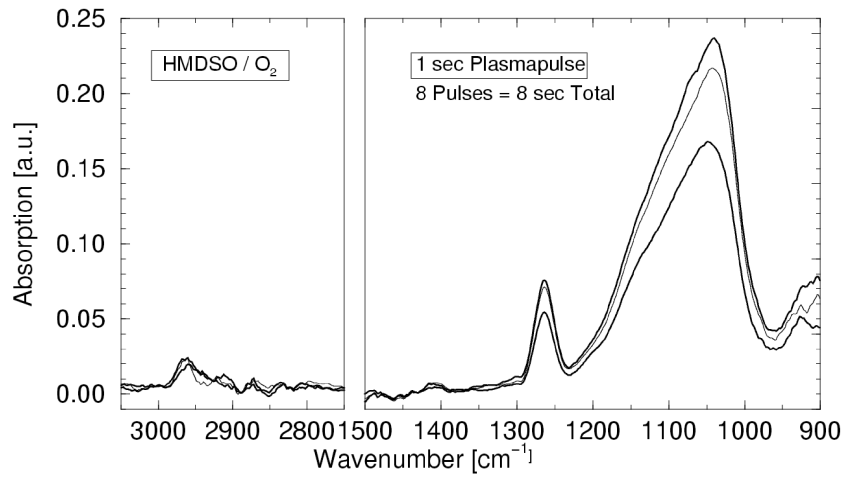
Appendix "D"

The line positions of chosen absorption bands.

<u>Deposition on the IR fibre at the floating potential.</u>

HMDSO plasma, 15 Pa, 130 W, 5 $sccm$ HMDSO

Wavenumber, cm^{-1}	Vibration
2958 2922 2895 2857	C-H stretching, in CH_3
1256	Si-C deformation, in $Si(CH_3)_3$
1070 1037	Si-O stretching, in Si-O-Si

HMDSO/O_2 plasma: 15 Pa, 130 W, 3 $sccm$ HMDSO, 17 $sccm$ O_2

Wavenumber, cm^{-1}	Vibration
1264	CH_3 deformation, in $Si(CH_3)_3$
1102 1035	Si-O stretching, in Si-O-Si

<u>Deposition on the rf electrode.</u>

HMDSO plasma, 15 Pa, 130 W, 5 $sccm$ HMDSO

Pulse duration, s	Wavenumber, cm^{-1}	Intensity, [a.u.]	Vibration
1	2961	0.015	
5	2961	0.015	
10	2961	0.012	C-H stretching
30	2960	0.004	
60	2959	0.003	
240	2959	0.001	
1	1259	0.059	
5	1259	0.062	
10	1259	0.051	Si-C deformation
30	1259	0.021	
60	1258	0.012	
240	1275	0.003	
1	1072	0.094	
5	1070	0.106	
10	1072	0.093	Si-O stretching
30	1070	0.070	
60	1057	0.044	
240	1043	0.033	
1	847	0.043	
5	847	0.046	
10	847	0.036	CH_3 rocking
30	845	0.014	
60	845	0.007	
240	840	0.004	
1	804	0.030	
5	804	0.032	
10	806	0.025	CH_3 rocking
30	806	0.015	
60	809	0.006	
240	801	0.005	

HMDSO/O$_2$ plasma: 15 Pa, 130 W, 3 $sccm$ HMDSO, 17 $sccm$ O$_2$

Pulse duration, s	Wavenumber, cm^{-1}	Intensity, [a.u.]	Vibration
1	2966	0.007	
5	2966	0.003	C-H stretching
10	2966	0.002	
240	-	-	
1	1274	0.034	
5	1274	0.019	Si-C deformation
10	1275	0.010	
240	1275	0.003	
1	1149	0.066	
5	1156	0.055	Si-O stretching
10	1163	0.045	
240	1187	0.044	
1	1096	0.086	
5	1102	0.075	Si-O stretching
10	1106	0.057	
240	1128	0.051	
1	850	0.021	
5	848	0.007	CH$_3$ rocking
10	853	0.004	
240	-	-	
1	809	0.025	
5	809	0.015	CH$_3$ rocking
10	812	0.010	
240	-	-	

Appendix "E"

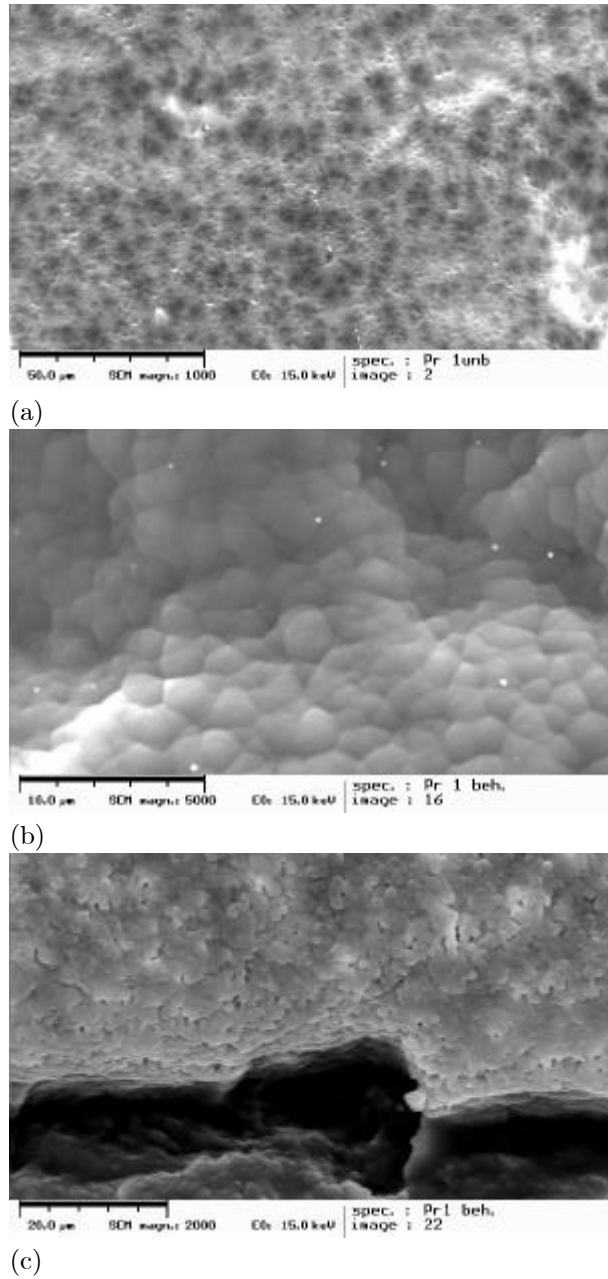SEM micrographs of plasma polymer films deposited on various substrates.
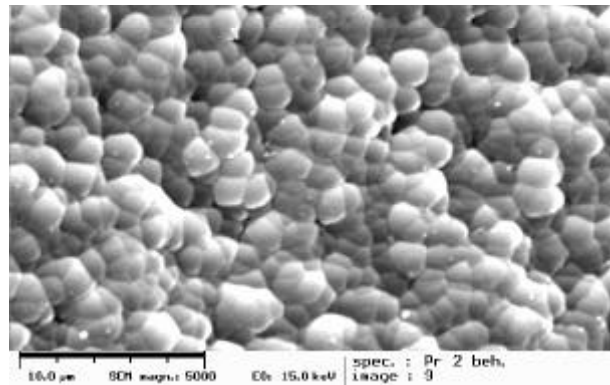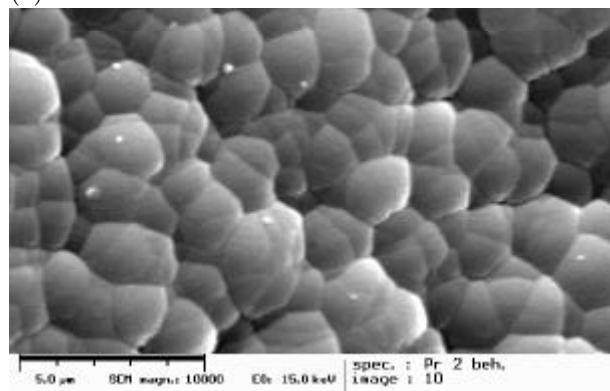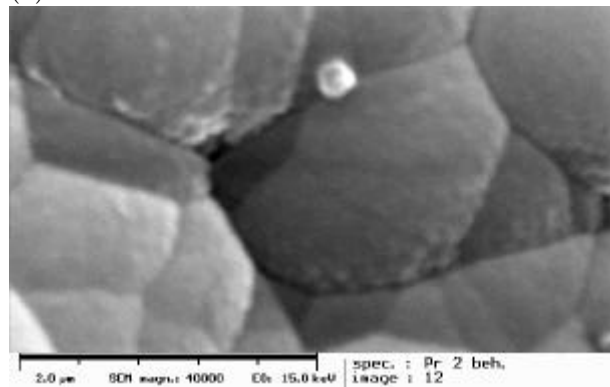

(a)

(b)

(c)

Figure 27. (a) Cellulose acetate membrane without plasma polymer,
(b) Cellulose acetate membrane with the HMDSO plasma polymer
deposited at the process conditions: 10 Pa, 60 W, 2 $sccm$ HMDSO,
(c) cross-section of the composite membrane with plasma polymer.

(a)

(b)

(c)

Figure 24. SEM micrographs of PA 6,6 film with the HMDSO plasma polymer
deposited at the process conditions: 10 Pa, 60 W, 2 $sccm$ HMDSO.
Magnification: (a) 5×10^3, (b) 10^4, (c) 4×10^4.

Erklärung

Hiermit erkläre ich, daß diese Arbeit bisher von mir weder an der Mathematisch-Naturwissenschaftlichen Fakultät der Ernst-Moritz-Arndt-Universität Greifswald noch einer anderen wissenschaftlichen Einrichtung zum Zwecke der Promotion eingereicht wurde.

Ferner erkläre ich, daß ich diese Arbeit selbständig verfaßt und keine anderen als die darin angegebenen Hilfsmittel benutzt habe.

Lebenslauf

Persönliche Daten

Name	Konstantin Li
Geburtsdatum	10 Juni 1972
Geburtsort	Magnitogorsk, Russische Föderation
Familienstand	verheiratet, ein Kind

Studium

Sep 1979 - Juli 1989	Mittelschule 28, Magnitogorsk, Russische Föderation
Sep 1989 - Juni 1995	Moskauer Institut für Physik und Technologie, MIPT, Fakultät für molekulare und chemische Physik
Sep 1993 - Juni 1995	Russische Forschungszentrum "Kurchatov Institut" Diplomarbeit: '*Plasmamodifizierung gastrennenden Polymermembranen in einer HF-Entladung.*'
Juni 1995	Staatliche Diplom, /Qualifikation: Ingenieur-Physiker, Fachgebiet: Angewandte Physik und Mathematik/

Promotionsstudium

Sep 1995 - Feb 1997	Aspirant am MIPT
März 1997 - Apr 1999	Stipendiat des Graduiertenkollegs "Dünne Schichten und nichtkristalline Materialien" der Technischen Universität Chemnitz
seit Apr 1999	Doktorand am Institut für Physik, Ernst-Moritz-Arndt-Universität Greifswald

Wissenschaftlicher Werdegang

seit Apr 1999	wissenschaftlicher Mitarbeiter am Institut für Physik, Ernst-Moritz-Arndt-Universität Greifswald

Greifswald, Februar 2002

Acknowledgements

Here, with great joy I count my Acknowledgements to the contributors who have, in practice as well as in spirit, made the completion of this thesis possible.

Sincere thanks to Prof. Dr. Jürgen Meichsner, who is most responsible for my success as a graduate student, for invaluable guidance and dedication, for giving me freedom and skill to explore.

Deepest thanks go to all members of the group "Niedertemperaturplasmaphysik" (Institute of Physics, University of Greifswald) for your immense help, patience, and kindness. My time at the Institute has been greatly enhanced by them who have helped me within and outside of the Lab with issues, scientific or otherwise. I would like to thank Martin Geigl for his wise council, he made my life in Germany enjoyable providing more than just moral support.

Thanks to Silke Peters and Bert Krames for interesting discussions and for being so welcoming. Thanks to Onno Gabriel for the fruitfull collaboration. Great thanks to Peter Druckrey and Mathias Wilsnack.

Thanks to Dr. Jürgen Röpcke (INP, Greifswald) and his team for introducing me into the "new" world of IR Tuneable Diode Laser Absorption Spectroscopy and successful cooperation which, I hope, will continue. Thanks to Vasile Vartolomei for XPS analysis of numerous samples.

I would like to express my gratitude to Prof. Dr. Frank Richter and Prof. Dr. Dieter Gerlich for offering the opportunity to study at the Graduiertenkolleg "Dünne Schichten und nichtkristalline Materialien" (Institute of Physics, Technical University of Chemnitz) where I began to work on this thesis. I would like to thank my friends and collegues from TU Chemnitz. The efforts made by Adelheid Steinrücken in taking the SEM micrographs are greatly appreciated. Her assistance in technical issues was very valuable.

This work was primarily supported by Deutsche Forschungsgemeinschaft through a fellowship of Graduiertenkolleg "Dünne Schichten und nichtkristalline Materialien". DFG provided further funding for this project under the contract ME 1506-1/2.

Finally, I would like to thank my family for love, encouragement and understanding. I could never have made it to the end without them behind me.